

**TRACE ELEMENTS AND COLOR-CAUSING ROLE IN
SPINEL AND TANZANITE**



Mr. Teerarat Pluthametwisute

จุฬาลงกรณ์มหาวิทยาลัย
CHULALONGKORN UNIVERSITY

**A Dissertation Submitted in Partial Fulfillment of the Requirements
for the Degree of Doctor of Philosophy in Geology**

**Department of Geology
FACULTY OF SCIENCE
Chulalongkorn University
Academic Year 2021**

Copyright of Chulalongkorn University

ธาตุร่องรอยกับบทบาทการให้สีในสปีเนลและแทนซาไนต์



วิทยานิพนธ์นี้เป็นส่วนหนึ่งของการศึกษาตามหลักสูตรปริญญาวิทยาศาสตรดุษฎีบัณฑิต

สาขาวิชาธรณีวิทยา ภาควิชาธรณีวิทยา

คณะวิทยาศาสตร์ จุฬาลงกรณ์มหาวิทยาลัย

ปีการศึกษา 2564

ลิขสิทธิ์ของจุฬาลงกรณ์มหาวิทยาลัย

ธีรรัฐ พุทธรเมธวิสุทธิ์ : ชาติรุ่งอรอยกับบทบาทการให้สีในสปิเนลและแทนซาไนต์. (TRACE ELEMENTS AND COLOR-CAUSING ROLE IN SPINEL AND TANZANITE) อ.ที่ปรึกษาหลัก : ศ. ดร.จักรพันธ์ สุทธิรัตน์, อ.ที่ปรึกษาร่วม : ดร.ภูวคล วรธนะชัยแสง

งานวิจัยนี้ได้ทำการศึกษาชาติรุ่งอรอยและบทบาทการเกิดสีในแทนซาไนต์ และสปิเนล (7 กลุ่มสี) โดยเฉพาะปริมาณของธาตุ สถานะออกซิเดชัน และตำแหน่งที่อยู่ในโครงสร้างที่เป็นสาเหตุการเกิดสีในอัญมณีทั้งสองชนิด ซึ่งยังไม่เคยมีงานวิจัยที่แสดงผลลัพธ์ชัดเจนทั้งก่อนและหลังเผาอัญมณีทั้งสองชนิด จากการศึกษาครั้งนี้พบว่าแทนซาไนต์ตามธรรมชาติจะแสดงสีไครโคริกอย่างชัดเจน ประกอบด้วยสีม่วง สีน้ำเงินและสีน้ำตาลในทิศทางที่ต่างกัน โดยสมบัตินี้จะเปลี่ยนเป็นไครโคริกสีน้ำเงิน-ม่วงหลังการปรับปรุงคุณภาพสีด้วยการเผา โดยปริมาณของธาตุวานาเดียมที่แทนที่ในตำแหน่งออกตะอิตรัลภายในโครงสร้างจะเป็นสาเหตุของสีหลัก หลังการเผาพบว่าแถบการดูดกลืนแสงในช่วงน้ำเงิน-ม่วงที่จุดศูนย์กลางประมาณ 450-460 นาโนเมตร ลดลงอย่างเห็นได้ชัด ซึ่งส่งผลให้เกิดสีม่วงที่ชัดเจนยิ่งขึ้น โดยผลที่ได้จากเทคนิคการดูดกลืนรังสีเอ็กซ์ยังชี้ให้เห็นถึงการเพิ่มขึ้นของสถานะออกซิเดชันของธาตุวานาเดียม ดังนั้นวานาเดียมจึงเป็นธาตุให้สีที่สำคัญอย่างยิ่งในแทนซาไนต์สอดคล้องกับปริมาณที่เด่นกว่าชาติรุ่งอรอยอื่น

จากการศึกษาสปิเนลในครั้งนี้พบว่า องค์ประกอบของชาติรุ่งอรอย อาทิ โครเมียม โคบอลต์ เหล็ก และ วานาเดียม เป็นสาเหตุของความหลากหลายสีในสปิเนล โดยอัตราส่วนของธาตุให้สีเหล่านี้ส่งผลโดยตรงต่อองค์ประกอบสี โดยสีแดงในสปิเนลเป็นผลมาจากสัดส่วนธาตุโครเมียมและวานาเดียมประกอบกันอย่างมีนัยสำคัญ ส่วนสีชมพู สีม่วง สีน้ำเงิน และสีเขียวในสปิเนลนั้นได้รับอิทธิพลมาจากปริมาณของธาตุเหล็ก ในขณะที่สีส้มในสปิเนลเป็นผลมาจากธาตุวานาเดียมอย่างเห็นได้ชัด หลังการทดลองเผาพบว่า การวิเคราะห์ด้วยเทคนิคการดูดกลืนรังสีเอ็กซ์แสดงการเพิ่มสูงขึ้นของสถานะออกซิเดชันและการเปลี่ยนแปลงตำแหน่งที่อยู่ของธาตุให้สีเหล่านี้ในโครงสร้าง ยกเว้นธาตุโครเมียมที่ไม่พบการเปลี่ยนแปลงสถานะออกซิเดชัน นอกจากนี้การขยายกว้างขึ้นของพีคที่ตำแหน่งราว 406.2 ซม.⁻¹ และพีคเล็ก ๆ ที่เกิดขึ้นประมาณ 715.2-719.8 ซม.⁻¹ ในสเปกตรัมรามาน ร่วมกับการขยายกว้างขึ้นของพีคสำคัญที่ 685 นาโนเมตร และการลดลงของความชัดเจนของพีคอื่น ๆ ในสเปกตรัมโฟโตลูมิเนสเซนซ์ เป็นตัวบ่งชี้สำคัญแสดงถึงสปิเนลที่ผ่านการเผาที่เป็นประโยชน์ต่อการตรวจสอบการปรับปรุงคุณภาพสปิเนลเป็นอย่างมาก

สาขาวิชา ธรณีวิทยา

ลายมือชื่อนิสิต

ปีการศึกษา 2564

ลายมือชื่อ อ.ที่ปรึกษาหลัก

ลายมือชื่อ อ.ที่ปรึกษาร่วม

6072064723 : MAJOR GEOLOGY

KEYWORD tanzanite, spinel, heat treatment, color, XAS

D:

Teerarat Pluthametwisute : TRACE ELEMENTS AND COLOR-CAUSING ROLE IN SPINEL AND TANZANITE. Advisor: Prof. CHAKKAPHAN SUTTHIRAT, Ph.D. Co-advisor: Bhuwadol Wanthanachaisaeng, Ph.D.

This research is aimed to investigate the significant trace elements and their color-causing roles in tanzanite and spinels (7 color varieties) by focusing on their concentrations, valencies, and site occupancy since no palpable research has been reported previously either before or after heating of both gems. According to this finding, natural tanzanites usually show strongly trichroic colors of violet, blue, and brown in different directions. However, this characteristic is easily changed to violet-blue dichroism after heat treatment. As the result, the violet-blue absorption band (centered around 450–460 nm) is obviously decreased after heating, and XAS analysis indicates the higher valency state of vanadium. Consequently, vanadium is strongly suggested as the significant coloring agent in tanzanite which is also supported by its dominant concentration.

Based on this finding, natural spinels contain trace elements which may cause various hues. Red color is attributed by the combination of significant Cr and V ratios. Magenta and purple to blue and green colors are affected by significant Fe content, whereas orange color shows contribution to significant V content. After heating, XAS indicates a greater oxidation state as well as disordering of iron and vanadium, while Cr stays consistent. Broadening of the dominant peak at around 406.2 cm^{-1} and the occurrence of additional small peak at around $715.2\text{--}719.8\text{ cm}^{-1}$ in Raman spectra as well as broadening of the 685 nm and poorly defined structure of additional peaks in photoluminescence spectra are significant indicators of inverse spinels (heated spinel) which strongly benefits gem-testing laboratory to recognize the heat-treated spinel.

Field of Study:	Geology	Student's Signature
Academic Year:	2021
		Advisor's Signature
	
		Co-advisor's Signature
	

ACKNOWLEDGEMENTS

This research is supported by the 90th Anniversary of Chulalongkorn University Fund (Ratchadaphiseksomphot Endowment Fund) and the 100th Anniversary Chulalongkorn University for Doctoral Scholarship. The author wishes to express his gratitude to both supervisors, Professor Dr. Chakkaphan Sutthirat and Dr. Bhuwadol Wanthanachaisaeng for their counsel and support; without their supervision, this study would have been far more difficult and unattainable to accomplish. The author also acknowledges the Synchrotron Light Research Institute (Public Organization) or SLRI, particularly all staffs of the beamline 1.1W (MXT) for technical support. Special thank is sent to Mrs. Sopit Poompeang for assistance in EPMA analysis as well as Mr. Thanapong Lhuaamporn and Miss Waratchanok Suwanmanee for facilitation at The Gem and Jewelry Institute of Thailand (Public Organization), GIT.

Last but not least, the author wants to express his thankfulness to his parents (Mom and Dad) and younger brother (personal doctor) for their unwavering support throughout this challenging period. The author absolutely loves his family, Pluthametwisute and Jaijadee.

TABLE OF CONTENTS

	Page
.....	iii
ABSTRACT (THAI)	iii
.....	iv
ABSTRACT (ENGLISH).....	iv
ACKNOWLEDGEMENTS.....	v
TABLE OF CONTENTS.....	vi
LIST OF TABLES.....	ix
LIST OF FIGURES	x
CHAPTER 1	1
INTRODUCTION	1
1.1 General statement.....	1
1.2 Objective	2
1.3 Tanzanite.....	2
1.3.1 Occurrence.....	4
1.3.2 Heat treatment and coloration.....	6
1.4 Spinel.....	7
1.4.1 Occurrence.....	9
1.4.2 Heat treatment and coloration.....	12
CHAPTER 2	14
MATERIALS AND METHODOLOGY.....	14
2.1 Tanzanite samples	14
2.2 Spinel samples	17
CHAPTER 3	20

TANZANITE	20
3.1 Results	20
3.1.1 General gemological properties	20
3.1.2 Mineral chemistry	21
3.1.3 Heat treatment.....	25
3.1.4 UV-VIS-NIR spectroscopy.....	27
3.1.5 X-ray absorption spectroscopy.....	29
3.2 Discussion	31
3.2.1 Absorption spectra.....	31
3.2.2 X-ray absorption spectroscopy and chemistry	33
CHAPTER 4	35
SPINEL	35
4.1 Results.....	35
4.1.1 General gemological properties	35
4.1.2 Mineral chemistry	36
4.1.3 Heat treatment.....	42
4.1.4 UV-VIS-NIR spectroscopy.....	44
4.1.5 Raman spectroscopy	46
4.1.6 Photoluminescence spectroscopy	47
4.1.7 X-ray absorption spectroscopy.....	47
4.2 Discussion	52
4.2.1 Color-causing elements	52
4.2.2 Indication of heated spinel	57
CHAPTER 5	61

CONCLUSION AND RECOMMENDATION.....	61
5.1 Conclusion.....	61
5.2 Recommendation.....	62
REFERENCES	64
APPENDICES	73
APPENDIX A Tanzanite XAS Spectra.....	74
APPENDIX B Tanzanite UV-Visible Absorption Spectra	76
APPENDIX C Spinel UV-Visible Absorption Spectra.....	81
APPENDIX D Spinel Raman Spectra.....	92
APPENDIX E Spinel PL Spectra	103
APPENDIX F Spinel Fe K-edge XANES Spectra	114
APPENDIX G Spinel V K-edge XANES Spectra	120
APPENDIX H Fe-V-Cr pre-edge interpretation result diagrams	126
VITA.....	129

LIST OF TABLES

	Page
Table 1 Groups of spinels (Bosi et al., 2019).....	9
Table 2 XAS parameters for analyses of iron, chromium, and vanadium.....	18
Table 3 General properties of tanzanite samples.	20
Table 4 Electron probe microanalyzer (EPMA) analyses of major and trace compositions of tanzanite samples under this investigation.....	22
Table 5 Edge energy values of V and Ti obtained from K-edge X-ray absorption near edge structure (XANES) spectra of tanzanite samples before and after the heating experiment.	29
Table 6 Physical properties of spinel samples in this investigation.	35
Table 7 EPMA analyses of major and trace elements of spinel samples.....	38
Table 8 Summary of UV-visible absorption approximate in each colored spinel groups.	54

LIST OF FIGURES

	Page
Figure 1 Trichroism of a natural tanzanite rotated in three directions showing violet, blue, and green pleochroic colors	2
Figure 2 (a) Zoisite octahedral chain (M1, 2) combined with additional octahedra (M3) on only one side along b-direction, whereas (b) additional octahedra (M3) located on both sides of clinozoisite octahedral chain (M1) with (c) isolated octahedral chain (M2)	4
Figure 3 Beamline 1.1W: Multiple X-ray Technique station (Photo by C. Saiyasombat)	16
Figure 4 All tanzanite samples show natural trichroic colors including purple, green, and yellow dominating along the directions of a-, b-, and c-axes, respectively. All samples turned to dichroic coloration between violet color (along the a- and c-axes) and blue color (along the b-axis) after the heating experiment.	26
Figure 5 Representative absorption spectra of natural (blue spectrum) and heated (red spectrum) along the a-axis (a), b-axis (b), and c-axis (c) of a tanzanite sample (T04)	28
Figure 6 Plots of absorption edge energy (E ₀) of vanadium in natural tanzanite samples and after heating experiment with a calibration curve (dotted line) fitted by standard V ₂ O ₃ and V ₂ O ₄ ; oxidation states of vanadium in most samples appear to increase after heating.	30
Figure 7 Plots of absorption edge energy (E ₀) of titanium in natural tanzanite samples and after heating experiment with a calibration curve (dotted line) fitted by standard Ti ₂ O ₃ and TiO ₂ ; oxidation states of titanium tend to decrease after heating.	30
Figure 8 Representative spinel samples of each color group presenting appearances before and after heating as reported in the main text.	43

Figure 9 Representative of UV-visible absorption spectra of all spinel varieties and their pattern change after heating experiment under this study.	45
Figure 10 Representative Raman spectra of a) red spinel as a common pattern of most sample groups and b) green spinel presenting dissimilarly pattern to the other groups both before (blue lines, lower spectra) and after (red lines, upper spectra) heating experiment.	46
Figure 11 Representative PL spectra of a) orange spinel as a representative pattern of most samples, and b) green spinel with dissimilar pattern to the other spinels both before (blue lines, lower spectra) and after heating experiment (red lines, upper spectra).	47
Figure 12 Representative of Fe pre-edge XANES spectra composition.	51
Figure 13 Diagram represented integrated pre-edge intensity and pre-edge peak centroid ($E-E_0$) parameter of all spinel samples in various a) Fe- and b) V-oxidation state and their coordination, whereas c) represented normalized Cr pre-edge XANES spectra of natural (blue lines) and heated (red lines) spinels compared with Cr(III) and Cr(VI) standards. Number [4], [5], and [6] represent a 4-fold, 5-fold, and 6-fold coordinated atoms, respectively.	51
Figure 14 Ternary plots of Fe-Cr-V of spinel samples showing atomic ratios involving color.	53
Figure 15 Normalized V K-edge XANES spectra of all natural and heated Tanzanite samples compared with vanadium standards.	74
Figure 16 Normalized Ti K-edge XANES spectra of all natural and heated Tanzanite samples compared with titanium standards.	75
Figure 17 Visible absorption spectra of tanzanite sample T04 in three directions before (blue lines) and after (red lines) heating.	76
Figure 18 Visible absorption spectra of tanzanite sample T06 in three directions before (blue lines) and after (red lines) heating.	77

Figure 19 Visible absorption spectra of tanzanite sample T09 in three directions before (blue lines) and after (red lines) heating.	78
Figure 20 Visible absorption spectra of tanzanite sample T11 in three directions before (blue lines) and after (red lines) heating.	79
Figure 21 Visible absorption spectra of tanzanite sample T12 in three directions before (blue lines) and after (red lines) heating.	80
Figure 22 UV-visible absorption spectra of natural (blue line) and heated (red line) red spinel sample S1-01.	81
Figure 23 UV-visible absorption spectra of natural (blue line) and heated (red line) red spinel sample S1-03.	81
Figure 24 UV-visible absorption spectra of natural (blue line) and heated (red line) red spinel sample S1-07.	82
Figure 25 UV-visible absorption spectra of natural (blue line) and heated (red line) red spinel sample S1-10.	82
Figure 26 UV-visible absorption spectra of natural (blue line) and heated (red line) magenta spinel sample S2-20.	83
Figure 27 UV-visible absorption spectra of natural (blue line) and heated (red line) magenta spinel sample S2-22.	83
Figure 28 UV-visible absorption spectra of natural (blue line) and heated (red line) magenta spinel sample S2-25.	84
Figure 29 UV-visible absorption spectra of natural (blue line) and heated (red line) orange spinel sample S3-04.	84
Figure 30 UV-visible absorption spectra of natural (blue line) and heated (red line) orange spinel sample S3-11.	85
Figure 31 UV-visible absorption spectra of natural (blue line) and heated (red line) orange spinel sample S3-18.	85

Figure 32 UV-visible absorption spectra of natural (blue line) and heated (red line) orange spinel sample S3-23.	86
Figure 33 UV-visible absorption spectra of natural (blue line) and heated (red line) orange spinel sample S3-27.	86
Figure 34 UV-visible absorption spectra of natural (blue line) and heated (red line) red-purple spinel sample S4-02.	87
Figure 35 UV-visible absorption spectra of natural (blue line) and heated (red line) red-purple spinel sample S4-03.	87
Figure 36 UV-visible absorption spectra of natural (blue line) and heated (red line) red-purple spinel sample S4-06.	88
Figure 37 UV-visible absorption spectra of natural (blue line) and heated (red line) red-purple spinel sample S4-14.	88
Figure 38 UV-visible absorption spectra of natural (blue line) and heated (red line) purple spinel sample S5-04.	89
Figure 39 UV-visible absorption spectra of natural (blue line) and heated (red line) purple spinel sample S5-09.	89
Figure 40 UV-visible absorption spectra of natural (blue line) and heated (red line) purple spinel sample S5-13.	90
Figure 41 UV-visible absorption spectra of natural (blue line) and heated (red line) purple spinel sample S5-22.	90
Figure 42 UV-visible absorption spectra of natural (blue line) and heated (red line) blue spinel sample S6-04.	91
Figure 43 UV-visible absorption spectra of natural (blue line) and heated (red line) green spinel sample S7-08.	91
Figure 44 Raman spectra of natural (blue line) and heated (red line) spinel S1-01.	92
Figure 45 Raman spectra of natural (blue line) and heated (red line) spinel S1-03.	92

Figure 46 Raman spectra of natural (blue line) and heated (red line) spinel S1-07.93	
Figure 47 Raman spectra of natural (blue line) and heated (red line) spinel S1-10.93	
Figure 48 Raman spectra of natural (blue line) and heated (red line) spinel S2-20.	
.....	94
Figure 49 Raman spectra of natural (blue line) and heated (red line) spinel S2-22.	
.....	94
Figure 50 Raman spectra of natural (blue line) and heated (red line) spinel S2-25.	
.....	95
Figure 51 Raman spectra of natural (blue line) and heated (red line) spinel S3-04.	
.....	95
Figure 52 Raman spectra of natural (blue line) and heated (red line) spinel S3-11.	
.....	96
Figure 53 Raman spectra of natural (blue line) and heated (red line) spinel S3-18.	
.....	96
Figure 54 Raman spectra of natural (blue line) and heated (red line) spinel S3-23.	
.....	97
Figure 55 Raman spectra of natural (blue line) and heated (red line) spinel S3-27.	
.....	97
Figure 56 Raman spectra of natural (blue line) and heated (red line) spinel S4-02.	
.....	98
Figure 57 Raman spectra of natural (blue line) and heated (red line) spinel S4-03.98	
Figure 58 Raman spectra of natural (blue line) and heated (red line) spinel S4-06.99	
Figure 59 Raman spectra of natural (blue line) and heated (red line) spinel S4-14.99	
Figure 60 Raman spectra of natural (blue line) and heated (red line) spinel S5-04.	
.....	100
Figure 61 Raman spectra of natural (blue line) and heated (red line) spinel S5-09.	
.....	100

Figure 62 Raman spectra of natural (blue line) and heated (red line) spinel S5-13.	101
Figure 63 Raman spectra of natural (blue line) and heated (red line) spinel S5-22.	101
Figure 64 Raman spectra of natural (blue line) and heated (red line) spinel S6-04.	102
Figure 65 Raman spectra of natural (blue line) and heated (red line) spinel S7-08.	102
Figure 66 PL spectra of natural (blue line) and heated (red line) spinel S1-01.....	103
Figure 67 PL spectra of natural (blue line) and heated (red line) spinel S1-03.....	103
Figure 68 PL spectra of natural (blue line) and heated (red line) spinel S1-07.....	104
Figure 69 PL spectra of natural (blue line) and heated (red line) spinel S1-10.....	104
Figure 70 PL spectra of natural (blue line) and heated (red line) spinel S2-20.....	105
Figure 71 PL spectra of natural (blue line) and heated (red line) spinel S2-22.....	105
Figure 72 PL spectra of natural (blue line) and heated (red line) spinel S2-25.....	106
Figure 73 PL spectra of natural (blue line) and heated (red line) spinel S3-04.....	106
Figure 74 PL spectra of natural (blue line) and heated (red line) spinel S3-11.....	107
Figure 75 PL spectra of natural (blue line) and heated (red line) spinel S3-18.....	107
Figure 76 PL spectra of natural (blue line) and heated (red line) spinel S3-23.....	108
Figure 77 PL spectra of natural (blue line) and heated (red line) spinel S3-27.....	108
Figure 78 PL spectra of natural (blue line) and heated (red line) spinel S4-02.....	109
Figure 79 PL spectra of natural (blue line) and heated (red line) spinel S4-03.....	109
Figure 80 PL spectra of natural (blue line) and heated (red line) spinel S4-06.....	110
Figure 81 PL spectra of natural (blue line) and heated (red line) spinel S4-14.....	110
Figure 82 PL spectra of natural (blue line) and heated (red line) spinel S5-04.....	111

Figure 83 PL spectra of natural (blue line) and heated (red line) spinel S5-09.....	111
Figure 84 PL spectra of natural (blue line) and heated (red line) spinel S5-13.....	112
Figure 85 PL spectra of natural (blue line) and heated (red line) spinel S5-22.....	112
Figure 86 PL spectra of natural (blue line) and heated (red line) spinel S6-04.....	113
Figure 87 PL spectra of natural (blue line) and heated (red line) spinel S7-08.....	113
Figure 88 Normalized Fe K-edge XANES spectra of all natural and heated red spinels (S1) compared with Fe standards.	114
Figure 89 Normalized Fe K-edge XANES spectra of all natural and heated magenta spinels (S2) compared with Fe standards.	115
Figure 90 Normalized Fe K-edge XANES spectra of all natural and heated orange spinels (S3) compared with Fe standards.	116
Figure 91 Normalized Fe K-edge XANES spectra of all natural and heated red-purple spinels (S4) compared with Fe standards.	117
Figure 92 Normalized Fe K-edge XANES spectra of all natural and heated purple spinels (S5) compared with Fe standards.	118
Figure 93 Normalized Fe K-edge XANES spectra of natural and heated blue (S6) and green spinels (S7) compared with Fe standards.	119
Figure 94 Normalized V K-edge XANES spectra of all natural and heated red spinels (S1) compared with V standards.	120
Figure 95 Normalized V K-edge XANES spectra of all natural and heated magenta spinels (S2) compared with V standards.	121
Figure 96 Normalized V K-edge XANES spectra of all natural and heated orange spinels (S3) compared with V standards.	122
Figure 97 Normalized V K-edge XANES spectra of all natural and heated red-purple spinels (S4) compared with V standards.	123

Figure 98 Normalized V K-edge XANES spectra of all natural and heated purple spinels (S5) compared with V standards.	124
Figure 99 Normalized V K-edge XANES spectra of natural and heated blue (S6) and green spinels (S7) compared with V standards.	125
Figure 100 Diagram represented integrated pre-edge intensity and pre-edge peak centroid ($E-E_0$) parameter of all natural (blue dotted) and heated (red dotted) spinel samples in various Fe oxidation state and their coordination. Number [4], [5], and [6] represent a 4-fold, 5-fold, and 6-fold coordinated atoms, respectively.....	126
Figure 101 Diagram represented integrated pre-edge intensity and pre-edge peak centroid ($E-E_0$) parameter of all natural (blue dotted) and heated (red dotted) spinel samples in various V oxidation state and their coordination. Number [4], [5], and [6] represent a 4-fold, 5-fold, and 6-fold coordinated atoms, respectively.....	127
Figure 102 Diagram represented normalized Cr pre-edge XANES spectra of natural (blue lines) and heated (red lines) spinels compared with Cr(III) and Cr(VI) standards.	128

CHAPTER 1

INTRODUCTION

1.1 General statement

Tanzanite is an anisotropic mineral that have strong trichroic coloration yielding three different colors in different directions. On the other hand, spinel is an isotropic mineral that represents gem having identical color in all directions. Some previous studies investigated tanzanite and reported that V is the main coloring agent responsible for the violet-blue color of tanzanite (Anderson, 1968; Barot & Boehm, 1992; Bocchio et al., 2012; Faye & Nickel, 1971; Hurlbut, 1969; Olivier, 2006; Schmetzer & Bank, 1978-1979; Smith, 2011). However, it was subsequently suggested that trace of Ti, instead of V, may cause color in tanzanite (Olivier, 2006).

For spinel, distinct colors in spinel are caused by various trace elements. However, previous studies demonstrated that these various trace elements may affect distinct hues. Cr was suggested to yield the red color, while Fe was considered to influence the blue color (Anderson, 1937; Andreozzi et al., 2018; Atsawatanapirom et al., 2016; Carbonin et al., 1996; Chauviré et al., 2015; D'Ippolito et al., 2012; D'Ippolito et al., 2015; Gaffney, 1973; Gorghinian et al., 2013; Huong et al., 2017; Krzemnicki et al., 2017; Krzemnicki, 2011; Peretti & Günther, 2003; Shigley & Stockton, 1984; Wherry, 1929). V have never been well understood, although it may involve the orange coloration in spinel (Andreozzi et al., 2018).

Moreover, causes of color change after heating in tanzanite and spinel have never been published prior to initiation of this research. This study was then focused on causes of colors in both natural and heated gems, i.e., spinel and tanzanite. Combination of sophisticated techniques were therefore used to analyze various parameters for further interpretation. Details of these techniques will be reported later.

1.2 Objective

To investigate the significant trace elements and their color-causing roles in spinel and tanzanite.

1.3 Tanzanite

Tanzanite, a violet-blue, vanadium-bearing, variety of zoisite ($\text{Ca}_2\text{Al}_3[\text{Si}_2\text{O}_7][\text{SiO}_4]\text{O}(\text{OH})$) (Deer et al., 2013), has been long known and become a highly demanded precious stone in the world gem market owing to its fantastic color appearances. Natural tanzanites usually show strong trichroism between violet, blue, and brown (or green) colors (Figure 1). Tanzanite was first discovered in 1967 (Crowingshield, 1967) at Merelani area, north-eastern Tanzania (East Africa), by Jumanne Ngoma, a gypsum miner who was officially acknowledged by the Tanzanian Government. The deposit only covers around 7 kilometers and its estimated life expectancy for mining is, unfortunately, less than 20 years (Olivier, 2006). Moreover, natural high-quality violet-blue colored tanzanites are rare; therefore, heat treatment has been applied to lower quality stones owing to the high demand in the market.



Figure 1 Trichroism of a natural tanzanite rotated in three directions showing violet, blue, and green pleochroic colors (Photo by T. Sripoonjan, GIT).

Zoisite, including tanzanite variety, is an orthorhombic sorosilicate mineral whose ideal formula can be defined as $\text{A}_2\text{M}_3\text{Si}_3\text{O}_{12}\text{OH}$ (Dollase, 1968), where A sites

are generally substituted by divalent cations (e.g., Ca, Mn, Sr, Pb), while M sites are mainly occupied by trivalent cations (e.g., Al, Fe, Mn, Cr, and V) (Franz & Liebscher, 2004; Ghose & Tsang, 1971; Hurlbut, 1969). Its structure contains the base of edge sharing octahedral (M1,2) chain linked by double Si_2O_7 (T1, T2) and single SiO_4 (T3) tetrahedra. This edge sharing octahedral chain in zoisite also has additional M3 octahedra attaching on one side of the chain (Franz & Liebscher, 2004) (Figure 2). The structure of zoisite is slightly different from clinozoisite (a member of epidote supergroup), with the additional M3 octahedra attaching on both sides along the b-axis of the octahedral M1 chain and the octahedral M2 chain being isolated from the M3-combined M1 chain (see also Figure 2). According to this information, the Commission on New Minerals, Nomenclature, and Classification of the International Mineralogical Association (IMA) has recently defined all members of epidote supergroup as monoclinic minerals, and thus tanzanite, a variety of orthorhombic sorosilicate zoisite, no longer belongs to the epidote supergroup (Armbruster et al., 2006; Lauf, 2011; Mills et al., 2009).

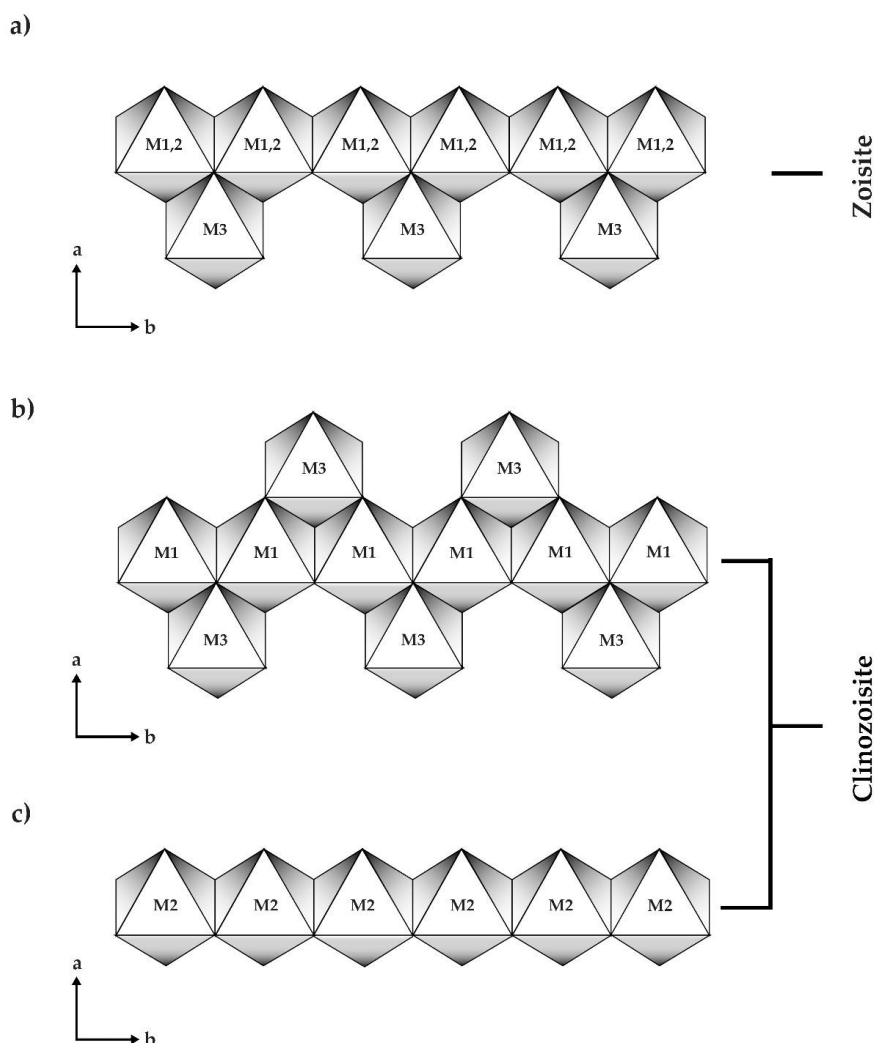


Figure 2 (a) Zoisite octahedral chain (M1, 2) combined with additional octahedra (M3) on only one side along b-direction, whereas (b) additional octahedra (M3) located on both sides of clinozoisite octahedral chain (M1) with (c) isolated octahedral chain (M2) (Modified after Franz, 2004).

1.3.1 Occurrence

Zoisite is an orthorhombic polymorph of a sorosilicate with the ideal composition $\text{Ca}_2\text{Al}_3(\text{Si}_2\text{O}_7)(\text{SiO}_4)\text{O}(\text{OH})$ and was originally classified as an epidote group. This mineral seems to be generated in rocks, primarily those undergoing medium-grade metamorphism, and is often the product of plagioclase degeneration. It is also possible to discover it in impure limestones and skarns that have been thermally metamorphosed at a low temperature. The hydrothermal alteration of

calcium-rich plagioclase (sassaritization) may also produce zoisite (Malisa, 2004; Olivier, 2006).

Zoisite is found between Meru and Kilimanjaro, in the heart of the Great Rift Valley area. The majority of zoisite that appears to be that of gem quality occurs in fault zones and in a variety of geological settings, including continental collision and subduction zones, with schists and gneisses as outcrops inward containing a small amount of transparent zoisite crystal in a variety of colors, including violet – blue, green, yellow, brown, and colorless (Olivier, 2006).

Tanzanite is a well-known mineral that is only found in one location on Earth: The Merelani region along the Lelatema fault system, which is dominated by Late Proterozoic Metasedimentary rocks, including schists, graphitic gneisses, and dolomitic marbles. According to Malisa (2004), hot hydrothermal solutions containing calcium, magnesium, carbon dioxide, sulfur, and trace elements such as V, U, Sr, Zn, and rare earth elements are injected into faults and fissures created by bedrocks to form associated minerals containing tanzanite and other colored zoisites, as well as tsavorite (grossular garnet), diopside, quartz, graphite, and calcite. Tanzanite mineralization occurred around 585 ± 28 million years ago at pressure – temperature conditions (P – T conditions) of roughly 5 – 6 kbar and $650 \pm 50^\circ\text{C}$ (Olivier, 2006). Private prospectors and miners continued to labor until 1971, after the discovery of tanzanite and its commercialization in the United States in 1968. Due to capricious exploitation and thievery, the production of tanzanite mines is uncertain for the next two decades. The mining area are roughly 5x1 kilometers and are separated into four major sections (so called block A, B, C, and D), which are regulated by the state but permit for outside venture finance. Although open pit mining is employed, more than 90% of mining is done underground (Olivier, 2006).

Many people mistakenly use the term tanzanite to refer to other colored zoisite varieties, such as brown tanzanite and green tanzanite. However, as gemologists have stated, the term “tanzanite” should be used exclusively to refer to the blue – violet colored variety of zoisite, regardless of whether the color is an origin color or an enhanced color due to the heating process (Dirlam et al., 1992). Indeed, the majority of gem-quality tanzanite sold on the market has been heat treated to

increase its color saturation. The effect of heating on the color of zoisite is determined by its trace elements, which include vanadium, chromium, titanium, and presumably a tiny amount of rare earth element (REE)(Olivier, 2006).

1.3.2 Heat treatment and coloration

Tanzanite has been heated to improve the color to sapphire-like blue color, which is highly demanded in the market (Crowningshield, 1967; McClure & Smith, 2000). It is believed that the violet-blue color in the tanzanites is owing to the presence of vanadium, which replaces aluminum in the octahedral site (Anderson, 1968; Barot & Boehm, 1992; Bocchio et al., 2012; Faye & Nickel, 1971; Hurlbut, 1969; Olivier, 2006; Schmetzer & Bank, 1978-1979; Smith, 2011). Heating tanzanite at approximately 500°C usually produces the disappearance of the yellow color in that particular direction in which the absorption around 450–460 nm is decreased, and alteration of pleochroism from trichroic to dichroic violet to blue color (Bocchio et al., 2012; Faye & Nickel, 1971; Olivier, 2006; Schmetzer & Bank, 1978-1979). Heating tanzanite at too low or too high a temperature may lead to never reaching the desirable color alteration; no color alteration is observed below 250 °C (Faye & Nickel, 1971), whereas color appears to be faded at a high temperature (Olivier, 2006). In situ heating spectroscopy was used to reveal the optimum temperature (550 °C), which causes the disappearance of the absorption around 450–460 nm (Olivier, 2006). Color alteration behavior after heat treatment can also be observed in other gemstones. For example, blue intensification and removal of green tint in blue-colored variety (aquamarine) of beryls were performed by heating at 300–700°C, leading to the reduction of Fe³⁺ to Fe²⁺. Consequently, Fe³⁺ absorption bands at 375 and 425 nm are decreased, while Fe²⁺ band at 810 nm is significantly intensified. However, heating aquamarines at higher temperature (e.g., 1100 °C) may lead to an opaque appearance, which relates to the disappearance of the 810 nm absorption band (Fridrichová et al., 2014). Another example is in diaspore (zultanite), where the chromophores involved in the variation in the color are owing to the presence of Ti-Fe and are associated with the intervalence-charge-transfer mechanism (Garcia-Guinea et al., 2005).

However, coloration in tanzanite after heat treatment has been still a questionable subject for decades. Previous researchers speculated that coloration of heated tanzanite is owing to oxidation changing of either vanadium or titanium. Vanadium may have been oxidized from V^{3+} to V^{4+} after heat treatment (Hurlbut, 1969; Schmetzer & Bank, 1978-1979); however, Olivier (2006) argued that the coloration of tanzanite after heat treatment is owing to an oxidizing of titanium from Ti^{3+} to Ti^{4+} . Moreover, a more recent inconsistency by Smith (2011) quoted that the change in color of brown tanzanite after heating is attributed to a conversion of V^{4+} to V^{3+} , as well as Bocchio et al. (2012), who also introduced that the V/Ti ratio should play an important role in the coloration of tanzanite without any concern about oxidation states of both elements in natural and heated tanzanites. Since then, the controversial topic of oxidation states of the color-causing element in tanzanite has still not been settled.

1.4 Spinel

Spinel ($MgAl_2O_4$) is a mineral consisting of mostly magnesium, aluminum, and oxygen (Sickafus et al., 1999). Spinel has variety of hues, ranging from violet to red. It is generally found in the same deposits of ruby or sapphire. However, gem colored spinel is economically found in a few places across the world, such as significant deposits of bright red in Myanmar and cornflower blue in Vietnam, with other minor sources including Sri Lanka, Tanzania, and Tajikistan (Peretti et al., 2015). The most popular varieties of natural spinel in the world gem markets are blue and red to magenta colors. These attractive colors of spinel are mainly due to Cr, Fe, and Co that substitute Mg and/or Al in its structure. Spinel, initially, is a Latin word (spina) meaning "thorn". Recently, the Commission on New Minerals, Nomenclature, and Classification (CNMNC) of the International Mineralogical Association (IMA) has approved that spinel ($MgAl_2O_4$) belongs to the spinel subgroup in the oxyspinel group of the spinel supergroup. Spinel-type structure is applied by many compounds with a ratio of 3:4 cations to anions, basically represented by the formula AB_2X_4 where A and B refer to different cations or vacancies and X refers to the occupancy of anions. For instance, X can be O^{2-} or S^{2-} . The basic structure may be described now as a slightly distorted face-centered cubic array of X anions with A cations occupying

1/8 tetrahedral site and B cations occupying 1/2 of an octahedral site within cubic unit cell. For general understanding, typical spinel formula shall be possibly written as ${}^T A {}^M B_2 X_4$ (T and M , *italic letters*, refers to tetrahedrally- and octahedrally-coordinated sites, respectively) or $A^{2+} B^{3+}_2 X_4$, since spinel subgroup (2-3 spinels) is a group of various mineral species containing different constituents of divalent cations and trivalent cations, for A and B, respectively (Biagioni & Pasero, 2014; Bosi et al., 2019; O'Neill et al., 2005; Sickafus et al., 1999; Skvortsova et al., 2015). For site occupation, some studies proposed that Ga^{3+} , In^{3+} , Ti^{3+} , Cr^{3+} , Fe^{3+} (perhaps a few Fe^{2+}), V^{3+} , Mn^{3+} , Co^{3+} , and Rh^{3+} may substitute Al^{3+} in octahedral site (Andreozzi et al., 2018; Bragg, 1915; Carbonin et al., 1996; D'Ippolito et al., 2015; Gaffney, 1973; Gorghinian et al., 2013; Juhin et al., 2008; Nishikawa, 1915; Peretti et al., 2015; Wood et al., 1968), while Fe^{2+} , Co^{2+} , Mn^{2+} , Ni^{2+} , Cu^{2+} , Zn^{2+} , and Cd^{2+} can replace Mg^{2+} in tetrahedral site (Anderson, 1937; Andreozzi et al., 2018; Bragg, 1915; Carbonin et al., 1996; D'Ippolito et al., 2012; D'Ippolito et al., 2015; Gaffney, 1973; Nishikawa, 1915; Peretti et al., 2015; Wood et al., 1968).

On the basis 32 oxygen atoms per formula unit, the normal spinel ideally has 24 cation atoms in a cubic unit cell. It is composed of A-divalent cations (8 atoms) inhabited the tetrahedral site (4-fold coordination, T), whereas B-trivalent cations (16 atoms) occupied the octahedral site (6-fold coordination, M) or described as ${}^T A_8 {}^M B_{16}^{3+} O_{32}$ which could be simplified as $A^{2+} B^{3+}_2 O_4$ or $A(BB)O_4$ (Deer et al., 2013; Peretti et al., 2015). Mg and Al can then occupy the T and M sites, respectively, for normal spinel ($MgAl_2O_4$, or $Mg(AlAl)O_4$). Heating may induce cation disorder towards inverse spinels. Consequently, half of Al in M site (8 of 16 B cations) may occupy T site alternating with 8 atoms of A cations in T site that occupied half of M site. This could be described as ${}^T Al_8^{3+} ({}^M Mg_8^{2+} + {}^M Al_8^{3+}) O_{32}$ or simply written as $Al(MgAl)O_4$ (Deer et al., 2013; Peretti et al., 2015).

Table 1 Groups of spinels (Bosi et al., 2019).

Spinel Supergroup	
Groups	Subgroup (AB₂X₄)
Oxyspinel	Spinel (A ²⁺ +B ³⁺ +O ₄)
	Ulvospinel (A ⁴⁺ +B ²⁺ +O ₄)
Thiospinel	Carrollite (A ¹⁺ +B ^{3.5+} +S ₄)
	Linnaeite (A ²⁺ +B ³⁺ +S ₄)
Selenospinel	Tyrrellite (A ¹⁺ +B ^{3.5+} +Se ₄)
	Bornhardtite (A ²⁺ +B ³⁺ +Se ₄)

1.4.1 Occurrence

The melting point of spinel is 2,135°C. (Skvortsova et al., 2015). It may develop at moderate to high temperatures and pressures in both igneous and metamorphic rocks, with ultramafic to felsic compositions, and can occur as a result of both contact and regional metamorphism. Owing to the fact that spinel is heavy and strong due to its high-density atomic lattice structure, it is found in both primary and secondary deposits. Spinel's mafic to ultramafic composition results in an abundance of iron, chromium, and titanium, resulting in a black and opaque crystal, while its felsic composition results in a colorless to vibrant crystal.

Spinel is a translucent to transparent crystal that is normally found in euhedral form without cleavage or parting (Gorghinian et al., 2013). The market's most brilliantly colored spinels are mostly mined in Mogok (Burma), Luc Yen (Vietnam), Sri Lanka, Badakshan (Afghanistan and Tajikistan), Mahenge and Matombo (Tanzania), Tunduru (Tanzania), Ilakaka (Madagascar), and Tsavo (Kenya) (Gorghinian et al., 2013; Hughes et al., 2006; Keller, 1983; Long et al., 2013; Pardieu & Soubiraa, 2006; Themelis, 2020). Spinel was discovered in primary and secondary deposits, mostly limestone and marble, in these localities. Previously published publications summarized the following information about various spinel deposits, geological locations, and occurrences:

Sri Lanka

Sri Lanka's Ratnapura gems resources are one of the most renowned gem-bearing areas in the world. Sri Lanka is a major spinel deposit that is deposited under Precambrian metamorphic basement rocks. Sri Lanka Precambrian rocks are metamorphosed and correspond to the granulite facies. They are typically metamorphosed retrogradely during the late Archean. Sri Lanka was divided into three major complexes, the Wannai Complex (western region); the Highland Complex (central region from northeast to southwest); and the Vijayan Complex (eastern region). These complexes are primarily composed of homologous rocks, such as supracrustal rocks (garnet-silimanite gneisses, metaquartzites, marble, and calc-silicate rocks), granitoid gneisses, granitic migmatites, granites, scattered metasediments (garnet-cordierite gneiss), and charnockitic rocks that transform from amphibolite to granulite facies as mentioned by several studies (Cooray, 1994; Dahanayake, 1980; Dahanayake & Ranasinghe, 1985; Gorghinian et al., 2013; Gunawardene & Rupasinghe, 1986; Mathavan et al., 2000).

Gemstone deposits in Sri Lanka provide an excellent opportunity for local miners to mine since gemstones are mostly found in residual, alluvial, eluvial, and colluvial deposits; as well as in gemstone-rich marble placers named "illam" by local miners. It is up to one meter deep and lies between 1.5 to 20 meters under the surface, covered in gravels, sands, and clays with many rock fragments. The Highland Complex seems to be the primary source of gemstones in Sri Lanka. Elahera is another gemstone field location situated within the Highland Complex. Since the 1960s, this location has also yielded several beautiful gemstones. Elahera has also been a major producer of precious gemstones on an economy basis, which included sapphire, spinel, garnet, chrysoberyl, zircon, and tourmaline along with other gemstones. Elahera's gem field contributed up to 35% of Sri Lanka's exported gemstones (Cooray, 1994; Dahanayake, 1980; Dahanayake & Ranasinghe, 1985; Gunawardene & Rupasinghe, 1986; Mathavan et al., 2000).

Vietnam

More than two decades of gem production in the Luc Yen, Yen Bai area (Northern Vietnam), Vietnam has developed into one of the world's leading producers of high-quality spinel resources (Chauviré et al., 2015; Huong et al., 2012; Senoble, 2010). In Vietnam, gemstone deposits are found in both primary and secondary deposits associated with metamorphic rocks such as marble (Senoble, 2010). Vietnam, like Thailand and Cambodia, has a similar tectonic history, which has impacted its geology and gemstone occurrence. The Paleo-Tethys closure, the Indosinian orogeny, and the Himalayan orogeny are the three major tectonic events in the past. The collision of the Indochina and South China blocks during the Permo-Triassic period and the Himalayan block during the late Cenozoic period resulted in reworked terrains composed primarily of metamorphic rocks such as weakly metamorphosed quartz-sericite schists, quartzites, marble, gneisses, medium-grade kyanite-sillimanite bearing micaschists, garnet amphibolites, and granu Marble-hosted gem deposits in Northern Vietnam are the consequence of the Indian-Eurasian plates colliding, causing severe deformation across Southeast Asia (Chauviré et al., 2015; Garnier et al., 2005; Hauzenberger et al., 2003; Kunír, 2000; Long et al., 2013). Additionally, this resulted in the formation of the Red River Shear Zone, which runs northwest-southeast.

Burma

Mogok Valley, one of the most well-known localities for the production of a large quantity of high-quality gemstones, has gained popularity for its distinctive colored spinel. Spinel was found in Mogok (Burma) in a variety of hues, including pink to red, orangey pink to orangey red, grey to purplish grey, and others. Numerous mining sites in the Mogok region contain spinel of gem grade. Spinel was found in both main and secondary deposits in Mogok (Myat Phyto et al., 2019). Mogok Stone Tract is around 700 kilometres north of Rangoon's capital city. It has been exploited for about 500 years (Keller, 1983). It is centrally located inside the Mogok Metamorphic Belt. It is composed of Paleozoic and Mesozoic high-grade metasediments and plutonic rocks that sit along the western Shan Thai terrane.

The Mogok Metamorphic Belt (or Mogok-Mandalay-Mergui Belt) is located inside the Shan-Tenasserim Massif (Eastern Highlands or Sino Burman Ranges) and is composed mainly of marble, gneiss, and calc-silicate rocks, as well as granites (Zaw et al., 2014). Spinel occurs naturally in marble in the Mogok region, but corundum occurs in both calc-silicate rocks and marble. Spinel is also found in secondary deposits, such as alluvial and eluvial placers. Spinel is often found about 6-7 meters deep in alluvial sediments (Myat Phyo et al., 2019; Myat Phyo et al., 2017).

1.4.2 Heat treatment and coloration

Color in spinel has been studied for some decades and it was demonstrated that it is basically influenced by site occupation of the main chromophores, particularly Cr, Fe, and Co. For instance, Cr³⁺, Fe³⁺ and/or V³⁺ in octahedral site were proved to cause red to magenta color whereas Co²⁺ and/or Fe²⁺ in tetrahedral site may impart blue color while the ratio of these elements also affect bluish and purplish color composition (Anderson, 1937; Andreatti et al., 2018; Atsawanapirom et al., 2016; Carbonin et al., 1996; Chauviré et al., 2015; D'Ippolito et al., 2012; D'Ippolito et al., 2015; Gaffney, 1973; Gorghinian et al., 2013; Huong et al., 2017; Krzemnicki et al., 2017; Krzemnicki, 2011; Peretti & Günther, 2003; Shigley & Stockton, 1984; Wherry, 1929). Orange spinel could be influenced by the proper amount of V³⁺ in the octahedral site (Andreatti et al., 2018). Fe²⁺ - Fe³⁺ IVCT was suggested to cause green color in spinel (Andreatti et al., 2018; D'Ippolito et al., 2015; Fregola et al., 2014). V may also have an effect on green spinels (Krzemnicki, 2011). Moreover, the additional suggestion has appeared lately in 2018 that blue color in spinel is likely due to collaboration of Co²⁺ and Fe³⁺ in the tetrahedral site with Fe²⁺ in the octahedral site (Palke & Sun, 2018). However, it should be notified that these previous studies made merely suggestion about the coloration of normal spinels without any direct evidence related to color-causing elements valency, site occupancy and their alteration after heat treatment.

In 2009, natural red spinels were subjected to heat treatment in oxidizing atmosphere for 5 hours with high temperatures varying from 1,100°C to 1,700°C but they showed no improvement of color, only turned darker (Saeseaw et al., 2009).

Subsequently, potential color enhancement of spinel was experimentally carried out above 1,200°C for more than 30 minutes using local heating method at Mogok in Myanmar (Peretti et al., 2015). Color alterations were presented in three groups including less orange and brown group, more in magenta and saturation group, and no alteration of hue, tone, and saturation group (Peretti et al., 2015). Many studies have proposed that the color shades, tints, and tones of spinels relate to specific types of trace impurities and/or their concentrations which is still a dispute. However, there is still an ambiguous and imprecise understanding of coloration in both normal and heated gem-quality spinels.



CHAPTER 2

MATERIALS AND METHODOLOGY

2.1 Tanzanite samples

Five rough tanzanite samples were collected based on their strong trichroism, which clearly showed various colors in different directions. During rotation of the sample, color changing was clearly observed such as yellowish orange to orangey yellow, greenish yellow to greenish blue to bluish green, and bluish purple along particular directions, which were marked. Subsequently, samples were then cut and polished following those marked directions and their colors were compared with the GIA standard color GemSet. Colors along these particular directions were also observed again after heating experiment. In addition, absorption spectra were analyzed using a PerkinElmer-LAMBDA 900 UV/ VIS/ NIR spectrophotometer based at Department of Earth Sciences, Kasetsart University (PerkinElmer LAMBDA); the operating conditions were set with 2.00 slit size and recording range between 200 nm and 1500 nm. Chemical compositions of the samples were analyzed using an electron probe microanalyzer (EPMA), JEOL model JXA 8100, while the heating experiment was carried out using a Linn-HT-1800-Vac high temperature furnace (Linn High Therm). Both EPMA and high temperature furnace were facilitated by Department of Geology, Chulalongkorn University. Analytical conditions of EPMA were set at 15 kV accelerating voltage and about 2.5×10^{-8} A probe current with focus electron beam (1 μm). Mineral standards and some synthetic oxide standards were selected appropriately for calibration including jadeite ($\text{NaAlSi}_2\text{O}_5$) for Na, fayalite (Fe_2SiO_4) for Fe, wallastonite (CaSiO_3) and potassium titanium phosonate (KTiPO_4) for Ti and K, synthetic corundum (Al_2O_3) for Al, synthetic periclase (MgO) for Mg, synthetic quartz (SiO_2) for Si, synthetic manganosite (MnO) for Mn, synthetic eskolaite (Cr_2O_3) for Cr, and lead vanadium germanium oxide (PbV Geoxide) for V. The heating experiment was carried out in atmospheric condition at the maximum temperature of 550 ° C with approximately a 1.8° C/ min heating rate without holding time prior to cooling down naturally in the furnace.

X-ray Absorption Spectroscopy (XAS) was investigated at Beamline 1.1W: Multiple X-ray Techniques (MXT) experimental station (Nakhon Ratchasima, Thailand) at the Synchrotron Light Research Institute (Public Organization) in Thailand (Figure 3). This beamline has a 2.2 Tesla multipole wiggler as the X-ray source and equipped with Si (111) double monochromator. A 19-element Ge detector was used as a fluorescence detector to detect probed element with low concentration. All XAS analyses were examined using $1.65 \text{ (V)} \times 2.6 \text{ (H)}$ mm beam size along the C-axis in all samples with an average of three scans to improve signal to noise ratio. A standard foil for each element was used to calibrate X-ray energies by setting the absorption edge energy of V and Ti to 5465 eV and 4966 eV, respectively. An energy scan ranging from 200 eV below to 200 eV above the absorption edge energy was used with the highest collection time of 2 seconds and 7 seconds per point for vanadium and titanium, respectively. Furthermore, V_2O_3 , V_2O_4 , Ti_2O_3 , and TiO_2 were measured as chemical standards in transmission mode using ionization chambers. However, these standards are not the same mineral group as tanzanite, and thus are used as a reference point for relative change but are unable to inform the exact oxidation state of V and Ti in the samples. The absorption edges of V and Ti from XANES spectra were then extracted from their first derivative graph and presented in a calibration curve.

X-ray Absorption Spectroscopy (XAS), a synchrotron radiation utility, is a prospective atomic probe method that is sensitive to the oxidation state and local structure of the absorbing element. XAS is divided into two sections, X-ray Absorption Near Edge Structure (XANES) and Extended X-ray Absorption Fine Structure (EXAFS). EXAFS is used to characterize the distance, coordination number, the types of surrounding atoms, and the level of disorder, whereas XANES is an effective spectroscopic method for determining oxidation state and structural symmetry. The shift of the absorption edge (edge energy, E_0) and distinctive XANES characteristics are affected by a probed element with various oxidation states and local structure (Bare, 2007; Newville, 2014; Ravel, 2015; Ruiz, 2011). As previously stated, this has induced our research to investigate gem-quality colored tanzanite and spinel for clarifying their mechanism of color-causing role.

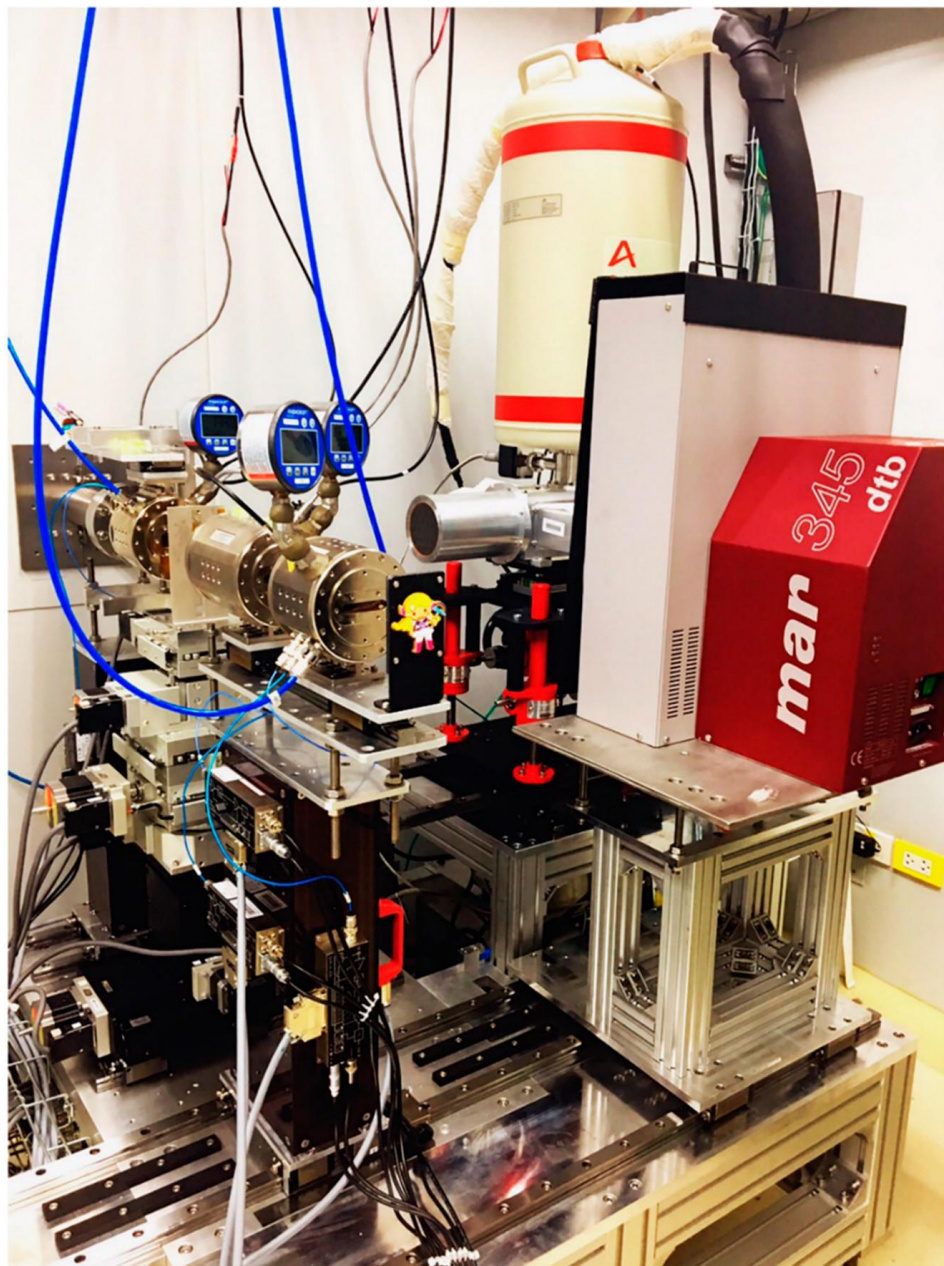


Figure 3 Beamline 1.1W: Multiple X-ray Technique station (Photo by C. Saiyasombat).

2.2 Spinel samples

Twenty-two rough spinel samples with various hues were clearly separated into 7 groups including red, magenta, orange, red-purple, purple, blue, and green. These samples were then cut and polished into wafers prior to color classification based on Munsell's color coding system. Absorption spectra were analyzed using a PerkinElmer-LAMBDA 1050 UV-VIS-NIR spectrophotometer, the operating conditions were set with a 2.00 slit size, data interval of 3.00 nm with a scan speed of 405.07 nm/min and a recording range between 250 nm and 1500 nm. Raman and photoluminescence (PL) spectra were also analyzed using a Renishaw-inVia Raman microscope with recording range of 200-2,000 Raman shift/cm⁻¹ (excitation at 532 nm edge) for Raman, and a recording range of 537-850 nm for photoluminescence (PL), respectively. These facilities are based at The Gem and Jewelry Institute of Thailand (Public Organization), GIT.

Chemical compositions of the samples were determined using an Electron Probe Micro-Analyzer (EPMA) model JXA 8100 from JEOL. The EPMA analytical conditions were set at a 15 kV accelerating voltage and a probe current of about 2.5×10^{-8} with a focus electron beam (1 μ m). Mineral standards and some synthetic oxide standards were selected suitably for calibration, including zinc oxide (ZnO) for Zn, fayalite (Fe₂SiO₄) for Fe, wollastonite (CaSiO₃) for Ca, synthetic corundum (Al₂O₃) for Al, synthetic periclase (MgO) for Mg, synthetic quartz (SiO₂) for Si, synthetic rutile (TiO₂) for Ti, synthetic manganosite (MnO) for Mn, synthetic eskolaite (Cr₂O₃) for Cr, cobalt oxide (CoO) for Co, gadolinium gallium garnet (Ga), and lead vanadium germanium oxide (PbV Geoxide) for V. Three analytical spots in each sample were carried out for statistical analysis.

A heating experiment was carried out using a Linn-HT-1800-Vac high temperature furnace in atmospheric conditions at the maximum temperature of 1,200°C with holding time of 1 hour and cooling down naturally. EPMA and the electric furnace were facilitated by the Department of Geology, Faculty of Science, Chulalongkorn University.

XAS was investigated at Beamline 1.1W: Multiple X-ray Techniques (MXT) experimental station at the Synchrotron Light Research Institute (Public Organization) in Thailand. This beamline has a 2.2 Tesla multipole wiggler as the X-ray source and equipped with Si (111) double monochromator. The 19-element Ge detector was used as a fluorescence detector to detect probed element with low concentration. All XAS analysis were examined with an average of 3-5 scans to improve signal to noise ratio. Analytical parameters for iron, chromium and vanadium were presented in Table 2.

Table 2 XAS parameters for analyses of iron, chromium, and vanadium.

Parameters	Iron	Chromium	Vanadium
Edge energy (E₀)	7112 eV	5989 eV	5465 eV
Number of scans	3-5	3-5	3-5
Energy (eV)	-80, -15,30,60,90,200	-80, 15,30,60,90,200	-80, 15,30,60,90,200
Energy step (eV)	5,0.2,0.4,2,4	5,0.2,0.4,2,4	5,0.2,0.4,2,4
Time step (sec.)	1-4	1-4	1-4
Beam size	2x3/4x3/4x4 mm	2x3/4x3/4x4 mm	2x3/4x3/4x4 mm

Fe-foil, Cr-foil, and V-foil, as well as FeO, Fe₂O₃, Cr₂O₃, CrO₃, V₂O₃ and V₂O₄ were used as chemical standards for examining oxidation state of Fe, Cr, and V in spinel. Absorption edges of Fe, Cr, and V from XANES spectra were then extracted from their normalized XANES spectra. Pre-edge parameters diagram also presented for the oxidation state and/or co-ordination indication which indicated a variation of assuming binary mixtures of respective endmembers. These procedures have been proposed by many previous researchers (Bunnag et al., 2020; Chaurand et al., 2007; Dubrail & Farges, 2009; Farges, 2009; Giuli et al., 2004; Huggins et al., 1999; Peterson et al., 1996; Peterson et al., 1997; Wilke et al., 2001; Wilke et al., 2005). Fitting the spectral region before the pre-edge with a Victoreen function and subtracting this as background absorption were used to normalize the XANES spectra. The pre-edge was modeled using Lorentzian and line function that was used to interpolate the background data a few eV before and after the pre-edge feature. Normalized height, position, half-width, centroid, and integrated intensity were

derived from the pre-edges (Wilke et al., 2001) using the XAS Viewer program (Newville, 2013). The pre-edge information was gathered by calculating the total integrated area (sum of the integrated intensities of each component) and the centroid (area-weighted average of the pre-edge peak location) of the background subtracted pre-edge (Wilke et al., 2001; Wilke et al., 2005). The location of the centroid and its integrated intensity are the most relevant features. The approach for determining the pre-edge peak features in XANES spectra was derived from Wilke et al. (2001), who developed a methodology described by several previous researchers by subtracting background and adding components of Gaussian model fitting, resulting in the pre-edge fit centroid and integrated intensity (pre-edge peak area). This is apparently the most accurate method for determining the symmetry and oxidation state of Fe XANES spectra, which was utilized in this study. The examination of V pre-edge XANES was primarily performed by applying the Chaurand et al. (2007), Giuli et al. (2004), and Farges et al. (1996) methodology approaches, with the purpose of identifying the ratio of mixed oxides and site symmetry. Several determinations were proposed for analyzing Cr pre-edge XANES spectra, however, this research will be analyzed based on Peterson et al. (1996; 1997) procedure which determined the pre-edge height on normalized XANES spectra. Additional information will be given in the later section.

CHAPTER 3

TANZANITE

3.1 Results

3.1.1 General gemological properties

The physical properties of all tanzanite samples are summarized in Table 3. They ranged from 0.565 to 1.26 carats in weight with specific gravity (S.G.) of 3.32–3.38. Refractive indices (R.I.) and birefringence fell within the ranges of 1.691–1.701 and 0.08–0.09, respectively. All samples were inert under UV lamp. Their natural trichroic colors and dichroic colors after heating observed along different directions are presented in Figure 4.

Table 3 General properties of tanzanite samples.

Sample/Properties	T04	T06	T09	T11	T12
Refractive Indices	1.692–	1.691–	1.691–	1.693–	1.692–
	1.700	1.700	1.700	1.701	1.701
Birefringence	0.008	0.009	0.009	0.008	0.009
Specific Gravity	3.33	3.35	3.37	3.32	3.38
UV Fluorescence	Inert	Inert	Inert	Inert	Inert

3.1.2 Mineral chemistry

Major and trace compositions, resulting from EPMA analyses, are presented in Table 4. A. P. F. U. were recalculated on the basis of 13 oxygen atoms. Three analytical spots were carried out on the C-axis (yellowish color). SiO_2 , Al_2O_3 , and CaO ranged from about 39.0 to 40.5 wt% , 33.0 to 34.0 wt% , and 24.0 to 24.5 wt% , respectively. V_2O_3 content yielded <0.5 wt% , whereas TiO_2 content was even lower than 0.05 wt% , and other trace elements including MgO , Cr_2O_3 , FeO , MnO , Na_2O , and K_2O were negligible and mostly lower than 0.1 wt% . Apart from the major contents of Si, Al, and Ca, the EPMA data also indicated that V is the most significant trace chromophore in these samples.



Table 4 Electron probe microanalyzer (EPMA) analyses of major and trace compositions of tanzanite samples under this investigation.

Sample/Oxides (wt%)	T04_1	T04_2	T04_3	T06_1	T06_2	T06_3
SiO ₂	39.78	39.04	39.04	40.02	40.21	39.79
TiO ₂	0.00	0.03	0.00	0.03	0.00	0.00
Al ₂ O ₃	33.48	33.02	33.47	33.19	33.21	33.99
V ₂ O ₃	0.39	0.43	0.38	0.35	0.38	0.39
Cr ₂ O ₃	0.00	0.07	0.08	0.05	0.02	0.08
FeO	0.00	0.00	0.00	0.03	0.00	0.01
MnO	0.00	0.01	0.00	0.00	0.02	0.00
MgO	0.05	0.04	0.03	0.05	0.03	0.05
CaO	24.26	24.28	24.12	24.38	24.56	24.45
Na ₂ O	0.00	0.01	0.00	0.00	0.01	0.00
K ₂ O	0.01	0.00	0.01	0.01	0.00	0.00
Total	97.97	96.94	97.13	98.11	98.44	98.76
Based on 13 oxygens						
Si	3.128	3.110	3.101	3.144	3.149	3.107
Ti	0.000	0.002	0.000	0.002	0.000	0.000
Al	3.104	3.100	3.132	3.073	3.065	3.127
V	0.025	0.027	0.024	0.022	0.024	0.024
Cr	0.000	0.005	0.005	0.003	0.001	0.005
Fe	0.000	0.000	0.000	0.002	0.000	0.001
Mn	0.000	0.001	0.000	0.000	0.002	0.000
Mg	0.005	0.005	0.003	0.006	0.004	0.006
Ca	2.045	2.072	2.053	2.052	2.061	2.045
Na	0.000	0.002	0.000	0.000	0.002	0.000
K	0.001	0.000	0.001	0.001	0.000	0.000
Total	8.308	8.323	8.319	8.305	8.307	8.315

(< 0.05 wt% = below detection limit)

Table 4 (Cont.)

Sample/Oxides (wt%)	T09_1	T09_2	T09_3	T11_1	T11_2	T11_3
SiO ₂	39.86	39.42	39.50	40.12	40.49	39.43
TiO ₂	0.05	0.00	0.00	0.00	0.02	0.00
Al ₂ O ₃	33.21	33.72	33.83	33.23	33.17	33.09
V ₂ O ₃	0.29	0.20	0.29	0.25	0.25	0.25
Cr ₂ O ₃	0.00	0.07	0.00	0.02	0.00	0.05
FeO	0.00	0.00	0.00	0.06	0.00	0.03
MnO	0.06	0.03	0.03	0.02	0.00	0.00
MgO	0.04	0.05	0.05	0.02	0.01	0.01
CaO	24.64	24.34	24.34	24.47	24.43	24.37
Na ₂ O	0.00	0.00	0.02	0.00	0.02	0.00
K ₂ O	0.01	0.01	0.00	0.00	0.01	0.02
Total	98.15	97.84	98.06	98.19	98.41	97.94
Based on 13 oxygens						
Si	3.134	3.107	3.105	3.149	3.168	3.128
Ti	0.003	0.000	0.000	0.000	0.001	0.000
Al	3.077	3.132	3.135	3.074	3.059	3.093
V	0.018	0.013	0.018	0.016	0.016	0.016
Cr	0.000	0.005	0.000	0.001	0.000	0.003
Fe	0.000	0.000	0.000	0.004	0.000	0.002
Mn	0.004	0.002	0.002	0.001	0.000	0.000
Mg	0.004	0.006	0.006	0.002	0.001	0.001
Ca	2.075	2.055	2.050	2.058	2.048	2.071
Na	0.000	0.000	0.003	0.000	0.003	0.001
K	0.001	0.001	0.000	0.000	0.001	0.002
Total	8.316	8.319	8.320	8.306	8.296	8.317

(< 0.05 wt% = below detection limit)

Table 4 (Cont.)

Sample/Oxides (wt%)	T12_1	T12_2	T12_3
SiO ₂	39.46	39.77	39.25
TiO ₂	0.00	0.00	0.03
Al ₂ O ₃	33.42	33.26	33.25
V ₂ O ₃	0.18	0.06	0.21
Cr ₂ O ₃	0.00	0.00	0.00
FeO	0.03	0.00	0.04
MnO	0.01	0.01	0.01
MgO	0.05	0.05	0.04
CaO	24.33	24.35	24.55
Na ₂ O	0.01	0.01	0.00
K ₂ O	0.01	0.01	0.00
Total	97.48	97.52	97.38
Based on 13 oxygens			
Si	3.120	3.141	3.112
Ti	0.000	0.000	0.002
Al	3.115	3.096	3.107
V	0.011	0.004	0.013
Cr	0.000	0.000	0.000
Fe	0.002	0.000	0.002
Mn	0.001	0.001	0.001
Mg	0.006	0.006	0.004
Ca	2.061	2.060	2.086
Na	0.001	0.001	0.000
K	0.001	0.001	0.000
Total	8.317	8.310	8.327

(< 0.05 wt% = below detection limit)

3.1.3 Heat treatment

As expected, heating with optimum temperature (550 ° C) dramatically effected the colors of tanzanite in all directions (Figure 4). Yellow tints in the C-axis were obviously removed after the heating experiment. Figure 4 also presents the color codes of natural colors and colors after heat treatment along the three main directions; for instance, the sample T04 yielded color alteration from yellowish orange (yO 6/3) to violet (V7/4) along the c-axis, green-blue (GB 6/1) to bluish violet (bV 6/5) along the b-axis, and bluish purple (bP 6/3) to violet (V7/4) along the a-axis. In general, their trichroic colors appeared to be changed to dichroic colors after heat treatment. The C-axis direction always shows the strongest color modification compared with the other direction.










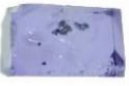






















Axis Samples	a-axis		b-axis		c-axis	
	Natural	Heated	Natural	Heated	Natural	Heated
T04						
	bP 6/3	V 7/4	GB 6/1	bV 5/5	yO 6/3	V 7/4
T06						
	bP 6/3	V 6/4	GY 5/3	vB 4/6	yO 6/4	V 7/4
T09						
	bP 2/3	V 6/4	GY 5/3	vB 4/6	oY 3/5	V 6/4
T11						
	bP 3/3	V 5/5	oY 3/2 zoning gB 5/4	vB 6/4	oY 3/5	V 5/2
T12						
	bP 6/3	V 5/5	gY 4/3	vB 6/4	Y 8/3	V 4/5

Figure 4 All tanzanite samples show natural trichroic colors including purple, green, and yellow dominating along the directions of a-, b-, and c-axes, respectively. All samples turned to dichroic coloration between violet color (along the a- and c-axes) and blue color (along the b-axis) after the heating experiment.

3.1.4 UV-VIS-NIR spectroscopy

UV-VIS-NIR spectroscopy revealed a representative spectrum of natural and heated tanzanite sample (Figure 5). This natural tanzanite sample T04 showed the highest absorption band with a peak at about 460 nm (violet-blue range), particularly in the c-axis, whereas the absorption band with a peak at around 585–600 nm (yellow range) appeared to be the most typical in all directions. In fact, the absorption band with a peak at 460 nm also presented slightly in the a- and b-axes, but this absorption was significantly decreased in all directions after heating. On the other hand, the absorption band (peak around 585–600 nm) still remained as shown in Figure 5.

In summary, decreasing the absorption band with a peak at 460 nm (violet to blue range) was obviously observed in all directions after heating experiment, whereas the absorption band with a peak around 585–600 nm was unchanged. Only in c-axis, was the absorption band with a peak at 585 nm slightly increased after heating. It should be notified that natural tanzanite usually shows an important absorption band with a peak around 460 nm, which is possibly caused by either vanadium or titanium, as suggested by previous researchers (Anderson, 1968; Barot & Boehm, 1992; Bocchio et al., 2012; Faye & Nickel, 1971; Hurlbut, 1969; Olivier, 2006; Schmetzer & Bank, 1978-1979; Smith, 2011).

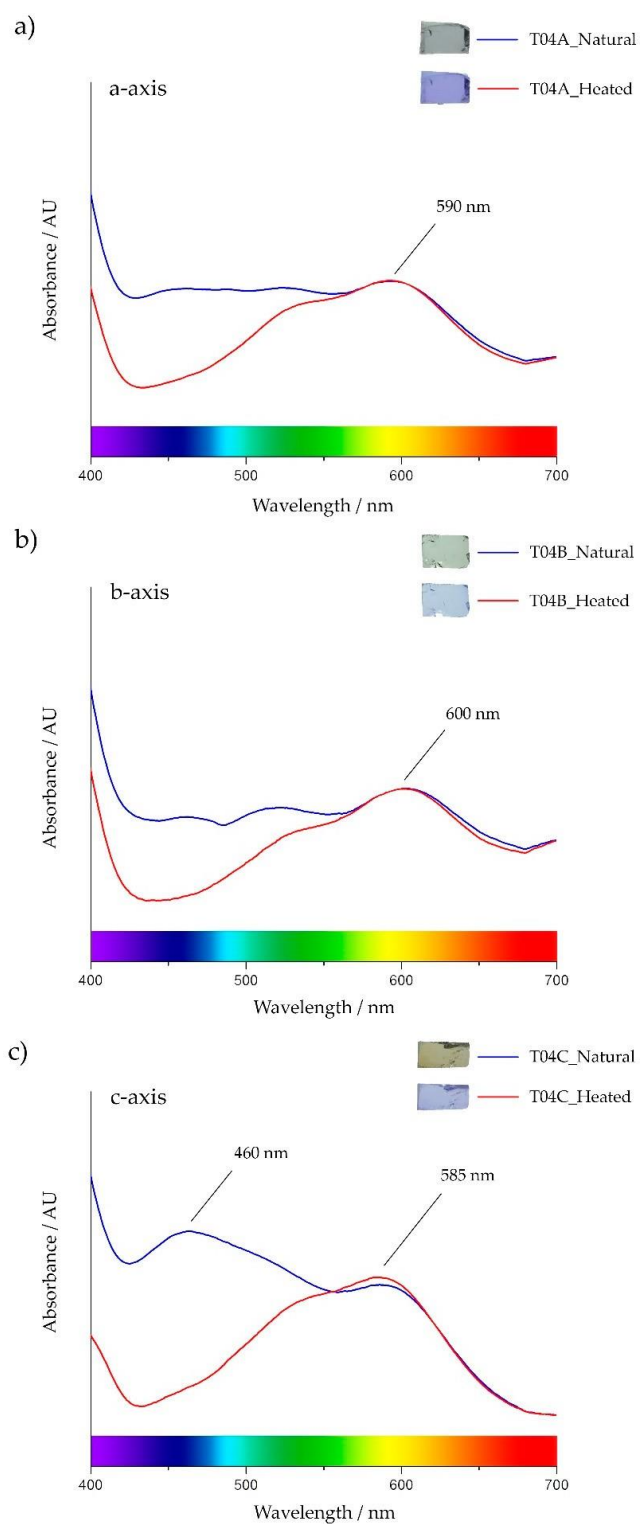


Figure 5 Representative absorption spectra of natural (blue spectrum) and heated (red spectrum) along the a-axis (a), b-axis (b), and c-axis (c) of a tanzanite sample (T04) (visible spectrum modified after Nassau (2001)).

3.1.5 X-ray absorption spectroscopy

Edge energy (E₀) data in the natural tanzanite were increased to higher energy of vanadium after heat treatment, as summarized in Table 5. For instance, edge energy of natural tanzanite sample T06 was 5478.95 eV and subsequently reached up to 5479.15 eV. On the other hand, titanium in the same sample appeared to be decreased in edge energy from 4981.00 eV in natural tanzanite to 4980.70 eV after heating experiment (Table 5). All analytical data of E₀ obtained from all samples are compared in the graphic presentation in Figures 6 and 7 for V and Ti, respectively. Most samples obviously showed increasing edge energy of vanadium and decreasing edge energy of titanium. The change in edge energy refers to changing of the oxidation state; the higher energy indicates the higher oxidation state (Newville, 2014). Therefore, V tended to be oxidized after heating at 550 °C in atmospheric environment, whereas Ti behaved in the other way.

Table 5 Edge energy values of V and Ti obtained from K-edge X-ray absorption near edge structure (XANES) spectra of tanzanite samples before and after the heating experiment.

Samples	Edge Energy of V (eV)		Edge Energy of Ti (eV)	
	Before	After	Before	After
T04	5479.00	5479.02	4981.92	4979.20
T06	5478.95	5479.15	4981.00	4980.70
T09	5478.82	5478.97	4981.40	4980.90
T11	5478.75	5479.02	4980.83	4979.30
T12	5478.80	5478.95	4980.73	4980.63

(Margin of error ± 0.075 eV)

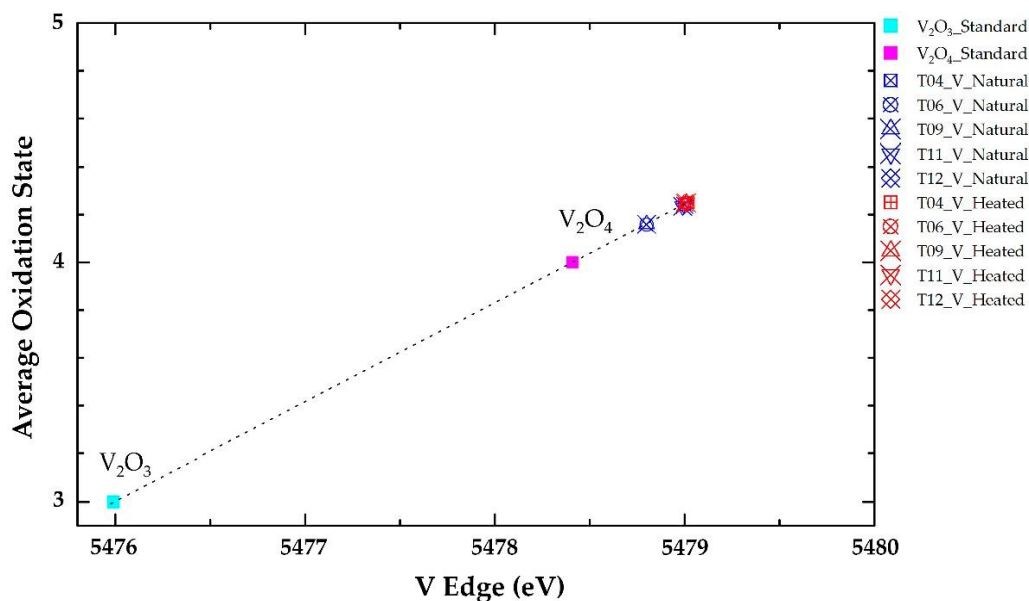


Figure 6 Plots of absorption edge energy (E_0) of vanadium in natural tanzanite samples and after heating experiment with a calibration curve (dotted line) fitted by standard V_2O_3 and V_2O_4 ; oxidation states of vanadium in most samples appear to increase after heating.

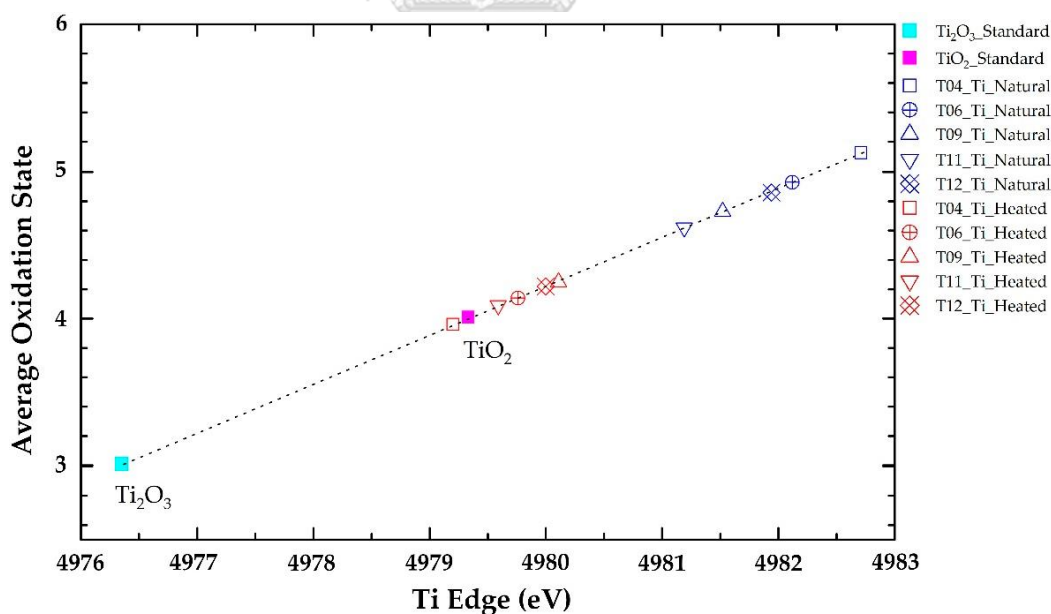


Figure 7 Plots of absorption edge energy (E_0) of titanium in natural tanzanite samples and after heating experiment with a calibration curve (dotted line) fitted by standard Ti_2O_3 and TiO_2 ; oxidation states of titanium tend to decrease after heating.

3.2 Discussion

V and Ti have previously been proposed to be the main chromophore allocated within Al-octahedral site of tanzanite; both elements could have changed oxidation states after heating (Anderson, 1968; Dollase, 1968; Faye & Nickel, 1971; Hurlbut, 1969; Olivier, 2006; Schmetzer & Bank, 1978-1979). V^{3+} should be oxidized to V^{4+} after heating and cause a sapphire-like blue color (Crowningshield, 1967; Hurlbut, 1969; McClure & Smith, 2000; Schmetzer & Bank, 1978-1979). However, Olivier (2006) has later suggested that heating could oxidize Ti rather than vanadium in tanzanite. He has also proposed that Ti^{3+} is responsible for the red/green/blue color in the natural tanzanite and appears to be oxidized to colorless Ti^{4+} after heating.

On the basis of the results of this investigation, natural tanzanite showed a mainly purplish blue, green-blue to green-yellow, and yellow to yellowish orange in the a-, b-, and c-axes, respectively. After the heating experiment, the yellow to yellowish orange color along the c-axis turned into violet and the bluish purple changed to violet along the a-axis, whereas the yellowish/greenish blue was altered to a blue-dominated color in the b-axis. Consequently, its pleochroism changed from trichroic to dichroic coloration, accordingly. Therefore, green and/or yellow colors were conclusively removed by heating at 550 °C (see Figure 4). The most significant change can be observed along the c-axis, which contained the most intense yellow component in the natural stone.

3.2.1 Absorption spectra

In general, different absorption spectra of natural tanzanite samples appear in each particular direction (a-, b-, or c-axis), for example, in sample T04 (Figure 5). A strong absorption band in the yellow region (peak at 585–600 nm) can be recognized in all directions. This absorption band should involve violet coloration, which can be explained using the role of complementary colors suggested by Nassau (2001). The visible color spectrum arranged in the triangular presents pairs of complementary colors on the opposite side such as blue-orange, green-red, and yellow-violet. Each pair of complementary colors provides a white color or no color.

Therefore, selective absorptions in the visible spectrum may yield the combination of colors of which their complementary pairs are absorbed (Nassau, 2001). The main absorption band with a peak at about 585–600 nm (yellow range) still remains after heating; therefore, it should be the main cause of violet coloration, particularly in heated tanzanite. For instance, violet (V7/4 in sample T04) appears along a- and c-axes, which is clearly caused by such an absorption band (see Figure 5a, 5c). On the other hand, the peak of this absorption band slightly shifts towards the orange range (600 nm) in the b-axis (see Figure 5b), which leads to bluish violet (bV5/5) being present, based on the same principle.

Regarding colors in natural samples, the yellowish orange (yO 6/4) color of natural tanzanite sample T04 in the c-axis is clearly affected by very strong absorption band peaked around 460 nm covering the blue region (Figure 5c), which this absorption pattern decreases significantly in both the a- and b-axes, yielding bluish purple (bP 6/3) and green-blue (GB 6/1), respectively. This absorption band is clearly an indication of natural tanzanite (unheated), as also suggested by previous workers (Anderson, 1968; Barot & Boehm, 1992; Bocchio et al., 2012; Crowningshield, 1967; Faye & Nickel, 1971; Hurlbut, 1969; Schmetzer & Bank, 1978-1979; Smith, 2011).

Consequently, it is implicit that the trichroic bluish purple, green-blue to green-yellow, and yellow to yellowish orange colors of the a-, b-, and c-axes of natural tanzanite are obviously influenced by different intensities of absorption band (peaked around 460 nm) in the blue region, as explained above. This absorption band is absent in all directions after heating at 550 °C, which leads to dichroic violet (a- and c-axes) and blue (b-axis). In addition, a more stable absorption band in the yellow region (peak at 585–600 nm) presented in all directions of both natural and heated tanzanite should be the main color causing blue-violet. A slight shifting of the peak of this absorption band from 585 to 600 nm may induce different shades such as purplish to bluish, accordingly.

3.2.2 X-ray absorption spectroscopy and chemistry

XAS analyses give rise to new evidence indicating that the edge energy of vanadium in most samples changes to the higher oxidation state, whereas titanium yields lower edge energy and decreases the oxidation state after heat treatment (Table 5, Figures 6 and 7). It has been suggested by Olivier (2006) that Ti^{3+} causing red/green/blue color in natural tanzanite should be oxidized to Ti^{4+} , then contributing no color. However, the results obtained from this study indicate that the oxidation state of titanium is likely decreased after heat treatment. In fact, this study reveals the increasing of vanadium edge energy in most samples, which clearly relates to more intense violet and blue coloration, which is a result of extreme decreasing of absorption in the blue region. EPMA analyses indicate that all tanzanite samples are similar in composition and close to the idealized formula $Ca_2Al_3[Si_2O_7][SiO_4]O(OH)$.

Their major compositions are composed, on the basis of 13 oxygen atoms of Si (3.1–3.2 apfu), Al (3.1 apfu), and Ca (2.0–2.1 apfu). Moreover, they also confirm that vanadium contents (up to 0.027 apfu) are much higher than titanium (≤ 0.002 apfu) in these tanzanite samples (see Table 4). Electron microprobe analyses of tanzanite in this present work represent the average results of 0.29 wt% V_2O_3 , 0.01 wt% TiO_2 , 0.03 wt% Cr_2O_3 , and 0.01 wt% FeO , which are compatible with those recently reported by Bocchio et al. (2012), including about 0.39 wt% V_2O_3 , 0.01 wt% TiO_2 , 0.07 wt% Cr_2O_3 , and 0.00 wt% FeO , as well as those of Barot and Boehm [15], who earlier presented averages of 0.15 wt% V_2O_3 , 0.03 wt% TiO_2 , 0.08 wt% Cr_2O_3 , and 0.01 wt% Fe_2O_3 . However, it is in contrast to those reported by Olivier (2006), who presented the lower average V_2O_3 contents of 0.06 wt%, but comparable averages of 0.03 wt% TiO_2 , 0.04 wt% Cr_2O_3 , and 0.02 wt% FeO . V/Ti ratios obtained from this work show that V contents are about 13 to 40 times greater than Ti content, which fits well with the color-causing model of tanzanites. V content was quoted to be 60 times greater than Ti content in blue colored samples but decreasing to 16 to 5 times was observed in yellowish brown and greenish yellow colored zoisites (Bocchio et al., 2012; Faye & Nickel, 1971; Olivier, 2006).

Moreover, the V_2O_3/Cr_2O_3 ratios of all tanzanites in this work are greater than two, which typically yields a blue color, whereas lower than two is usually detected in green tanzanite (Kammerling et al., 1995). Therefore, it is clear that the main chromophore in these samples is vanadium, which appears to have contributed to violet and blue coloration after heat treatment.



CHAPTER 4

SPINEL

4.1 Results

4.1.1 General gemological properties

Physical properties of all spinel samples are summarized in Table 6. They range from 0.33 to 4.68 carats in weight, with a specific gravity (S.G.) of 3.24-3.68. Refractive index (R.I.) is within the range of 1.716-1.722. All samples are inert under short-wave UV light while some show red fluorescent under long-wave UV light.

Table 6 Physical properties of spinel samples in this investigation.

Sample/ properties	Color Group	Refractive Index	Specific gravity	UV fluorescence		Color code	
				Short wave	Long wave	Natural	Heated
S1-01	S1 Red	1.722	3.52	inert	inert	5R 4/14	5R 3/10
S1-03		1.720	3.55	inert	red	10R 3/10	10R 3/8
S1-07		1.721	3.62	inert	red	10R 2/8	10R 1/8
S1-10		1.715	3.47	inert	inert	10R 2/12	10R 3/8
S2-20	S2 Magenta	1.718	3.42	inert	red	7.5RP 5/8	7.5RP 5/6
S2-22		1.718	3.66	inert	inert	10RP 5/8	2.5R 5/6
S2-25		1.718	3.55	inert	red	5R 5/8	7.5R 4/6
S3-04	S3 Orange	1.718	3.68	inert	inert	10R 5/16	10R 5/12
S3-11		1.718	3.50	inert	inert	2.5YR 5/12	2.5YR 6/6
S3-18		1.716	3.59	inert	red	2.5YR 4/10	2.5YR 5/6
S3-23		1.718	3.56	inert	inert	2.5YR 4/8	2.5YR 3/6
S3-27		1.718	3.56	inert	red	2.5YR 4/12	2.5YR 3/6
S4-02	S4 Red-purple	1.715	3.62	inert	inert	2.5R 4/6	7.5R 3/6
S4-03		1.718	3.21	inert	inert	2.5R 6/4	7.5R 5/6
S4-06		1.719	3.61	inert	inert	2.5YR 3/8	2.5YR 3/6
S4-14		1.718	3.60	inert	red	10R 3/8	5R 3/8
S5-04	S5 Purple	1.716	3.52	inert	inert	10P 5/6	2.5RP 5/4
S5-09		1.718	3.62	inert	inert	10RP 2/8	10RP 3/4
S5-13		1.720	3.50	inert	inert	2.5RP 5/6	2.5RP 6/4
S5-22		1.716	3.57	inert	red	7.5RP 7/4	10RP 7/4
S6-04	S6 Blue	1.720	3.68	inert	inert	10PB 3/2	10PB 2/2
S7-08	S7 Green	1.720	3.63	inert	inert	2.5GY 6/4	2.5GY 6/4

4.1.2 Mineral chemistry

Major and some trace oxide compositions determined by EPMA are summarized in Table 7, along with their atomic proportions recalculated on the basis of 32 oxygen atoms which an ideal of 24 total cations are theoretically expected to allow 8 cations in A sites (4-fold coordination) and 16 cations in B sites (6-fold coordination), accordingly (Deer et al., 2013). Based on EPMA analyses of spinel samples, MgO and Al₂O₃ contents range between 25.92-28.74 wt% (equivalent to 7.490-8.143 atoms per formula unit, apfu) and 68.90-70.97 wt% (15.642-16.058 apfu), respectively. Consequently, all spinels under this study generally present summation of both main cations (Mg and Al) with an average of 23.980 apfu close to the ideal formula. Moreover, both cations could be allocated for A and B sites with averages of 7.989 and 15.990 apfu, therefore, some trace elements should be allowed to occupy the little vacancies in both sites, appropriately. These trace components reveal various ranges in spinel collection as reported below. The highest average Fe content is recognized in blue spinel at 2.66 wt% oxides (0.432 apfu), followed by green, magenta, red-purple, purple, and red spinel group at about 1.14, 1.04, 0.92, 0.85, and 0.11 wt% oxide, equivalent to 0.183, 0.167, 0.147, 0.136, and 0.017 apfu, respectively. The lowest Fe content is observed in orange spinel group at avg. 0.09 wt% oxide (0.014 apfu). The average Cr content of red spinel is 0.82 wt% oxide (0.125 apfu), followed by magenta spinels at avg. 0.23 wt% oxide (0.035 apfu), whereas much lower averages are recorded at 0.08 wt% (0.012 apfu) in red-purple spinels, at 0.07 wt% (0.010 apfu) in purple, at 0.06 wt% (0.009 apfu) in orange spinels, and 0.02 wt% (0.004 apfu) in blue spinel, respectively. On the other hand, Cr is undetectable in green spinel. V reveals the highest average oxide content of 1.05 wt% (0.162 apfu) in red spinels, followed by orange spinels at avg. 0.70 wt% (0.106 apfu), red-purple spinels at avg. 0.31 wt% (0.048 apfu), magenta spinels at avg. 0.11 wt% (0.017 apfu), purple and blue spinels at 0.08 wt% (0.012 apfu) and 0.05 wt% (0.008 apfu), respectively. On the other hand, green spinel yields the lowest V content of 0.01 wt% oxides (0.002 apfu) (Table 7).

Despite the high Cr concentration (avg. 0.82 wt% oxide, 0.125 apfu), V content (avg. 1.05 wt% oxide, 0.162 apfu) is equally high in red spinels. Therefore,

both elements are obviously much higher than Fe (avg. 0.11 wt% oxide, 0.017 apfu). Orange spinels have the greatest V dominance (avg. 0.70 wt% oxide, 0.106 apfu) compared to Fe (avg. 0.09 wt% oxide, 0.014 apfu) and Cr (avg. 0.06 wt% oxide, 0.009 apfu). Magenta spinels reveal the greatest concentration of Fe (avg. 1.04 wt% oxide, 0.167 apfu) > Cr (avg. 0.23 wt% oxide, 0.035 apfu) > V (avg. 0.11 wt% oxide, 0.017 apfu). Red-purple spinels yield average oxides of 0.92 wt% Fe (0.147 apfu) > 0.31 wt% V (0.048 apfu) > 0.08 wt% Cr (0.012 apfu). Purple spinels present average oxides of 0.85 wt% Fe (0.136 apfu) > 0.08 wt% V (0.012 apfu) > 0.07 wt% Cr (0.010 apfu). Blue spinels contain average oxides of 2.66 wt% Fe (0.432 apfu) > 0.05 wt% V (0.008 apfu) > 0.02 wt% Cr (0.004 apfu), Green spinel gives average oxides of 1.16 wt% Fe (0.183 apfu) > 0.02 wt% V (0.002 apfu) without Cr. It should be notified that blue spinels under this research seem likely Fe-related blue spinels instead of Co-related blue spinels. Thus, these spinel varieties can be categorized into two groups, Cr-V-related color spinels (i.e., red and orange spinels) and Fe-related color spinels (i.e., magenta, red-purple, purple, blue and green spinels).

Although, Ga and Zn yield the highest concentrations of 2.57 wt% oxide (0.314 apfu) and 1.02 wt% oxide (0.145 apfu) in a few samples, they are inconsistency in most spinel varieties (Table 7). Therefore, they might insignificantly relate to coloration in these spinels. In addition, other trace elements with analyses lower than 0.2 wt% oxides, such as Mn, Co, and Ca, are negligible. As the result, it also supported that Co in the blue spinel of this study is below the detection limit.

Table 7 EPMA analyses of major and trace elements of spinel samples.

Oxide (wt%)/ Samples	S1 Red				S2 Magenta		
	S1-01	S1-03	S1-07	S1-10	S2-20	S2-22	S2-25
SiO ₂	0.00	0.00	0.00	0.01	0.01	0.00	0.02
TiO ₂	0.02	0.04	0.10	0.06	0.03	0.00	0.02
Al ₂ O ₃	69.51	69.52	68.90	69.73	69.82	70.92	70.97
V ₂ O ₃	0.47	1.07	1.06	1.60	0.06	0.12	0.15
Cr ₂ O ₃	1.84	0.25	1.02	0.19	0.23	0.22	0.25
Ga ₂ O ₃	1.53	0.00	0.00	0.00	0.00	0.00	0.00
FeO	0.18	0.07	0.17	0.02	1.00	1.14	0.98
MnO	0.00	0.00	0.00	0.02	0.03	0.01	0.02
MgO	26.38	27.20	27.39	28.17	27.49	26.71	26.74
CoO	0.00	0.01	0.00	0.00	0.01	0.00	0.00
ZnO	0.09	1.02	0.96	0.03	0.08	0.00	0.06
CaO	0.01	0.01	0.01	0.00	0.01	0.01	0.02
Total	100.03	99.22	99.60	99.82	98.75	99.12	99.24
Based on 32 oxygens							
Si	0.000	0.000	0.000	0.002	0.003	0.000	0.003
Ti	0.003	0.007	0.015	0.008	0.004	0.000	0.003
Al	15.728	15.799	15.642	15.692	15.886	16.058	16.048
V	0.072	0.166	0.163	0.245	0.010	0.018	0.023
Cr	0.279	0.039	0.155	0.029	0.034	0.034	0.038
Ga	0.188	0.000	0.000	0.000	0.000	0.000	0.000
Fe	0.028	0.010	0.027	0.003	0.161	0.182	0.157
Mn	0.000	0.000	0.000	0.002	0.004	0.002	0.004
Mg	7.551	7.820	7.865	8.021	7.913	7.650	7.649
Co	0.000	0.002	0.000	0.000	0.001	0.000	0.000
Zn	0.013	0.145	0.137	0.004	0.011	0.000	0.009
Ca	0.002	0.004	0.002	0.000	0.003	0.002	0.005
Total	23.864	23.991	24.005	24.007	24.029	23.945	23.939

(< 0.05 wt% = below detection limit)

Table 7 (Cont.)

Oxide (wt%)/ Samples	S3 Orange				
	S3-04	S3-11	S3-18	S3-23	S3-27
SiO₂	0.02	0.00	0.00	0.00	0.00
TiO₂	0.02	0.00	0.06	0.00	0.01
Al₂O₃	70.03	70.43	70.90	70.61	70.41
V₂O₃	0.75	0.63	0.61	0.72	0.77
Cr₂O₃	0.06	0.08	0.08	0.02	0.06
Ga₂O₃	0.00	0.00	0.63	0.95	2.28
FeO	0.06	0.07	0.05	0.16	0.11
MnO	0.00	0.00	0.00	0.00	0.00
MgO	28.54	28.74	28.39	26.75	27.22
CoO	0.00	0.00	0.02	0.00	0.00
ZnO	0.12	0.19	0.07	0.13	0.07
CaO	0.01	0.00	0.00	0.00	0.01
Total	99.61	100.14	100.79	99.36	100.94
Based on 32 oxygens					
Si	0.003	0.000	0.000	0.000	0.000
Ti	0.002	0.000	0.008	0.000	0.002
Al	15.764	15.772	15.795	15.970	15.767
V	0.115	0.096	0.092	0.110	0.117
Cr	0.009	0.012	0.012	0.003	0.009
Ga	0.000	0.000	0.076	0.117	0.278
Fe	0.010	0.010	0.007	0.026	0.017
Mn	0.000	0.000	0.000	0.000	0.000
Mg	8.128	8.143	8.000	7.654	7.712
Co	0.000	0.000	0.003	0.000	0.000
Zn	0.016	0.026	0.009	0.019	0.010
Ca	0.002	0.000	0.000	0.000	0.002
Total	24.051	24.060	24.004	23.900	23.913

(< 0.05 wt% = below detection limit)

Table 7 (Cont.)

Oxide (wt%)/ Samples	S4 Red-Purple				S5 Purple			
	S4-02	S4-03	S4-06	S4-14	S5-04	S5-09	S5-13	S5-22
SiO₂	0.00	0.00	0.00	0.00	0.00	0.04	0.01	0.00
TiO₂	0.00	0.00	0.00	0.00	0.11	0.07	0.00	0.01
Al₂O₃	70.18	70.93	70.36	70.52	69.60	70.58	70.71	70.57
V₂O₃	0.20	0.19	0.37	0.48	0.07	0.08	0.04	0.12
Cr₂O₃	0.04	0.10	0.09	0.09	0.02	0.07	0.12	0.06
Ga₂O₃	0.51	0.00	0.00	0.38	1.47	0.79	0.00	2.57
FeO	1.00	1.13	1.30	0.25	0.50	1.00	1.15	0.74
MnO	0.00	0.00	0.02	0.00	0.02	0.00	0.00	0.01
MgO	27.90	27.40	27.10	27.02	27.35	26.34	27.33	26.50
CoO	0.00	0.00	0.00	0.00	0.00	0.00	0.00	0.00
ZnO	0.01	0.05	0.05	0.19	0.72	0.31	0.05	0.13
CaO	0.01	0.00	0.00	0.01	0.01	0.00	0.02	0.00
Total	99.84	99.79	99.30	98.94	99.86	99.29	99.42	100.70
Based on 32 oxygens								
Si	0.000	0.000	0.000	0.000	0.000	0.007	0.002	0.000
Ti	0.000	0.000	0.000	0.000	0.015	0.011	0.000	0.002
Al	15.822	15.964	15.939	15.987	15.767	16.012	15.971	15.872
V	0.031	0.029	0.057	0.074	0.010	0.013	0.007	0.019
Cr	0.006	0.014	0.013	0.013	0.003	0.011	0.017	0.009
Ga	0.063	0.000	0.000	0.047	0.181	0.097	0.000	0.314
Fe	0.159	0.181	0.209	0.040	0.081	0.161	0.184	0.117
Mn	0.000	0.000	0.004	0.000	0.004	0.000	0.000	0.002
Mg	7.956	7.801	7.767	7.749	7.839	7.558	7.809	7.540
Co	0.000	0.000	0.000	0.000	0.000	0.000	0.000	0.000
Zn	0.001	0.006	0.008	0.027	0.102	0.044	0.007	0.018
Ca	0.001	0.000	0.000	0.002	0.001	0.000	0.003	0.000
Total	24.039	23.996	23.996	23.940	24.004	23.915	24.001	23.891

(< 0.05 wt% = below detection limit)

Table 7 (Cont.)

Oxide (wt%)/	S6 Blue	S7 Green
Samples	S6-04	S7-08
SiO ₂	0.00	0.00
TiO ₂	0.01	0.00
Al ₂ O ₃	69.93	70.74
V ₂ O ₃	0.05	0.01
Cr ₂ O ₃	0.02	0.00
Ga ₂ O ₃	0.05	0.00
FeO	2.66	1.14
MnO	0.02	0.19
MgO	25.92	26.96
CoO	0.00	0.00
ZnO	0.59	0.13
CaO	0.01	0.00
Total	99.27	99.17
Based on 32 oxygens		
Si	0.000	0.000
Ti	0.002	0.000
Al	15.972	16.025
V	0.008	0.002
Cr	0.004	0.000
Ga	0.006	0.000
Fe	0.432	0.183
Mn	0.003	0.030
Mg	7.490	7.727
Co	0.000	0.000
Zn	0.085	0.019
Ca	0.003	0.000
Total	24.004	23.986

(< 0.05 wt% = below detection limit)

4.1.3 Heat treatment

At atmospheric condition with a maximum temperature of 1,200°C, orange spinels are visibly impacted by the heating. After heat treatment, the yellow saturation of the orange spinel is dramatically reduced. In general, red spinels appear to be darker (lesser in saturation and lightness), magenta and red-purple spinels exhibit minor shift toward red and/or purple. Purple spinels have lower purple saturation with higher yellow affinity. Blue spinels exhibit clearly shift toward grey (decreased brightness) whereas green spinel displays indiscernible change. Representative spinel samples and their color alterations are presented in Figure 8.



Samples	Color		
	Natural	Heated	Group
S1-01	 5R 4/14	 5R 4/14	Red
S2-20	 7.5RP 5/8	 7.5RP 5/6	Magenta
S3-04	 10R 5/16	 10R 5/12	Orange
S4-03	 2.5R 6/4	 7.5R 5/6	Red-Purple
S5-04	 10P 5/6	 2.5RP 5/4	Purple
S6-04	 10PB 3/2	 10PB 2/2	Blue
S7-08	 2.5GY 6/4	 2.5GY 6/4	Green

Figure 8 Representative spinel samples of each color group presenting appearances before and after heating as reported in the main text.

4.1.4 UV-VIS-NIR spectroscopy

Absorption UV-VIS-NIR spectra of natural and heated spinels are representatively shown in Figure 9. Natural red, magenta, and orange spinels (Figures 9a, 9b, and 9c, respectively) reveal similarly two distinct absorption bands. Natural red spinels show absorption peaked at 396 nm and 537 nm which the later peak is significantly shifted to 546 nm after heating. Natural magenta spinels show absorption bands peaked at 387 nm and 540 nm; after heating, they turn to have higher intensity with significant shift of 540 nm absorption to 546 nm. Natural orange spinels show absorption peaks at 390 nm and 534 nm which obviously present the significant intensity decrease at 390 nm with very slightly shift and 534 nm absorption peaked to 546 nm without significant change in intensity. Natural red-purple spinel (Figure 9d) presents mostly comparable characteristics of two main absorptions of natural magenta spinels at 390 nm and 537 nm which clearly show intensity increase after heating. Natural purple spinel (Figure 9e) mainly yields absorptions at 390 and 543 nm with minor absorption at 487 nm whereas heated purple spinel turns slightly to greater absorption intensity covering the range of 390-543 nm. Blue spinels (Figure 9f) exhibit strong absorptions at 372 and 387 nm with a minor absorption around 459 nm as well as absorption bands centered around 558 and 630 nm; after heating, significantly higher absorption intensities of 372 and 387 nm as well as 459 nm are observed. Green spinel yields only little absorption around 456 nm which is likely unchanged after heating experiment (Figure 9g).

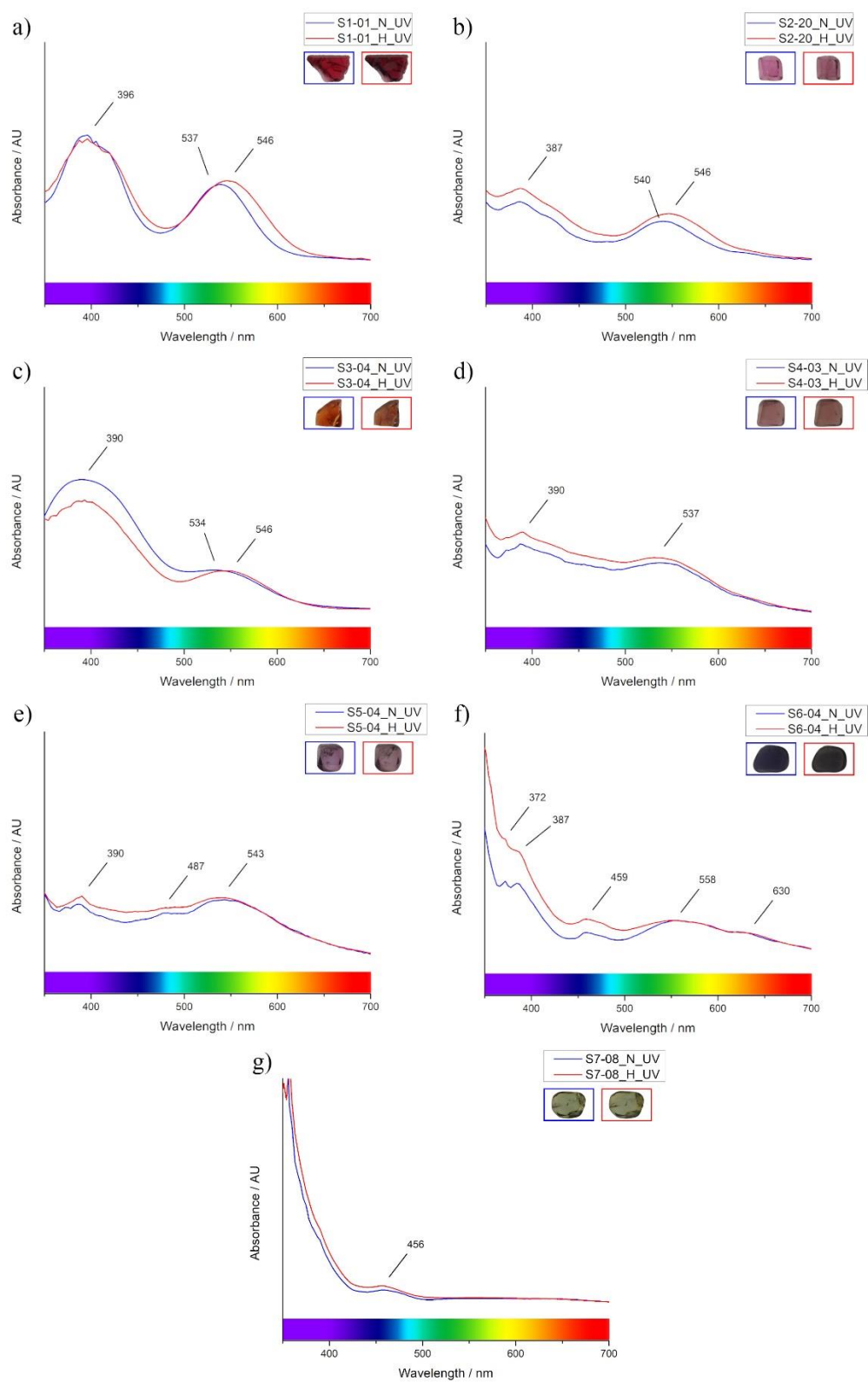


Figure 9 Representative of UV-visible absorption spectra of all spinel varieties and their pattern change after heating experiment under this study.

4.1.5 Raman spectroscopy

Raman spectra (Figure 10) of all spinel samples reveal similar patterns of 4 peak positions at around 306.5-311.4 cm^{-1} , 406.2 cm^{-1} , 665.8-672.0 cm^{-1} , and 762.8-768.9 cm^{-1} . Moreover, natural green spinel presents a small additional peak position at around 719.8 cm^{-1} .

After heating, all spinel varieties still show the same peak positions, however, their intensities seem slightly decreased and broadened, especially the main 406.2 cm^{-1} peak. This peak is expanded its width in most cases (Figure 10a) except for green spinel (Figure 10b). Consequently, the full width at half maximum (FWHM) of the 406.2 cm^{-1} peak is widened with averages of 11.10 cm^{-1} in purple spinels up to 17.01 cm^{-1} in red spinels after heating. Magenta, orange, red-purple, and blue spinels also reveal extension of FWHM with averages of 13.72 cm^{-1} , 14.62 cm^{-1} , 11.49 cm^{-1} , and 12.51 cm^{-1} , respectively, after heating experiment. On the other hand, green spinel (Figure 10b) shows FWHM of the 406.2 cm^{-1} peak shrunken around 1.69 cm^{-1} after heating. In addition, a tiny peak appears between 712.1-726.0 cm^{-1} , such as 715.2 cm^{-1} in red spinel (Figure 10a), which may be an evident of heating in most spinel varieties except for green spinel which such peak (719.8 cm^{-1} in Figure 10b) appears before and after (716.8 cm^{-1}) heating.

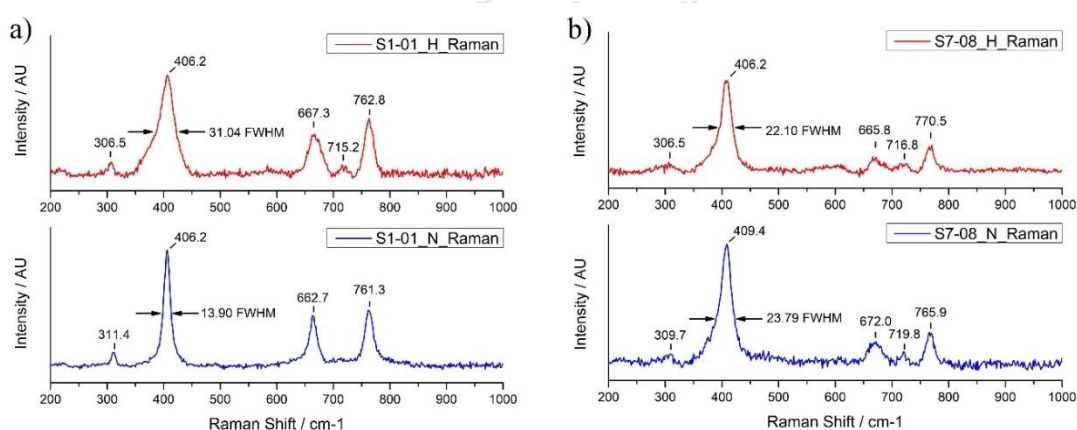


Figure 10 Representative Raman spectra of a) red spinel as a common pattern of most sample groups and b) green spinel presenting dissimilarly pattern to the other groups both before (blue lines, lower spectra) and after (red lines, upper spectra) heating experiment.

4.1.6 Photoluminescence spectroscopy

The photoluminescence (PL) spectra capture the narrow peaks of trace Cr^{3+} around 685.1 to 685.2 nm in most natural spinel samples (red, magenta, orange, red-purple, purple, and blue), however, green spinel rather shows a broader peak at 686.9 nm (Figure 11b, blue line). Other peaks centered about 675, 697, 706, 717, and 722 nm present in all spinel varieties.

Heating effects a broader FWHM and a little shift from 685.1 to 686.9 nm of the main peaks in most spinels, as an example of orange spinel sample (S3-04) shown in Figure 11a. Other small peaks located at about 675, 697, 706, 717, and 722 nm are less structured and unsharp after heating (Figure 11a, red line). The exceptional case is recognized in green spinel which both patterns of natural and heated stone exhibit comparable characteristics of broader FWHM of the 686.9 nm dominant peak and unsharp structure of the other additional peaks (Figure 11b).

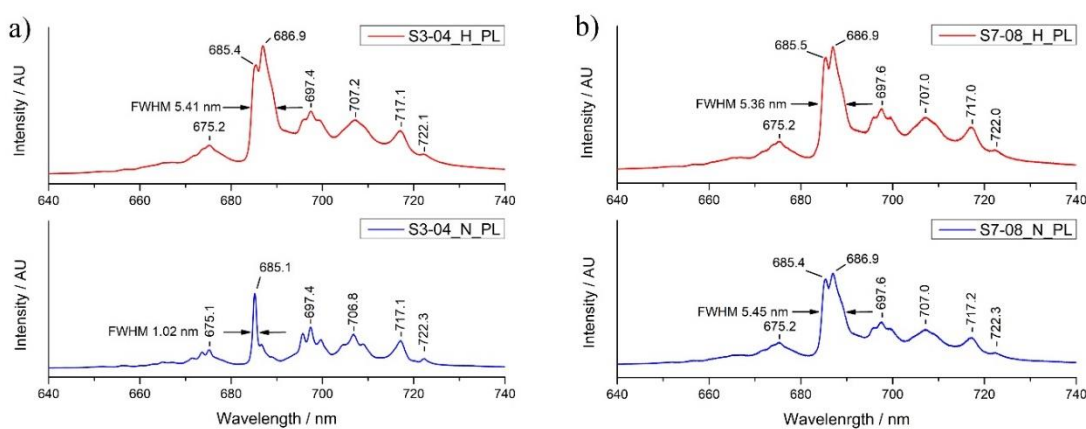


Figure 11 Representative PL spectra of a) orange spinel as a representative pattern of most samples, and b) green spinel with dissimilar pattern to the other spinels both before (blue lines, lower spectra) and after heating experiment (red lines, upper spectra).

4.1.7 X-ray absorption spectroscopy

XANES spectra are obtained from all 22 spinels of 7 varieties, as well as standard materials such as Fe-foil, Cr-foil, V-foil, Fe(II), Fe(III), Cr(III), Cr(VI), V(III), and V(IV) model compounds. The properties of pre-edge absorption are

important to assess the oxidation state and coordination number. Using the XAS Viewer application (Newville, 2013), the centroid position and integrated intensity of pre-edge XANES spectra are determined to stimulate different valency model compounds and their pre-edge peak compositions. Figure 12 depicts the result of Fe pre-edge composition by the XAS Viewer program. In addition, the fluctuation in oxidation state and its symmetry for Fe and V are displayed as shown in Figures 13a and 13b, respectively.

K-edge XANES spectra of Fe, Cr, and V of spinels are analyzed in order to correlate the characteristics of the pre-edge feature with the oxidation state and coordination number of the investigated atoms by comparing them to various model compounds (Bunnag et al., 2020; Wilke et al., 2001). The pre-edge feature is related to the metal electronic transitions $1s \rightarrow 3d$ (quadrupolar) and/or $1s \rightarrow 4p$ (dipolar) (Westre et al., 1997), and its position shifts toward higher oxidation state (Bare, 2007; Newville, 2014; Ravel, 2015; Ruiz, 2011; Westre et al., 1997; Wilke et al., 2001; Wilke et al., 2005).

Numerous previous researchers examined the V XANES spectra of oxides and other crystalline compounds and showed the presence of a pre-edge peak which intensity and energy related to the valency (Balan et al., 2006; Bordage et al., 2011; Burger et al., 2015; Chaurand et al., 2007; Giuli et al., 2004; Liu et al., 2001; Rees et al., 2016; Sutton et al., 2005; Waychunas et al., 1983; Wong et al., 1984). Because the pre-edge intensity is primarily determined by the dipole selection rule, increasing intensity is a result of increased transition dipole moments (Rees et al., 2016). This may be explained based on greater mixing of V p-orbital character into the 3d acceptor orbitals, and these data provide two critical mechanisms for regulating the p-d mixing. Since the V ions occupy octahedral vacancies in the lattice, the V-O bonds compress as a result of an enhanced Coulombic attraction when the V ions are oxidized. Because of the shorter bonds, p-d mixing is more effective, and resulting in a greater pre-edge intensity and a higher oxidation state as suggested by previous researchers (Bordage et al., 2011; Rees et al., 2016; Wong et al., 1984). For this reason, it is hypothesized that V^{3+} is localized in highly symmetrical octahedral sites

in spinel, based on the low intensity of the pre-edge characteristic (Burger et al., 2015).

The most basic approach for determining V valency is plotting pre-edge absolute energy (eV). Several valences superimpose the absorption edge, allowing oxidation state determination problematic (Chaurand et al., 2007). In fact, prior researchers developed more advanced methods for determining oxidation state and symmetry of V. Farges et al. (1996) established the pre-edge modeling fitting by Lorentzian function, which has also been utilized to estimate titanium symmetry and valency. Giuli et al. (2004) then established the contribution of various V states on pre-edge integrated intensity and centroid position. Subsequently, Chaurand et al. (2007) devised a pre-edge modelling fitting using pseudo-Voigt to determine mixed oxides and site symmetry which was applied to this research.

Peterson et al. (1996; 1997) measured the $\text{Cr}^{3+}:\text{Cr}^{6+}$ ratio in complex oxide samples using several methods and suggested that either peak height or peak area may be used to compute the Cr^{6+} /total Cr content. Huggins et al. (1999) reached similar model-fitting findings on Cr pre-edge information, valency, and symmetry (Pseudo-Voigt fitting). Although several methodologies have been introduced by many researchers that pre-edge features relate to dipolar and quadrupolar transitions from the metal 1s core state to metal 3d with some contribution from 4p depending on the local symmetry, their intensity and energy are likely dependent to the metal cation valency and site symmetry (Dubrail & Farges, 2009; Eeckhout et al., 2007; Fandeur et al., 2009; Farges, 2009; Huggins et al., 1999; Juhin et al., 2008; Juhin et al., 2007; Odake et al., 2008; Villain et al., 2007; Wongkokua et al., 2009). Cr oxidation and site symmetry could simply be determined by Peterson's initial method since the characteristics of Cr^{3+} and Cr^{6+} are distinct. Examining the pre-edge height (1s \rightarrow 3d electronic transition) and position (eV) in Cr pre-edge XANES spectra is likely the simplest method (Eeckhout et al., 2007; Peterson et al., 1996; Peterson et al., 1997).

Cr pre-edge XANES spectra of spinel samples in this research reveal a small absorption peak at approximately 5991.0 eV and likely without second peak, which is consistent with Eeckhout et al. (2007) that only significant feature appears around 5990.6 eV as for a chromite (Cr^{3+}) sample. Cr^{3+} has octahedral symmetry,

centrosymmetric geometry, no p-d mixing allowed, and a d^3 electronic configuration, whereas Cr^{6+} has tetrahedral symmetry, non-centrosymmetric geometry, p-d mixing allowed, and a d^0 electronic configuration, which correspond with the pre-edge XANES position around 5993.5 eV. It is assigned to a bound state $1s \rightarrow 3d$ transition (Eeckhout et al., 2007; Peterson et al., 1996; Peterson et al., 1997). The remarkable intensity of this Cr^{6+} pre-edge peak is attributed to oxygen 4p mixing into metal 3d orbitals, providing the transition $1s \rightarrow 4p$ character. Moreover, since this electric dipolar coupled mechanism is significantly stronger than the electric quadrupolar coupled mechanism, even a tiny quantity of 4p mixing into the 3d orbitals may have a large impact on the pre-edge peak intensity (Westre et al., 1997). It should be noted that the Cr pre-edge XANES intensity and absolute position of Cr^{3+} and Cr^{6+} XANES spectra are considerably different (~ 3 eV) and are not overlaid with one another; additionally, several prior studies have also reported Cr^{3+} [6] in spinels (Dubrail & Farges, 2009; Farges, 2009; Juhin et al., 2008; Juhin et al., 2007).

Thus, according to our XAS results, natural (unheated) spinels indicate that the Fe^{2+} occupied the tetrahedral site ($^T\text{Fe}^{2+}$) of Mg in all colored spinels and increased in valency while occupying the octahedral site ($^M\text{Fe}^{3+}$) upon heating in the majority of spinels (see Figure 13a). Vanadium is present as V^{3+} in Al-octahedral site ($^M\text{V}^{3+}$) in all spinels and increased its oxidation state to $^M\text{V}^{4+}$ in accordance with (Balan et al., 2006; Bordage et al., 2011; Chaurand et al., 2007; Rees et al., 2016; Wong et al., 1984) (Figure 13b). Chromium is presented as Cr^{3+} in Al-octahedral ($^M\text{Cr}^{3+}$) site in all spinels and no substantial change in the pre-edge is seen upon heating, indicating that no valency change (Figure 13c). Cr pre-edge XANES spectra of all colored spinel groups show an extremely low intensity (<0.2 a.u. in accordance with Peterson et al. (1996; 1997)) located at around 5991.0 eV where standard Cr^{6+} compound demonstrates exceptionally high intensity at around 5993.5 eV. In summary, the Fe oxidation state of natural spinel is shown as Fe^{2+} and mostly increased their valency upon heating (Figure 13a), except for green spinel which likely present little to no change. The V oxidation state of natural spinel is V^{3+} in all spinel groups, but they dramatically increase to a greater valency after heating in majority of samples (Figure 13b). However, Cr appears to be unchanged in most

spinel groups after heating which it identically present as Cr^{3+} , as revealed in Figure 13c.

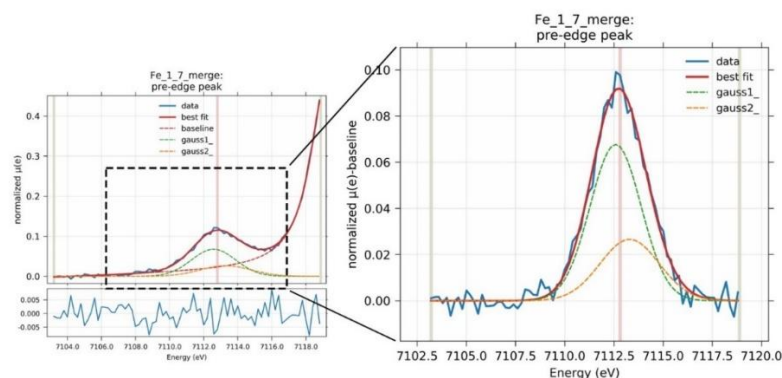


Figure 12 Representative of Fe pre-edge XANES spectra composition.

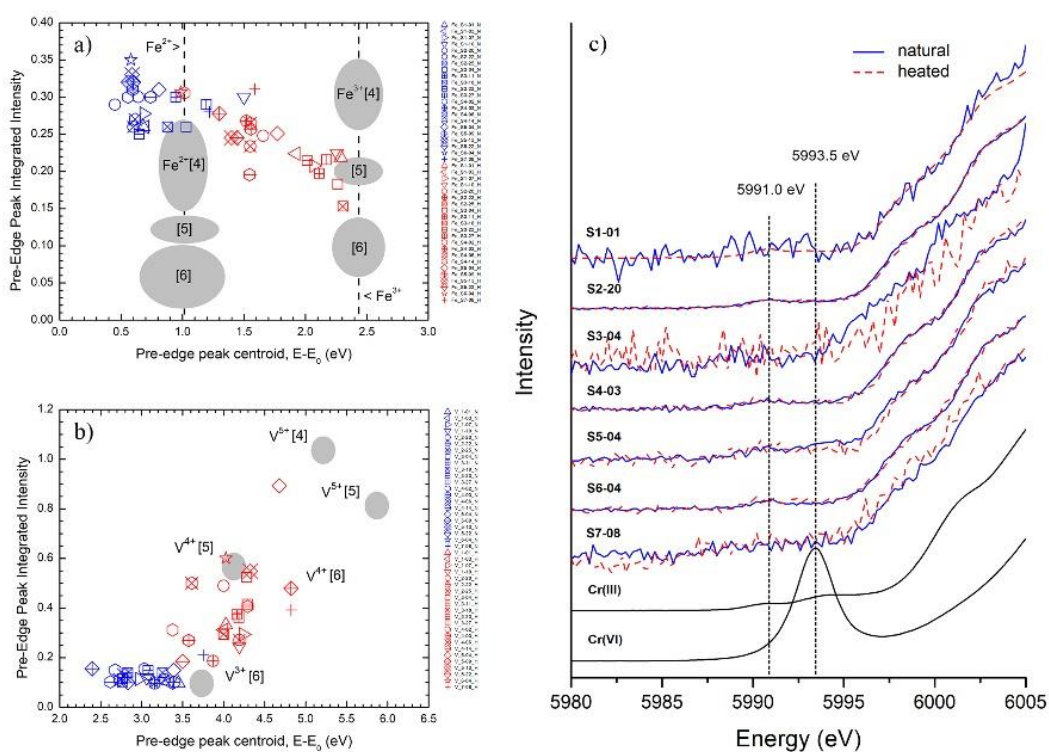


Figure 13 Diagram represented integrated pre-edge intensity and pre-edge peak centroid ($E-E_0$) parameter of all spinel samples in various a) Fe- and b) V-oxidation state and their coordination, whereas c) represented normalized Cr pre-edge XANES spectra of natural (blue lines) and heated (red lines) spinels compared with Cr(III) and Cr(VI) standards. Number [4], [5], and [6] represent a 4-fold, 5-fold, and 6-fold coordinated atoms, respectively.

4.2 Discussion

4.2.1 Color-causing elements

As reported in the mineral chemistry, Fe, Cr, and V appear to be the major chromophores of spinel varieties. Their elemental ratios are displayed in a ternary diagram (Figure 14), which graphically demonstrates that red and orange spinels are more closely associated with Cr and V contents, respectively, while the others (magenta, red-purple, purple, blue, and green) are more generally associated with a greater Fe component. Although cobalt was suggested by numerous previous researchers to contribute to the blue coloration of spinels (Carbonin et al., 1996; Chauviré et al., 2015; D'Ippolito et al., 2012; D'Ippolito et al., 2015; Gorghinian et al., 2013; Krzemnicki, 2011; Peretti & Günther, 2003; Shigley & Stockton, 1984), it is not presented in all spinel samples. As a result, Fe is more dominant and is more likely to be associated with the purple, blue, and green colors. V is likely responsible for orange-colored spinels due to its highest ratio compared to Fe and Cr. However, V and Cr almost certainly involve in the red color, with equally high contents of both elements tend to cause red. On the other hand, lower Cr may appear orangy red. Our finding agrees well with observation of Andreozzi et al. (2018) which suggested that high V content induces orange but high Cr content influences red in spinels. Therefore, two groups of spinels, including Cr-V related color spinels (red and orange) and Fe-related color spinels (magenta), red-purple, purple, blue, and green) will be discussed further.

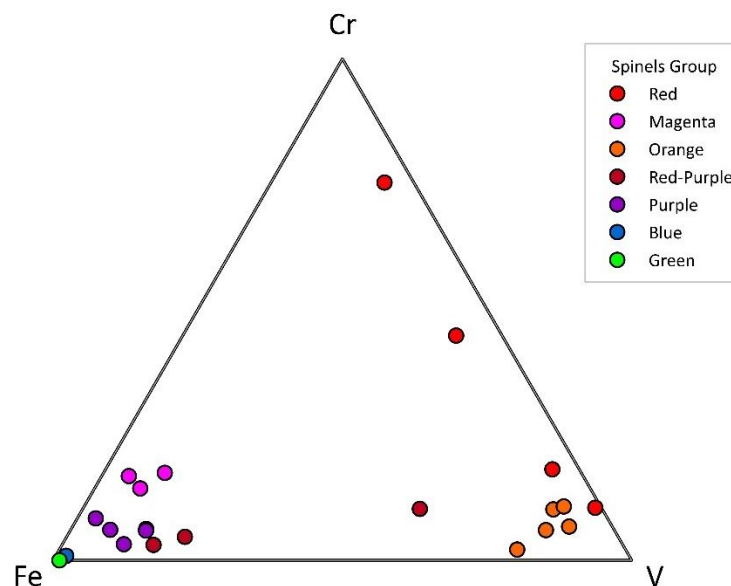


Figure 14 Ternary plots of Fe-Cr-V of spinel samples showing atomic ratios involving color.

Noteworthy correlations between certain absorption peaks in UV-Visible spectra and the color of spinels are summarized in Table 8. There are several absorption positions, commonly including 372, 390, 459, 487, 537, 558, and 630 nm, but not all features present in the sample group. For example, absorption centered around 372 nm is observed particularly in red-purple, purple, blue, and green whereas 390 nm absorption obtains from all colored spinel groups. Absorption band centered around 537 nm can be observed in red, magenta, orange, red-purple, and purple. On the other hand, absorption bands ranging from 558 to 630 nm seem specifically in blue spinel

Table 8 Summary of UV-visible absorption approximate in each colored spinel groups.

Absorption (nm) / Color	Cause	Red (S1)	Magenta (S2)	Orange (S3)	Red- purple (S4)	Purple (S5)	Blue (S6)	Green (S7)
372	Fe ²⁺ and Fe ^{3+*}	x	x	x	☑	☑	☑	☑
387-396	Fe ²⁺ , Cr ³⁺ , V ^{3+*}	☑	☑	☑	☑	☑	☑	☑
456-459	Fe ²⁺ and/or Fe ³⁺	x	x	x	x	x	☑	☑
487	Fe ²⁺	x	x	x	x	☑	x	x
534-546	Fe ²⁺ , Cr ³⁺ , V ^{3+*}	☑	☑	☑	☑	☑	x	x
558	Fe ²⁺	x	x	x	x	x	☑	x
630	Co ²⁺	x	x	x	x	x	☑	x

*Comprehensive absorption band

Red and orange (Cr-V-related) spinels exhibit two distinct sorts of strong absorption. The primary absorption bands at 387-396 and 534-546 nm (corresponding to violet-blue and green-yellow, respectively, in visible spectrum) originate from superimposition of the absorption spectra of V³⁺ and Cr³⁺ in an octahedral site (Andreozzi et al., 2018). The absorption bands centered on 387-396 nm and 534-546 nm are attributed to spin-allowed electronic d-d transitions $^4A_{2g} \rightarrow ^4T_{1g}(F)$ and $^4A_{2g} \rightarrow ^4T_{2g}(F)$ in $^M\text{Cr}^{3+}$ for red spinel but induced by spin-allowed d-d transitions $^3T_1(F) \rightarrow ^3T_1(P)$ and $^3T_1(F) \rightarrow ^3T_2(F)$ in $^M\text{V}^{3+}$ for orange spinels, respectively (Andreozzi et al., 2018).

Additionally, magenta (Fe-related) spinels exhibit two distinct absorption bands at 387 nm (violet-blue range) and 540 nm (green-yellow regions). These

characteristics are comparable to those of red spinel. There are relatively a few discrepancies in the absorption spectra of orange, red, and magenta. Orange and red samples have nearly identical absorption bands, but the orange samples are V^{3+} dominant (Andreozzi et al., 2018), and the absorption bands are slightly different in position and width. This results in a blue-shift of the absorption, or a greater absorption of the violet-blue and green regions, leading to more efficient light transmission in the yellow-orange-red region. In contrast, red/magenta Cr-dominant spinels have a substantially greater band intensity, which means that light in the violet-blue and yellow-green visible areas is severely absorbed, whereas light in the red part of the spectrum is more effectively transmitted. Magenta samples have a remarkably similar absorption spectrum to red samples, with both being absorbed by bands associated with Cr^{3+} and minor Fe cations. The variations in the absorption spectra of magenta and red samples are entirely attributable to the chromophore cation concentrations, with red samples containing more Cr^{3+} and having more prominent absorption bands, which results in a greater saturation of the red hue. In comparison to red samples, magenta spinels are deficient in Cr^{3+} and comparatively rich in Fe, resulting in less intense absorption bands and a relatively intense low-energy tail of the UV absorption band owing to ligand-to-metal charge transfer (LMCT) $O^{2-} \rightarrow Fe^{2+}$ (Andreozzi et al., 2018). Light absorption is weaker in the visible spectrum than it is in the red samples, hence two transmission windows exist for the blue and red visible region.

Despite their disparate appearances, the remaining Fe-related spinels, including red-purple, purple, blue, and green, have comparable absorption spectra. UV-edge to violet absorption with a particularly high intensity is induced by $O^{2-} \rightarrow Fe^{2+}$ and $O^{2-} \rightarrow Fe^{3+}$ charge transfer transitions which result in considerable absorption in violet-blue region. The absorption mostly around UV (including 372 and 387 nm) is attributed ${}^7Fe^{2+}$ (Muhlmeister et al., 1993) spin-forbidden transitions ${}^5E(D) \rightarrow {}^3E(D)$, and ${}^5E(D) \rightarrow {}^3T_2(G)$, respectively, and might be amplified by ${}^7Fe^{2+}$ - ${}^MFe^{3+}$ ECP transitions (Atsawatanapirom et al., 2016). Another absorption band around 456 and 487 nm that presented in purple, blue, and green spinels are assigned to spin-forbidden transitions ${}^5E(D) \rightarrow {}^3E(G)$, ${}^3T_2(F)$, ${}^3T_1(F)$ of ${}^7Fe^{2+}$ (Andreozzi et al.,

2001; Fregola et al., 2014; Muhlmeister et al., 1993; Schmetzer et al., 1989; Taran et al., 2005) whereas the other researchers ascribed to spin-forbidden ${}^6A_{1g} \rightarrow {}^4A_{1g}, {}^4E_g$ transitions of isolated ${}^MFe^{3+}$ ions (Taran et al., 2005), and to ECP interactions ${}^6A_{1g} \rightarrow {}^4A_{1g}, {}^4E_g$ in ${}^TFe^{3+}-{}^MFe^{3+}$ clusters (Andreozzi et al., 2001).

Blue spinels exhibit a variety of absorption bands around 372 nm and 387 nm (violet region), 459 nm (blue region), and 558-630 nm (green-yellow-orange region). Absorption band at approximately around 459-460 nm was also suggested by Andreozzi et al. (2018), and in agreement with Andreozzi et al. (2001) and Taran et al. (2005), that it probably relates with ${}^MFe^{3+}$ which contradicts earlier suggestions (Andreozzi et al., 2001; Fregola et al., 2014; Muhlmeister et al., 1993; Schmetzer et al., 1989; Taran et al., 2005). However, Taran et al. (2005) proposed both Fe^{2+} and Fe^{3+} . Although the band between 487 and 580 nm is inconsistent, it has been attributed to spin-forbidden transitions of ${}^TFe^{2+}$ (Andreozzi et al., 2018; Fregola et al., 2014; Gaffney, 1973; Taran et al., 2005). Absorption at 558 nm is attributed to spin forbidden transition ${}^5E(D) \rightarrow {}^3T_2(H)$ of ${}^TFe^{2+}$ (Fregola et al., 2014; Muhlmeister et al., 1993; Schmetzer et al., 1989; Taran et al., 2005). Additionally, absorption around 588 nm may be owing to spin-forbidden transitions ${}^5E(D) \rightarrow {}^3E(H)$ of isolated ${}^TFe^{2+}$ ions (Schmetzer et al., 1989; Taran et al., 2005). Lastly, $Fe^{2+} - Fe^{3+}$ IVCT and/or $Fe^{2+} - Fe^{3+}$ ECP interactions should be responsible for absorption around 666 nm (Hålenius et al., 2002; Schmetzer et al., 1989). 545-625 nm broad band absorption is seen solely in blue-colored spinels, which was suggested as cobalt-related absorption (Atsawatanapirom et al., 2016; Fregola et al., 2014; Palke & Sun, 2018; Peretti et al., 2015; Saeseaw, 2015), despite the fact that our blue spinel sample demonstrated no evidence of cobalt. Green spinel exhibits strong UV-edge absorption in the violet and blue regions of the visible spectrum, which may play a role of $O^{2-} \rightarrow Fe^{2+}$ and $O^{2-} \rightarrow Fe^{3+}$ charge transfer transitions (Andreozzi et al., 2018; Fregola et al., 2014; Taran et al., 2005) as well as ${}^MFe^{3+}$ absorption at 456 nm, which increased very slightly upon heating (Andreozzi et al., 2001; Andreozzi et al., 2018; Fregola et al., 2014; Muhlmeister et al., 1993; Schmetzer et al., 1989; Taran et al., 2005).

After heating, significant to minor color alteration can be observed in the red, magenta, orange, red-purple, purple, and blue, on the other hand, green appears to be

unchanged. The Fe-related color spinels, including magenta, red-purple, purple, and blue mostly show higher absorption around the violet-blue region (372, 387-390, 457-459, 487 nm) with a relatively minor change in the green-yellow region (band centered around 534-558 nm). In contrast, orange spinel shows a significant decrease in the violet-blue region (390 nm) with little to no change in the green region, whereas red spinel shows a significant change of wider absorption covering the green toward the yellow region (534-546 nm). For Fe-related color spinels, it is worth noting that the greater oxidation state reported in XAS investigation correlates with the higher Fe-related absorptions of the violet-blue region (372, 387-390, 457-459, 487 nm) (Andreozzi et al., 2001; Fregola et al., 2014; Muhlmeister et al., 1993; Schmetzer et al., 1989; Taran et al., 2005). This might be a remark of the higher oxidation state of $\text{Fe}^{2+} \rightarrow \text{Fe}^{3+}$ in heated spinels (Andreozzi et al., 2018; Fregola et al., 2014; Gaffney, 1973; Taran et al., 2005). For V-dominant orange spinels, the V^{3+} -related absorption band centered around 390 nm (Andreozzi et al., 2018) is obviously decreased after heating, which corresponds to a higher oxidation state of $\text{V}^{3+} \rightarrow \text{V}^{4+}$ as determined by XAS. For red spinels, the Cr^{3+} -related absorption band centered about 387-396 nm overlain by V^{3+} (Andreozzi et al., 2018) shows mostly identical after heating. This is consistent with a stable oxidation state of Cr^{3+} in heated red spinels. However, the origin of the band system around 487-580 nm is not entirely obvious, but as mentioned above, some of them are probably triggered by spin-forbidden transition of ${}^7\text{Fe}^{2+}$ (Andreozzi et al., 2018; Fregola et al., 2014; Gaffney, 1973; Taran et al., 2005). Therefore, the increasing of most visible absorptions is likely attributable to an increasing of Fe oxidation state from $\text{Fe}^{2+} \rightarrow \text{Fe}^{3+}$ of heated spinels. Cr^{3+} -related absorption band around 393 nm in red spinel remains stable owing to identical Cr valency while a decreasing of V^{3+} -related absorption band centered around 390 nm is likely due to the higher oxidation state of $\text{V}^{3+} \rightarrow \text{V}^{4+}$ after heating in orange spinels. These agree with XAS interpretation as reported earlier (Figure 13).

4.2.2 Indication of heated spinel

Raman and Photoluminescence spectra of heated spinels demonstrate remarkable changes in their characteristic features. Four Raman peaks are recognized in a red spinel sample at around $306.5\text{-}311.4\text{ cm}^{-1}$, 406.2 cm^{-1} , $662.7\text{-}672.0\text{ cm}^{-1}$, and

761.3-768.9 cm^{-1} comparable to previous studies (Bootkul et al., 2016; Cynn et al., 1992; Slotznick & Shim, 2008), they assigned these peaks to $T_{2g}(1)$, E_g , $T_{2g}(2)$, and A_{1g} mode, respectively (Figure 10a). The full width at half maximum (FWHM) dominating at around 406 cm^{-1} peak was suggested to be appropriate for determining natural and heated spinels since disordering of the spinel structure lattice is the expected consequence after heating above 750°C (Chauviré et al., 2015; Myat Phyo et al., 2019; Peretti et al., 2015; Saeseaw et al., 2009; Widmer et al., 2015). After heating, the dominating Raman spectra around 406.2 cm^{-1} of representative red spinel exhibit an enlargement of full width at half maximum (FWHM) with decreasing in intensity. These evidences indicate that the crystal lattice has become disordered (also referred as partly inverse spinel) as a result of heating process (Widmer et al., 2015). Moreover, an additional small peak at around 715.2 cm^{-1} between 712.1-726.0 cm^{-1} (Figure 10a) is observed in most color spinel groups after heating. Except green spinel, it exhibits similar features of 5 peaks in both spectra before and after heating (Figure 10b).

The broadening of the main peak around 406.2 cm^{-1} has been attributed to the asymmetry of the E_g mode, which is related to cation disordering (bending of Al in tetrahedral coordination) (Cynn et al., 1992; Slotznick & Shim, 2008). The lower shift of the peak 311.4 cm^{-1} or $T_{2g}(1)$ to 306.5 cm^{-1} (Figure 10a) may be attributed to the entry of larger Al atoms into the T site. This indicates that the vibrations of the MgO_4 and AlO_4 tetrahedra may still couple strongly. This also can be seen in green spinel as presented in Figure 10b. The higher shift of the 662.7 cm^{-1} peak in Figure 10a or $T_{2g}(2)$ mode to 667.3 cm^{-1} is consistent with the entry of lighter magnesium atoms into the octahedral positions (Slotznick & Shim, 2008). Even though it is difficult to define the additional peak at 715.2 cm^{-1} in heated red spinel or 719.8 cm^{-1} in unheated green spinel (between 712.1-726.0 cm^{-1} , Figures 10a and 10b). They occur after heating. Therefore, they may be related to the symmetric stretching of the AlO_4 tetrahedra due to cation disorder whereas peak at 761.3-770.5 cm^{-1} (A_{1g}) might relate with Mg-O stretching vibration (Cynn et al., 1992; Slotznick & Shim, 2008). These features of disorder cations presented in Raman spectra can also be seen in synthetic spinels since the synthesizing process of growth crystal undergo by high

temperature above 750°C (Chauviré et al., 2015; Fraas et al., 1973; Myat Phyو et al., 2019; Peretti et al., 2015; Saeseaw et al., 2009; Slotznick & Shim, 2008; Widmer et al., 2015).

The photoluminescence spectrum is utilized to observe the narrow peaks of the Cr³⁺ trace element in the spinel structure. Heating of spinel was hypothesized to cause disorder and defects in the crystal lattice (Atsawatanapirom et al., 2016; Peretti et al., 2015; Saeseaw, 2015; Saeseaw et al., 2009; Shen et al., 2004; Widmer et al., 2015). In normal spinels, a strong dominant chromium line with an absorption at 685 nm (R-line) is recognized as well as additional characteristics at 675, 697, 706, 717, and 722 nm (N-lines) (Mikenda, 1981; Phan et al., 2004). However, the most significant change occurs in the intensity of the dominant peak at about 686.9-687.0 nm (N1 line) (Bootkul et al., 2016; Mikenda, 1981; Phan et al., 2004), whereas the other features showed unsharp and unstructured after heating (Figure 11a). Unlike the others, the green sample exhibits no discernible change in the PL spectrum and most likely exhibited comparable characteristics to heated samples in all aspect including a broader 686.9 nm peak as well as unsharp of the other peaks (Figure 11b). The dominant sharp R-line, which is located around 685 nm originating from the states of the Cr³⁺ cation, has an ideal short-range order, due to the spin-forbidden transition ${}^2E_g \rightarrow {}^4A_{2g}$. Furthermore, the peak at 686.9-687 nm (Figure 11) is referred to as the N1-line due to a coupling between the Cr³⁺ state and the lattice defect. Broadening and poorly defined structure after heating is due to the interactive processes between Cr³⁺ ions and site occupation of the environment as well as an increasing of lattice defects (disorder in inverse spinels, as mentioned above) (Bootkul et al., 2016; Mikenda, 1981; Phan et al., 2004). Thus, with increasing of temperature, the higher the inversion to inverse spinels (disorder) occurs.

These Raman and PL characteristics provided a strong indication of whether the spinels are normal or inverse by considering the disorder characteristic features presented as a broadening of the dominant peak around 406.2 cm⁻¹ and additional 715.2-719.8 cm⁻¹ in Raman spectra (between 712.1-726.0 cm⁻¹), as well as a broadening and poorly defined structure of R-line (around 685 nm) and N-lines (others additional peak), especially the N1-line (686.9-687 nm) which they are

significantly dominant after heating. Moreover, these also indirectly indicate the coloration in spinels both before and after heating.

In addition, pre-edge model fitting of Fe K-edge (Figure 12 and 13a) XANES spectra indicate a significant increasing of average oxidation state from $T\text{Fe}^{2+}$ toward $M\text{Fe}^{3+}$, while pre-edge model fitting of V K-edge XANES spectra represents a significant increasing of an average V oxidation state from $M\text{V}^{3+}$ toward $M\text{V}^{4+}$ in the majority of samples. Some samples plotted between tetrahedral site and octahedral site (pentahedral site) indicate the alternating of cations between both sites (inverse spinels), since occupation of a pentahedral site is improbable owing to the absence of such site in spinels. The plotting also indicates a disorder of normal spinels towards inverse spinels after heating experiment which their averaged plots fall around the pentahedral site. Since some cations located in octahedral site may move to tetrahedral site as normal spinels altered to inverse spinels following this formula $A(\text{BB})\text{O}_4 \rightarrow \text{B}(\text{AB})\text{O}_4$. All spinel samples represent the oxidizing of V^{3+} and Fe^{2+} to V^{4+} and Fe^{3+} which occupy both tetrahedral and octahedral sites (from normal spinel to inverse spinel). The results gathered by Raman and PL indeed support the results of XAS that present the change in oxidation as well as site occupancy which are the results of the disorder of inverse spinel after heating.

CHAPTER 5

CONCLUSION AND RECOMMENDATION

5.1 Conclusion

Physical and chemical properties of the studied tanzanites were observed and measured using basic and advanced gemological instruments in combination with X-ray absorption spectroscopy (XAS). These results can be used to demonstrate the coloration in natural and heat-treated tanzanites, which can be recapitulated below.

1) More desired violet-blue color in tanzanite can be improved by thermal process.

2) Absorption band with a peak around 460 nm (blue range) is the main cause of color in different directions (trichroism) of natural tanzanite whereas the absorption band in the yellow region (peak at 585–600 nm) similarly presents in all directions and still remains after heating.

3) After heating, the c-axis shows the most significant change in color compared with the other directions. It clearly relates to the disappearance of the 460 nm absorption band.

4) XAS spectra show an increasing edge energy of vanadium which indicates the higher oxidation state after heat treatment. This should cause the disappearance of the 460 nm absorption band and induce more intensive blue-violet color in heated tanzanites.

For spinels, based on literatures and the finding of this research, their colors are clearly tied to one or more trace elements, depending on which trace elements are prominent.

1) Spinel should be classified, on the basis of color varieties, into two groups, the Cr-V-related group, and the Fe-related group.

2) Spinel with a high MV^{3+} ratio yield orange, but those with higher MCr^{3+} should induce deeper red.

3) Blue interference is caused by the higher Fe^{2+} concentration, whereas Fe^{2+} and Fe^{3+} charge transfer involves green color.

4) Magenta, red-purple, and purple spinels are therefore consequence of proportional combination between Fe and V as well as Cr concentration, accordingly.

5) These color variations in spinel after heating are mostly due to changing of oxidation state of iron and vanadium, whilst chromium stays consistent.

6) Raman and photoluminescence spectra are helpful technique to distinguish between normal (unheated) and inverse (heat-treated) spinels. For examples, small Raman peak at 715.2 cm^{-1} in heated red spinel or 719.8 cm^{-1} in green spinel (between $712.1\text{--}726.0\text{ cm}^{-1}$) are missing in the majority of normal spinels (unheated spinels).

UV-Visible-NIR and X-ray Absorption Spectroscopies are effective for determining the color alteration, as well as valency and site occupancy of the color-causing chromophores, respectively. Additional sophisticated approaches may be used to facilitate the correlation of these data, resulting in a more accurate and comprehensive knowledge of spinel and tanzanite coloration.

5.2 Recommendation

Although this research was meticulously designed and prepared, there is still a limit to the original source of the rough samples. The author would strongly encourage future research to focus on green spinels which must collect directly from mining areas. These natural samples should be characterized before and after heating experiment in order to gain more favorable outcomes. This should provide more convincing results to fill the gap.

Quantitative trace element analyses should be developed for XAS-based study. The higher concentration yields the better quality of XANES spectrum. The pre-edge characteristic is vital for determining valency and coordination number; therefore, further researchs should concentrate on the pre-edge region. Edge energy

absorption of some trace elements may not be efficient to distinguish the different characteristics of gemstones after heating; future study should refer to the methodology in this work to develop a better detection of valency changing and disordering in site occupancy of trace elements in gemstones.



REFERENCES

- Anderson, B. W. (1937). Magnesium-Zinc-Spinels from Ceylon. *Mineralogical Magazine*, 24, 547-554.
- Anderson, B. W. (1968). Three items of interest to gemmologists. *Journal of Gemmology*, 11, 1-6.
- Andreozzi, G., Hålenius, U., & Skogby, H. (2001). Spectroscopic active IVFe³⁺-VIFe³⁺ clusters in spinel-magnesioferrite solid solution crystal: A potential monitor for ordering in oxide spinels. *Physics and Chemistry of Minerals*, 28, 435-444. <https://doi.org/10.1007/s002690100178>
- Andreozzi, G. B., D'Ippolito, V., Skogby, H., Hålenius, U., & Bosi, F. (2018). Color mechanisms in spinel: a multi-analytical investigation of natural crystals with a wide range of coloration. *Physics and Chemistry of Minerals*, 46(4), 343-360. <https://doi.org/10.1007/s00269-018-1007-5>
- Armbruster, T., Bonazzi, P., Akasaka, M., Bermanec, V., Chopin, C., Gieré, R., Heuss-Assbichler, S. L., Axel, , Menchetti, S., Pan, Y., & Pasero, M. (2006). Recommended nomenclature of epidote-group minerals. *European Journal of Mineralogy*, 18(5), 551-567. <https://doi.org/10.1127/0935-1221/2006/0018-0551>
- Atsawatanapirom, N., Bupparenoo, B., Nilhud, N., & Saeneekatima, K., Leelawatanasuk, T. (2016). Identification and Stability of Cobalt Diffusion-Treated Spinel. 5th GIT International Gem and Jewelry Conference: Treatment and Synthetics update and disclosure, Pattaya, Thailand.
- Balan, E., De Villiers, J. P. R., Eeckhout, S. G., Glatzel, P., Toplis, M. J., Fritsch, E., Allard, T., Galoisy, L., & Calas, G. (2006). The oxidation state of vanadium in titanomagnetite from layered basic intrusions. *American Mineralogist*, 91(5-6), 953-956. <https://doi.org/10.2138/am.2006.2192>
- Bare, S. R. (2007). *Introduction to X-ray Absorption Spectroscopy* https://millenia.cars.aps.anl.gov/xafs/Workshops/APS2007?action=AttachFile&do=view&target=Bare_Intro.pdf
- Barot, N. R., & Boehm, E. W. (1992). Gem-Quality Green Zoisite. *Gems & Gemology*, 28(1), 4-15.
- Biagioni, C., & Pasero, M. (2014). The systematics of the spinel-type minerals: An overview. *American Mineralogist*, 99(7), 1254-1264. <https://doi.org/10.2138/am.2014.4816>
- Bocchio, R., Adamo, I., Bordoni, V., Caucia, F., & Diella, V. (2012). Gem-quality zoisite from Merelani (Northeastern Tanzania): Review and new data. *Periodico di Mineralogia*, 81(3), 379-391. <https://doi.org/10.2451/2012PM0022>
- Bootkul, D., Tengchaisri, T., Tippawan, U., & Intarasiri, S. (2016). Analysis and modification of natural red spinel by ion beam techniques for jewelry applications. *Surface and Coatings Technology*, 306, 211-217. <https://doi.org/10.1016/j.surfcoat.2016.05.084>

- Bordage, A. e., Balan, E., Villiers, J. P. d., Cromarty, R., Juhin, A., Carvallo, C., Calas, G., Sunder Raju, P. V., & Glatzel, P. (2011). V oxidation state in Fe Ti oxides by high-energy resolution fluorescence-detected X-ray absorption spectroscopy. *Physics and Chemistry of Minerals*, 38, 449-458.
- Bosi, F., Biagioni, C., & Pasero, M. (2019). Nomenclature and classification of the spinel supergroup. *European Journal of Mineralogy*, 31(1) , 183-192. <https://doi.org/10.1127/ejm/2019/0031-2788>
- Bragg, W. H. (1915). XXX. The structure of the spinel group of crystals. *The London, Edinburgh, and Dublin Philosophical Magazine and Journal of Science*, 30(176), 305-315. <https://doi.org/10.1080/14786440808635400>
- Bunnag, N., Kasri, B., Setwong, W., Sirisurawong, E., Chotsawat, M., Chirawatkul, P., & Saiyasombat, C. (2020). Study of Fe ions in aquamarine and the effect of dichroism as seen using UV-Vis, NIR and x-ray. *Radiation Physics and Chemistry*, 177, 109107. <https://doi.org/10.1016/j.radphyschem.2020.109107>
- Burger, P. V., Papike, J. J., Bell, A. S., & Shearer, C. K. (2015, 1 March 2015). VANADIUM VALENCE IN SPINEL FROM A Y98 COMPOSITION MELT AS DETERMINED BY XRAY ABSORPTION NEAR EDGE STRUCTURE (XANES). 46th Lunar and Planetary Science Conference (2015), The Woodlands, TX.
- Carbonin, S., Russo, U., & Giusta, A. D. (1996). Cation Distribution in Some Natural Spinels from X-ray Diffraction and Mössbauer Spectroscopy. *Mineralogical Magazine*, 60, 355 - 368.
- Chaurand, P., Rose, J., Briois, V., Salome, M., Proux, O., Nassif, V., Olivi, L., Susini, J., Hazemann, J.-L., & Bottero, J.-Y. (2007). New Methodological Approach for the Vanadium K-Edge X-ray Absorption Near-Edge Structure Interpretation: Application to the Speciation of Vanadium in Oxide Phases from Steel Slag. *The Journal of Physical Chemistry B*, 111(19) , 5101-5110. <https://doi.org/10.1021/jp063186i>
- Chauviré, B., Rondeau, B., Fritsch, E., Ressigeac, P., & Devidal, J. L. (2015). Blue Spinel from the Luc Yen District of Vietnam. *Gems & Gemology*, 51, 2-17. <https://doi.org/10.5741/GEMS.51.1.2>
- Cooray, P. G. (1994). The precambrian of Sri Lanka: a historical review. *Precambrian Research*, 66(1), 3-18. [https://doi.org/https://doi.org/10.1016/0301-9268\(94\)90041-8](https://doi.org/https://doi.org/10.1016/0301-9268(94)90041-8)
- Crowningshield, R. (1967). Zoisite Crystals. *Gems & Gemology*, 12(7), 201-202.
- Cynn, H., Sharma, S. K., Cooney, T. F., & Nicol, M. (1992). High-temperature Raman investigation of order-disorder behavior in the MgAl₂O₄ spinel. *Physical Review B*, 45(1), 500-502. <https://doi.org/10.1103/PhysRevB.45.500>
- D'Ippolito, V., Andreozzi, G. B., Bosi, F., & Halenius, U. (2012). Blue spinel crystals in the MgAl₂O₄-CoAl₂O₄ series: Part I. Flux growth and chemical characterization. *American Mineralogist*, 97(11-12) , 1828-1833. <https://doi.org/10.2138/am.2012.4138>

- D'Ippolito, V., Andreozzi, G. B., Hålenius, U., Skogby, H., Hametner, K., & Günther, D. (2015). Color mechanisms in spinel: cobalt and iron interplay for the blue color. *Physics and Chemistry of Minerals*, 42(6), 431-439. <https://doi.org/10.1007/s00269-015-0734-0>
- Dahanayake, K. (1980). Modes of occurrence and provenance of Gemstones of Sri Lanka. *Mineralium Deposita*, 15, 81-86.
- Dahanayake, K., & Ranasinghe, A. P. (1985). Geology and mineralogy of gemming terrains of Sri Lanka. *Bulletin of the Geological Society of Finland*, 57, 139-149. <https://doi.org/10.17741/bgsf/57.1-2.011>
- Deer, W. A., Howie, R. A., & Zussman, J. (2013). *An Introduction to the Rock-Forming Minerals* (3 ed.) [Book]. Berforts Information Press.
- Dirlam, D. M., Misiorowski, E. B., Tozer, R., Stark, K. B., & Bassett, A. M. (1992). Gem Wealth of Tanzania. *Gems & Gemology*, 28(2), 80-102.
- Dollase, W. A. (1968). Refinement and comparison of the structures of zoisite and clinzoisite. *American Mineralogist*, 53(11-12), 1882-1898.
- Dubrail, J., & Farges, F. (2009). Not all chromates show the same pre-edge feature. Implications for the modelling of the speciation of Cr in environmental systems. *Journal of Physics: Conference Series*, 190. <https://doi.org/10.1088/1742-6596/190/1/012176>
- Eeckhout, S., Bolfan, N., McCammon, C., Klemme, S., & Amiguet, E. (2007). XANES study of the oxidation state of Cr in lower mantle phases: Periclase and magnesium silicate perovskite. *American Mineralogist - AMER MINERAL*, 92, 966-972. <https://doi.org/10.2138/am.2007.2318>
- Fandeur, D., Juillot, F., Morin, G., Olivi, L., Cognigni, A., Webb, S., Ambrosi, J.-P., Fritsch, E., Guyot, F., & Brown, G. (2009). XANES Evidence for Oxidation of Cr(III) to Cr(VI) by Mn-Oxides in a Lateritic Regolith Developed on Serpentinized Ultramafic Rocks of New Caledonia. *Environmental science & technology*, 43, 7384-7390. <https://doi.org/10.1021/es900498r>
- Farges, F. (2009). Chromium speciation in oxide-type compounds: Application to minerals, gems, aqueous solutions and silicate glasses. *Physics and Chemistry of Minerals*, 36, 463-481. <https://doi.org/10.1007/s00269-009-0293-3>
- Farges, F., Brown, G. E., & Rehr, J. J. (1996). Coordination chemistry of Ti(IV) in silicate glasses and melts: I. XAFS study of titanium coordination in oxide model compounds. *Geochimica et Cosmochimica Acta*, 60(16), 3023-3038. [https://doi.org/https://doi.org/10.1016/0016-7037\(96\)00144-5](https://doi.org/https://doi.org/10.1016/0016-7037(96)00144-5)
- Faye, G. H., & Nickel, E. H. (1971). On the pleochroism of vanadium-bearing zoisite from Tanzania. *The Canadian Mineralogist*, 10(5), 812-821.
- Fraas, L. M., Moore, J. E., & Salzberg, J. B. (1973). Raman characterization studies of synthetic and natural MgAl₂O₄ crystals. *The Journal of Chemical Physics*, 58(9), 3585-3592. <https://doi.org/10.1063/1.1679704>

- Franz, G., & Liebscher, A. (2004). Physical and Chemical Properties of the Epidote Minerals—An Introduction—. *Reviews in Mineralogy and Geochemistry*, 56(1), 1-81. <https://doi.org/10.2138/gsrmg.56.1.1>
- Fregola, R. A., Skogby, H., Bosi, F., D'Ippolito, V., Andreozzi, G. B., & Hålenius, U. (2014). Optical absorption spectroscopy study of the causes for color variations in natural Fe-bearing gahnite: Insights from iron valency and site distribution data†. *American Mineralogist*, 99(11-12), 2187-2195. <https://doi.org/10.2138/am-2014-4962>
- Fridrichová, J., Bacik, P., Rusinova, P., Antal, P., Škoda, R., Bizovská, V., & Miglierini, M. (2014). Optical and crystal-chemical changes in aquamarines and yellow beryls from Thanh Hoa province, Vietnam induced by heat treatment. *Physics and Chemistry of Minerals*, 42(2), 287-302. <https://doi.org/10.1007/s00269-014-0719-4>
- Gaffney, E. S. (1973). Spectra of Tetrahedral Fe²⁺ in MgAl₂O₄. *Physical Review B*, 8(7), 3484-3486. <https://doi.org/10.1103/PhysRevB.8.3484>
- Garcia-Guinea, J., Correcher, V., Rubio, J., & Valle-Fuentes, F. J. (2005). Effects of preheating on diaspore: Modifications in colour centres, structure and light emission. *Journal of Physics and Chemistry of Solids*, 66(7), 1220-1227. <https://doi.org/10.1016/j.jpcs.2005.04.001>
- Garnier, V., Ohnenstetter, D., Giuliani, G., Maluski, H., Deloule, E., Trinh, P., Van, L., & Quang, V. (2005). Age and significance of ruby-bearing marble from the Red River Shear Zone, northern Vietnam. *The Canadian Mineralogist*, 43, 1315-1329. <https://doi.org/10.2113/gscanmin.43.4.1315>
- Ghose, S., & Tsang, T. (1971). Ordering of V²⁺, Mn²⁺, and Fe³⁺ Ions in Zoisite, Ca₂Al₃Si₃O₁₂(OH). *Science*, 171(3969), 374-376. <https://doi.org/10.1126/science.171.3969.374>
- Giuli, G., Paris, E., Mungall, J., Romano, C., & Dingwell, D. (2004). V oxidation state and coordination number in silicate glasses by XAS. *American Mineralogist*, 89(11-12), 1640-1646. <https://doi.org/10.2138/am-2004-11-1208>
- Gorghinian, A., Rossi, A., Oltean, F., Esposito, A., & Marcelli, A. (2013). Investigating the colour of spinel: 1. Red gem-quality spinels (“balas”) from Ratnapura (Sri Lanka). *Rendiconti Lincei*, 24, 127-140. <https://doi.org/10.1007/s12210-013-0223-7>
- Gunawardene, M., & Rupasinghe, M. S. (1986). The Elahera Gem Field in Central Sri Lanka. *Gems & Gemology*, 22, 80-95.
- Hålenius, U., Skogby, H., & Andreozzi, G. B. (2002). Influence of cation distribution on the optical absorption spectra of Fe³⁺-bearing spinel s.s.-hercynite crystals: evidence for electron transitions in VFe²⁺-VFe³⁺ clusters. *Physics and Chemistry of Minerals*, 29(5), 319-330. <https://doi.org/10.1007/s00269-002-0240-z>
- Hauzenberger, C., Häger, T., Hofmeister, W., Quang, V. X., & Fernando, G. W. A. R. (2003). *Origin and formation of gem quality corundum from Vietnam*.

- Huggins, F. E., Najih, M., & Huffman, G. P. (1999). Direct speciation of chromium in coal combustion by-products by X-ray absorption fine-structure spectroscopy. *Fuel*, 78(2), 233-242. [https://doi.org/https://doi.org/10.1016/S0016-2361\(98\)00142-2](https://doi.org/https://doi.org/10.1016/S0016-2361(98)00142-2)
- Hughes, R. W., Pardieu, V., Soubiraa, G., and , & Schorr, D. (2006). *Moon over the Pamirs: Chasing ruby and spinel in Tajikistan* http://www.ruby-sapphire.com/tajikistan_ruby_and_spinel.htm
- Huong, L., Haeger, T., & Phan, L. (2017). Study of impurity in blue spinel from the Luc Yen mining area, Yen Bai province, Vietnam. *VIETNAM JOURNAL OF EARTH SCIENCES*, 40. <https://doi.org/10.15625/0866-7187/40/1/10915>
- Huong, L. T.-T., Häger, T., Hofmeister, W., Hauzenberger, C., Schwarz, D., Long, P. V., Wehmeister, U., Khoi, N. N., & Nhung, N. T. (2012). Gemstones from Vietnam: An update. *Gems & Gemology*, 48(3) , 158-176. <https://doi.org/http://dx.doi.org/10.5741/GEMS.48.3.158>.
- Hurlbut, C. S., Jr. (1969). Gem zoisite from Tanzania. *American Mineralogist*, 54(5-6), 702-709.
- Juhin, A., Brouder, C., Arrio, M.-A., Cabaret, D., Saintavit, P., Balan, E., Bordage, A., Seitsonen, A. P., Calas, G., Eeckhout, S. G., & Glatzel, P. (2008). X-ray Linear Dichroism in cubic compounds: the case of Cr³⁺ in MgAl₂O₄. *Physical Review B*, 78(19), 195103. <https://doi.org/10.1103/PhysRevB.78.195103>
- Juhin, A., Calas, G., Cabaret, D., Galoisy, L., & Hazemann, J.-L. (2007). Structural relaxation around substitutional Cr³⁺ in pyrope garnet. *Physical Review B*, 76(5), 054105. <https://doi.org/10.1103/PhysRevB.76.054105>
- Kammerling, R. C., Koivula, J. I., Johnson, M. L., DeGhionno, D., Hanni, H. A., & Schmetzer, K. (1995). Gem News: Tanzanites and other zoisites from Merelani, Tanzania. *Gems & Gemology*, 31, 285.
- Keller, P. C. (1983). The rubies of Burma: A review of the Mogok stone tract. *Gems & Gemology*, 19(4), 209-219.
- Krzemnicki, M., Wang, H., Stephan, T., & Henn, U. (2017). *Cobalt diffusion treated spinel*. <https://doi.org/10.13140/RG.2.2.12372.65929>
- Krzemnicki, M. S. (2011). Spinel, a gemstone on the rise. *Swiss Gemmological Institute*, 18, 3-4.
- Kunír, I. (2000). Mineral resources of Vietnam. *Acta Montanistica Slovaca*, 5.
- Lauf, R. J. (2011). Collector's Guide to the Epidote Group. *Rocks & Minerals*, 86(5), 444-457. <https://doi.org/10.1080/00357529.2011.602297>
- Liu, R. S., Cheng, Y. C., Gundakaram, R., & Jang, L. Y. (2001). Crystal and electronic structures of inverse spinel-type LiNiVO₄. *Materials Research Bulletin*, 36(7), 1479-1486. [https://doi.org/https://doi.org/10.1016/S0025-5408\(01\)00629-8](https://doi.org/https://doi.org/10.1016/S0025-5408(01)00629-8)
- Long, P. V., Pardieu, V., & Giuliani, G. (2013). Update on Gemstone Mining in Luc Yen, Vietnam. *Gems & Gemology*, 49(4) , 233-245. <https://www.gia.edu/gems-gemology/wn13-long-gemstone-mining-vietnam>

- Malisa, E. P. (2004). Petrology and lithogeochemistry of the mineralized tanzanite-grossular bearing rocks in the Merelani-Lelatema area, northeastern Tanzania. *Tanzania Journal of Science*, 29. <https://doi.org/10.4314/tjs.v29i2.18378>
- Mathavan, V., Kalubandara, S., & Fernando, G. W. A. R. (2000). Occurrences of two new types of gem deposits in the Okkampitiya gem field, Sri Lanka. *The Journal of Gemmology*, 27, 65-72.
- McClure, S. F., & Smith, C. P. (2000). Gemstone Enhancements and Detection in the 1990s. *Gems & Gemology*, 36(4), 336-359. <https://www.gia.edu/gems-gemmology/winter-2000-gemstone-enhancements-detection-1990s-mcclure>
- Mikenda, W. (1981). N-lines in the luminescence spectra of Cr³⁺-doped spinels (III) partial spectra. *Journal of Luminescence*, 26(1), 85-98. [https://doi.org/https://doi.org/10.1016/0022-2313\(81\)90171-X](https://doi.org/https://doi.org/10.1016/0022-2313(81)90171-X)
- Mills, S. J., Hatert, F., Nickel, E. H., & Ferraris, G. (2009). The standardisation of mineral group hierarchies: application to recent nomenclature proposals. *European Journal of Mineralogy*, 21(5), 1073-1080. <https://doi.org/10.1127/0935-1221/2009/0021-1994>
- Muhlmeister, S., Koivula, J. I., Kammerling, R. C., Smith, C. P., Fritsch, E., & Shigley, J. E. (1993). Flux-grown synthetic red and blue spinels from Russia. *Gems and Gemology*, 29(2), 81-98.
- Myat Phy, M., Franz, L., Bieler, E., Balmer, W., & Krzemnicki, M. (2019). Spinel from Mogok, Myanmar—A Detailed Inclusion Study by Raman Microspectroscopy and Scanning Electron Microscopy. *The Journal of Gemmology*, 36, 418-435. <https://doi.org/10.15506/JoG.2019.36.5.418>
- Myat Phy, M., Franz, L., Capitani, C., Balmer, W., Krzemnicki, M., & Christian, C. (2017). *Petrology and PT-conditions of quartz- and nepheline-bearing gneisses from Mogok Stone Tract, Myanmar*. <https://doi.org/10.13140/RG.2.2.32455.75681>
- Nassau, K. (2001). *The Physics and Chemistry of Color: The Fifteen Causes of Color* (2nd Edition ed.). A Wiley-Interscience Publication.
- Newville, M. (2013). Larch: An Analysis Package for XAFS and Related Spectroscopies. *Journal of Physics: Conference Series*, 430, 012007. <https://doi.org/10.1088/1742-6596/430/1/012007>
- Newville, M. (2014). Fundamentals of XAFS. *Reviews in Mineralogy and Geochemistry*, 78(1), 33-74. <https://doi.org/10.2138/rmg.2014.78.2>
- Nishikawa, S. (1915). Structure of Some Crystals of Spinel Group. *Proceedings of the Tokyo Mathemico-Physical Society. 2nd Series*, 8(7), 199-209_191. https://doi.org/10.11429/ptmps1907.8.7_199
- O'Neill, H. S. C., James, M., Dollase, W. A., & Redfern, S. A. T. (2005). Temperature dependence of the cation distribution in CuAl₂O₄ spinel. *European Journal of Mineralogy*, 17(4), 581-586. <https://doi.org/10.1127/0935-1221/2005/0017-0581>
- Odake, S., Fukura, S., Arakawa, M., Ohta, A., Harte, B., & Kagi, H. (2008). Divalent

- chromium in ferropicriase inclusions in lower-mantle diamonds revealed by micro-XANES measurements. *Journal of Mineralogical and Petrological Sciences*, 103(5), 350-353. <https://doi.org/10.2465/jmps.080620d>
- Olivier, B. (2006). The geology and petrology of the Merelani tanzanite deposit, NE Tanzania.
- Palke, A. C., & Sun, Z. (2018). What is cobalt spinel? Unraveling the causes of color in blue spinels. *Gems and Gemology*, 54(3), 262-263.
- Pardieu, V., & Soubiraa, G. (2006). *From Kashmir to Pamir, Summer 2006: Gemological expedition report to Ruby, Emerald and Spinel mining areas in Central Asia. Part 3: Tajikistan: Gems from the Pamirs* <http://schoolofgemology.com/HughesCircus/HughesShorr.pdf>
- Peretti, A., & Günther, D. (2003). Spinel from Namya. *Contributions to Gemology*, No. 2, August, p. 15-18.
- Peretti, A., Günther, D., & Haris, M. T. M. (2015). New Type of treatment of spinel involving heat-treatment and cobalt diffusion (Updated 22 May 2015), In: World of Magnificent Spinel. Provenance and Identification. *Contributions to Gemology*, 279-282.
- Peterson, M. L., Brown, G. E., & Parks, G. A. (1996). Quantitative Determination of Chromium Valence in Environmental Samples Using Xafs Spectroscopy. *MRS Proceedings*, 432, 75, Article 75. <https://doi.org/10.1557/PROC-432-75>
- Peterson, M. L., Brown, G. E., Parks, G. A., & Stein, C. L. (1997). Differential redox and sorption of Cr (III/VI) on natural silicate and oxide minerals: EXAFS and XANES results. *Geochimica et Cosmochimica Acta*, 61(16) , 3399-3412. [https://doi.org/https://doi.org/10.1016/S0016-7037\(97\)00165-8](https://doi.org/https://doi.org/10.1016/S0016-7037(97)00165-8)
- Phan, T., Phan, M.-H., & Han, T. (2004). Photoluminescence properties of Cr³⁺-doped MgAl₂O₄ natural spinel. *Journal-Korean Physical Society*, 45.
- Ravel, B. (2015) . *Introduction to X-ray Absorption Spectroscopy*. <https://www.bnl.gov/ps/userguide/lectures/Lecture-4-Ravel.pdf>
- Rees, J. A., Wandzilak, A., Maganas, D., Wurster, N. I. C., Hugenbruch, S., Kowalska, J. K., Pollock, C. J., Lima, F. A., Finkelstein, K. D., & DeBeer, S. (2016). Experimental and theoretical correlations between vanadium K-edge X-ray absorption and K β emission spectra. *Journal of Biological Inorganic Chemistry*, 21(5), 793-805. <https://doi.org/10.1007/s00775-016-1358-7>
- Ruiz, J. G. (2011) . *Applications of X-ray Absorption Spectroscopy in Physics and Material Science* <https://www.iucr.org/ data/assets/pdf file/0009/60984/IUCr2011-XAFS-Tutorial-J-Garcia-Ruiz.pdf>
- Saeseaw, S. (2015). Cobalt diffusion of natural spinel: a report describing a new treatment on the gem market. *News from research*.
- Saeseaw, S., Wang, W., Scarratt, K., Emmett, J., & Douthit, T. (2009). *Distinguishing*

- heated from unheated natural spinels - A short review.* Gemological Institute of America (GIA).
- Schmetzer, K., & Bank, H. (1978-1979). Bluish-green zoisite. *Gems & Gemology*, 16(4), 121-122.
- Schmetzer, K., Haxel, C., & Amthauer, G. (1989). Colour of natural spinels, gahnospinel and gahnites. *Neues Jahrbuch für Mineralogie, Abhandlungen (Journal of Mineralogy and Geochemistry)*, 159-180.
- Senoble, J. B. (2010). Beauty and rarity – A quest for Vietnamese blue spinels. *InColor, Summer*, 2-7.
- Shen, A. H., B. C. M., & DeGhionno, D. (2004). Lab Notes: Natural spinel identified with Photoluminescence. *Gems and Gemology*, 40(2), 168-169.
- Shigley, J. E., & Stockton, C. M. (1984). Cobalt-blue gem spinels. *Gems and Gemology*, 20, 34-41.
- Sickafus, K. E., Wills, J. M., & Grimes, N. W. (1999). Structure of Spinel. *Journal of the American Ceramic Society*, 82(12) , 3279-3292. <https://doi.org/https://doi.org/10.1111/j.1151-2916.1999.tb02241.x>
- Skvortsova, V., Mironova-Ulmane, N., & Riekstiņa, D. (2015). Structure and Phase Changes in Natural and Synthetic Magnesium Aluminum Spinel. *ENVIRONMENT. TECHNOLOGIES. RESOURCES. Proceedings of the International Scientific and Practical Conference; Vol 2 (2011): Environment. Technology. Resources. Proceedings of the 8th International Scientific and Practical Conference. Volume 2DO - 10. 17770/ etr2011vol2. 1002.* <http://journals.ru.lv/index.php/ETR/article/view/1002>
- Slotznick, S., & Shim, S.-H. (2008). In Situ Raman Spectroscopy Measurements of MgAl₂O₄ Spinel up to 1400°C. *American Mineralogist*, 93, 470-476. <https://doi.org/10.2138/am.2008.2687>
- Smith, C. P. (2011). Natural-Color Tanzanite. *Gems & Gemology*, 47(2), 119-120.
- Sutton, S. R., Karner, J., Papike, J., Delaney, J. S., Shearer, C., Newville, M., Eng, P., Rivers, M., & Dyar, M. D. (2005). Vanadium K edge XANES of synthetic and natural basaltic glasses and application to microscale oxygen barometry. *Geochimica et Cosmochimica Acta*, 69(9) , 2333-2348. <https://doi.org/https://doi.org/10.1016/j.gca.2004.10.013>
- Taran, M., Koch-Müller, M., & Langer, K. (2005). Electronic absorption spectroscopy of natural (Fe²⁺, Fe³⁺)-bearing spinels of spinel s.s.-hercynite and gahnite-hercynite solid solutions at different temperatures and high-pressures. *Physics and Chemistry of Minerals*, 32. <https://doi.org/10.1007/s00269-005-0461-z>
- Themelis, T. (2020). *GEMS & MINES OF MOGOK (MYANMAR)*.
- Villain, O., Calas, G., Galoisy, L., Cormier, L., & Hazemann, J.-L. (2007). XANES determination of chromium oxidation states in glasses: comparison with optical absorption spectroscopy. *Journal of the American Ceramic Society*, 90(11), 3578-

3581. <https://doi.org/10.1111/j.1551-2916.2007.01905.x>
- Waychunas, G. A., Apter, M. J., & Brown, G. E. (1983). X-ray K-edge absorption spectra of Fe minerals and model compounds: Near-edge structure. *Physics and Chemistry of Minerals*, 10(1), 1-9. <https://doi.org/10.1007/BF01204319>
- Westre, T. E., Kennepohl, P., DeWitt, J. G., Hedman, B., Hodgson, K. O., & Solomon, E. I. (1997). A Multiplet Analysis of Fe K-Edge 1s → 3d Pre-Edge Features of Iron Complexes. *Journal of the American Chemical Society*, 119(27), 6297-6314. <https://doi.org/10.1021/ja964352a>
- Wherry, E. T. (1929). Mineral determination by absorption spectra II. *American Mineralogist*, 14(9), 323-328.
- Widmer, R., Malsy, A.-K., & Armbruster, T. (2015). Effects of heat treatment on red gemstone spinel: single-crystal X-ray, Raman, and photoluminescence study. *Physics and Chemistry of Minerals*, 42(4), 251-260. <https://doi.org/10.1007/s00269-014-0716-7>
- Wilke, M., Farges, F., Petit, P., Brown, G., & Martin, F. (2001). Oxidation state and coordination of Fe in minerals: An Fe K-XANES spectroscopic study. *American Mineralogist*, 86, 714-730. <https://doi.org/10.2138/am-2001-5-612>
- Wilke, M., Partzsch, G., Bernhardt, R., & Lattard, D. (2005). Determination of the Iron Oxidation State in Basaltic Glasses Using XANES at K-edge. *Chemical Geology*, 213, 143-161. <https://doi.org/10.1016/j.chemgeo.2005.03.004>
- Wong, J., Lytle, F. W., Messmer, R. P., & Maylotte, D. H. (1984). K-edge absorption spectra of selected vanadium compounds. *Physical Review B*, 30(10), 5596-5610. <https://doi.org/10.1103/PhysRevB.30.5596>
- Wongkokua, W., Pongkrapan, S., Dararutana, P., T-Thienprasert, J., & Wathanakul, P. (2009). X-ray absorption near-edge structure of chromium ions in α-Al₂O₃. *Journal of Physics: Conference Series*, 185, 012054. <https://doi.org/10.1088/1742-6596/185/1/012054>
- Wood, D. L., Imbusch, G. F., Macfarlane, R. M., Kisliuk, P., & Larkin, D. M. (1968). Optical Spectrum of Cr³⁺ Ions in Spinel. *The Journal of Chemical Physics*, 48(11), 5255-5263. <https://doi.org/10.1063/1.1668202>
- Zaw, K., Sutherland, F., Yui, t.f., Meffre, S., & Thu, K. (2014). Vanadium-rich ruby and sapphire within Mogok Gemfield, Myanmar: implications for gem color and genesis. *Mineralium Deposita*, 50. <https://doi.org/10.1007/s00126-014-0545-0>



APPENDICES

จุฬาลงกรณ์มหาวิทยาลัย
CHULALONGKORN UNIVERSITY

APPENDIX A

Tanzanite XAS Spectra

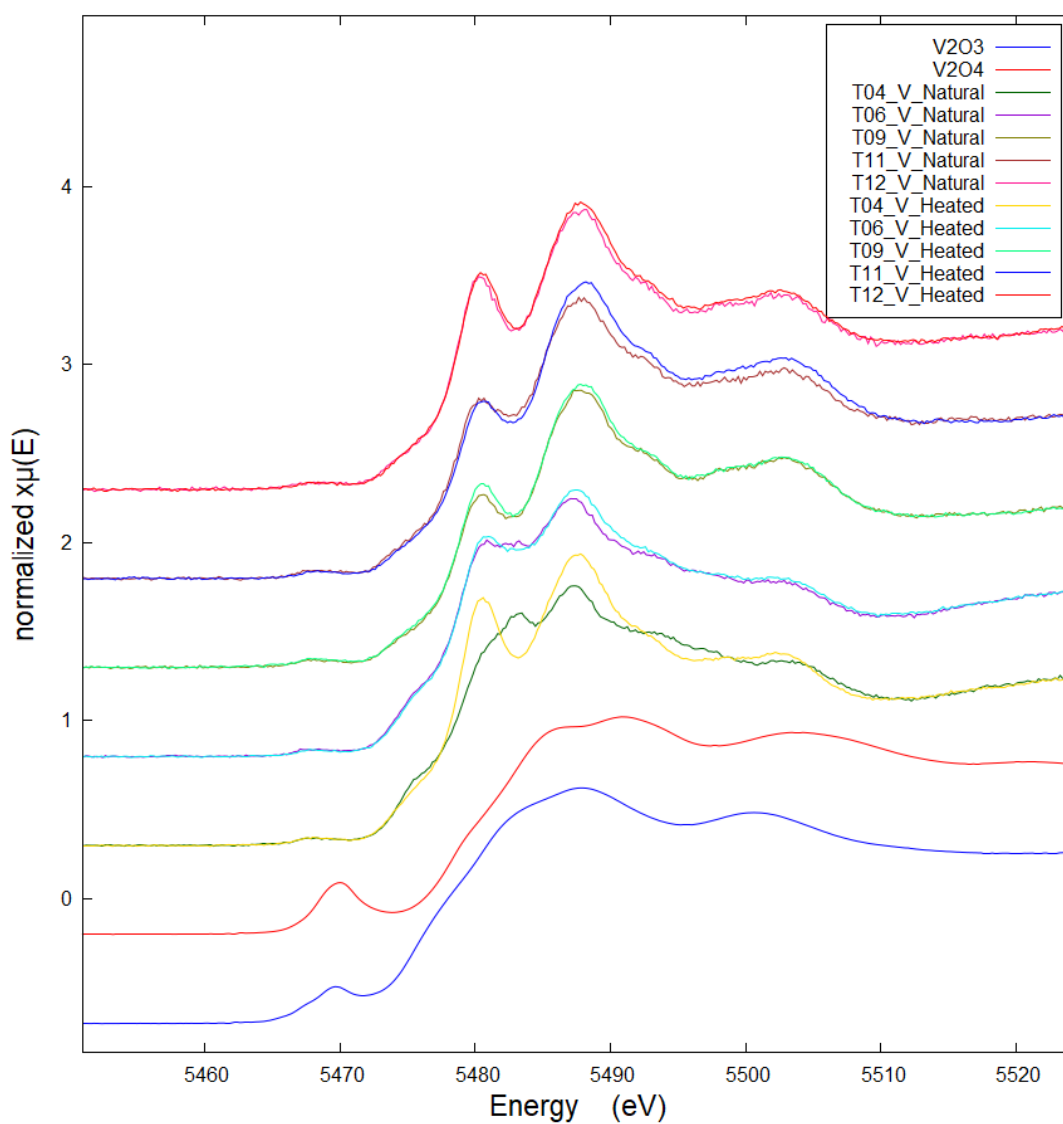


Figure 15 Normalized V K-edge XANES spectra of all natural and heated Tanzanite samples compared with vanadium standards.

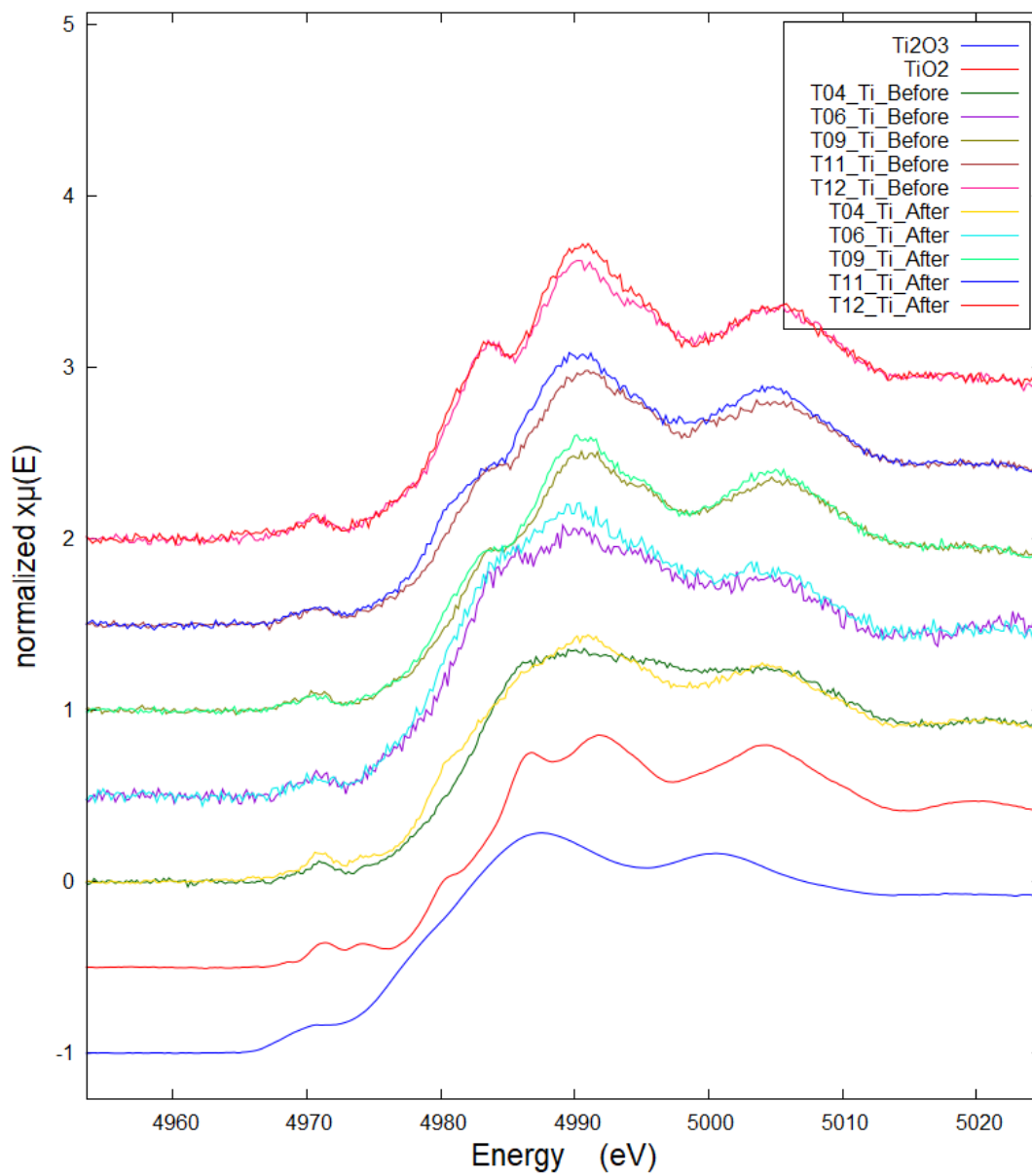


Figure 16 Normalized Ti K-edge XANES spectra of all natural and heated Tanzanite samples compared with titanium standards.

APPENDIX B

Tanzanite UV-Visible Absorption Spectra

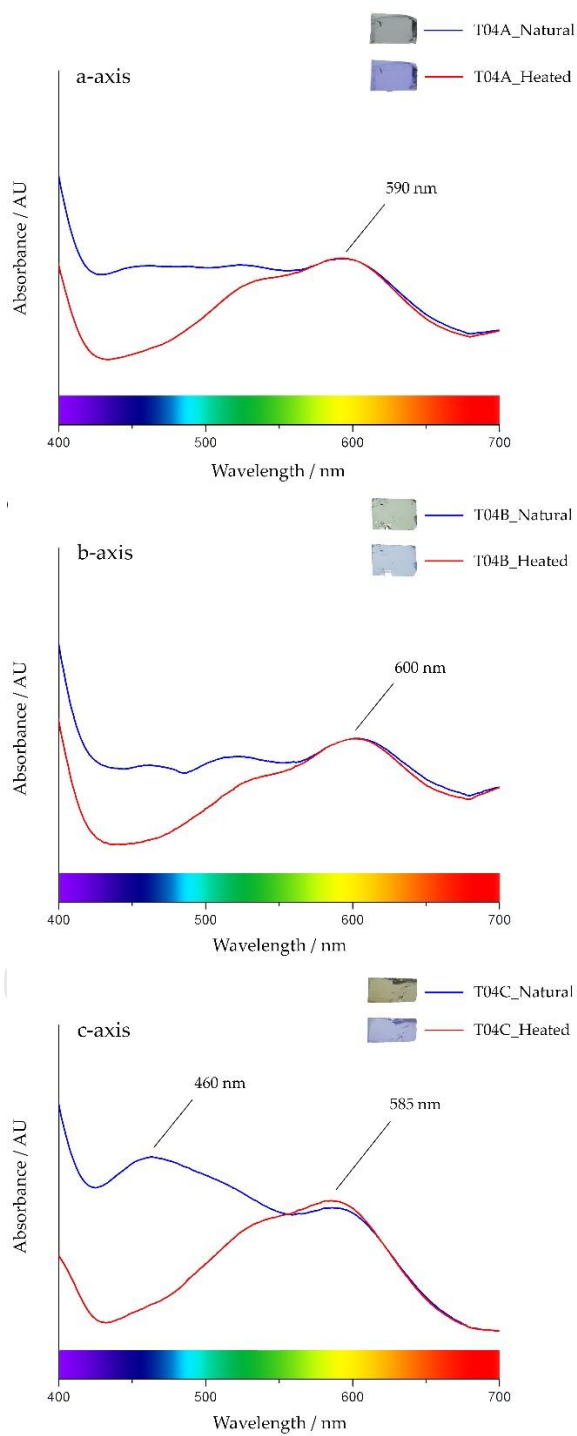


Figure 17 Visible absorption spectra of tanzanite sample T04 in three directions before (blue lines) and after (red lines) heating.

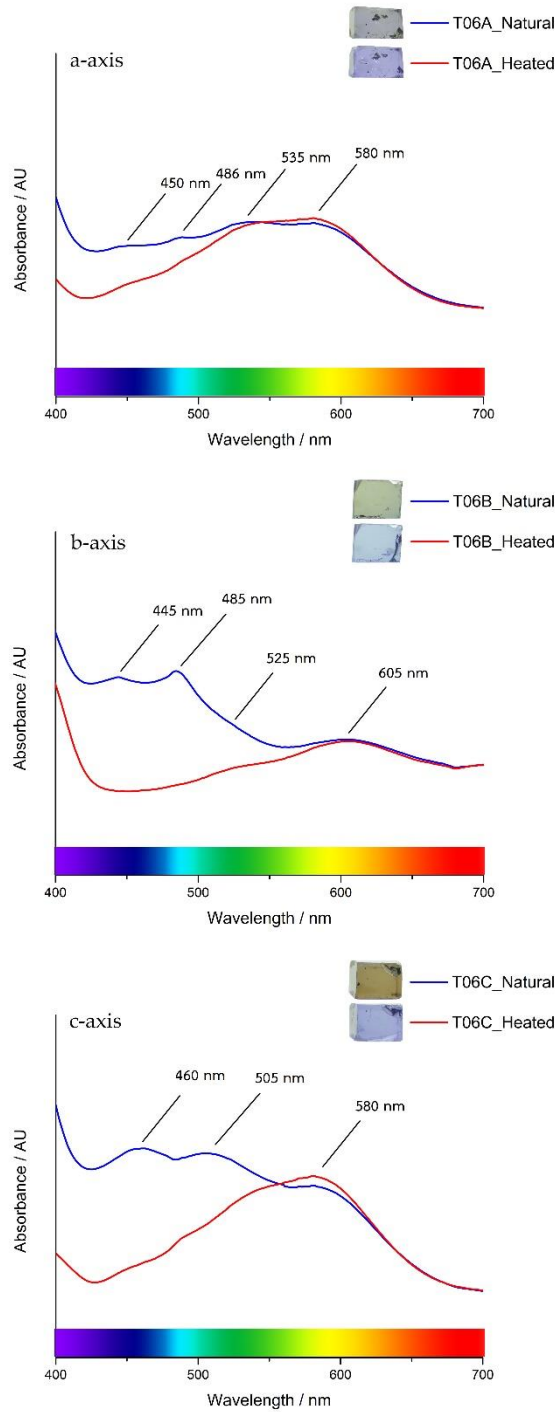


Figure 18 Visible absorption spectra of tanzanite sample T06 in three directions before (blue lines) and after (red lines) heating.

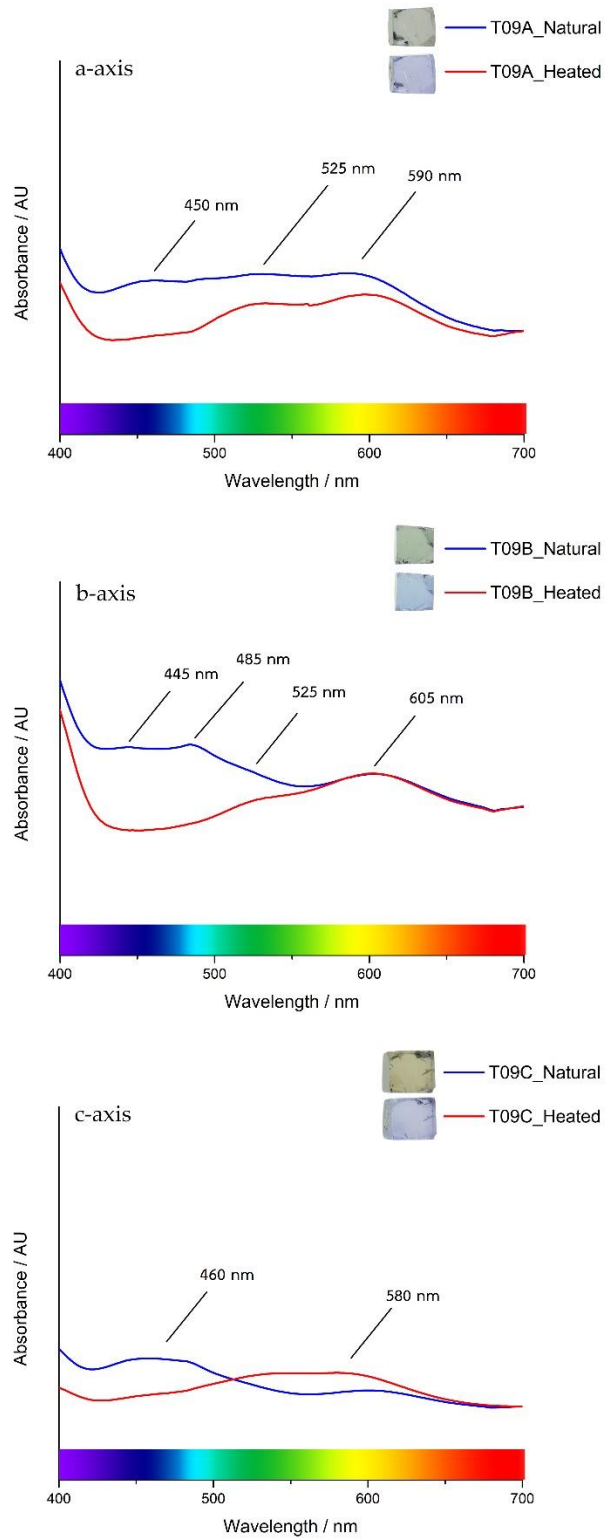


Figure 19 Visible absorption spectra of tanzanite sample T09 in three directions before (blue lines) and after (red lines) heating.

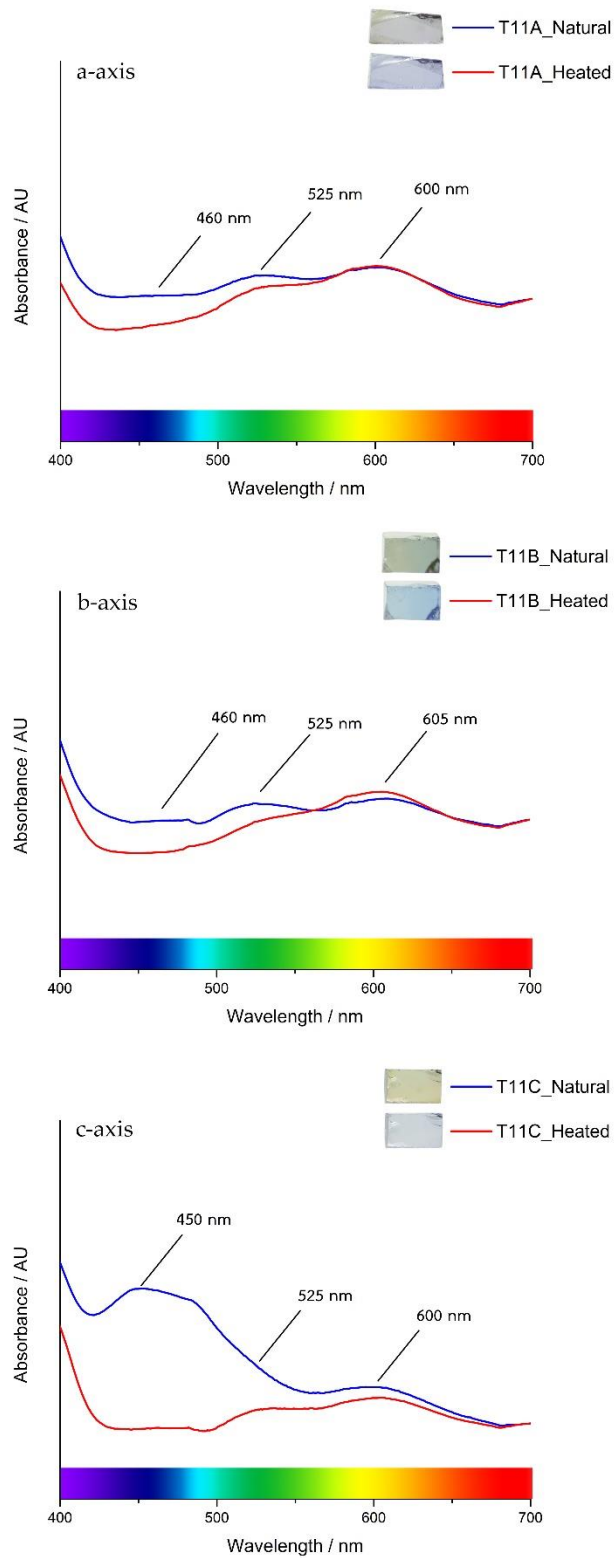


Figure 20 Visible absorption spectra of tanzanite sample T11 in three directions before (blue lines) and after (red lines) heating.

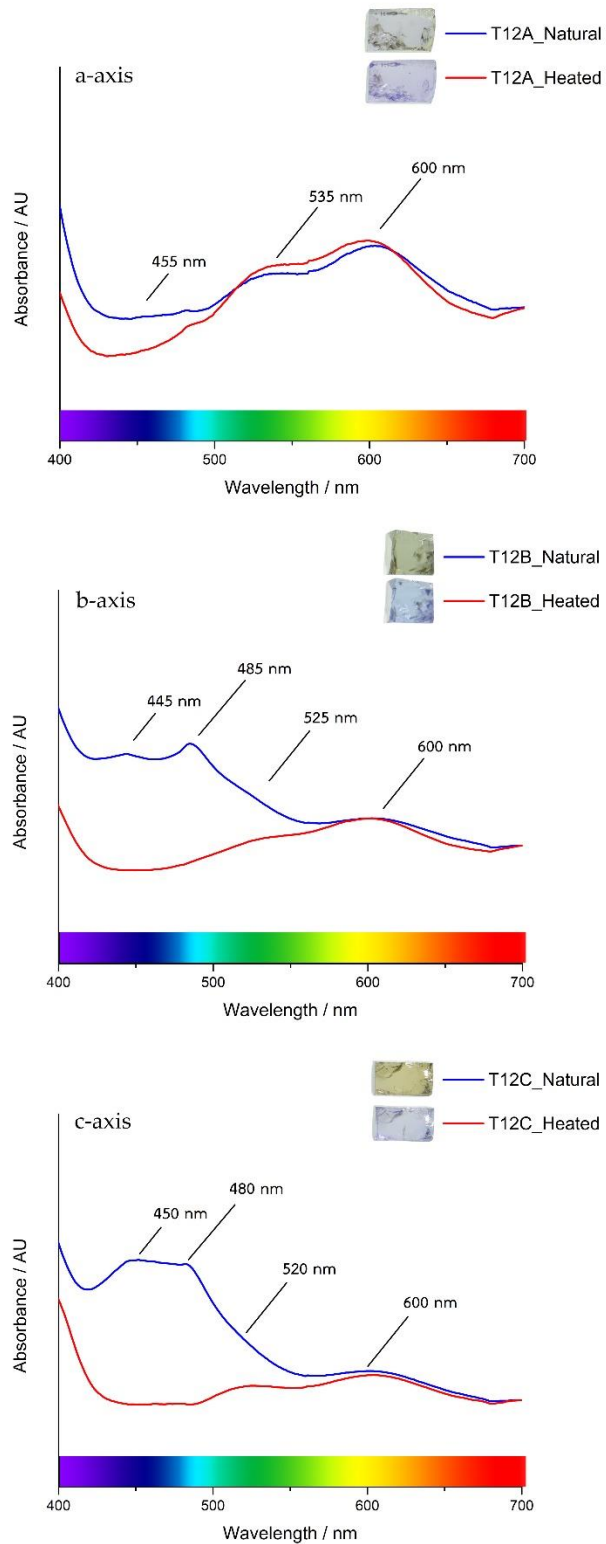


Figure 21 Visible absorption spectra of tanzanite sample T12 in three directions before (blue lines) and after (red lines) heating.

APPENDIX C

Spinel UV-Visible Absorption Spectra

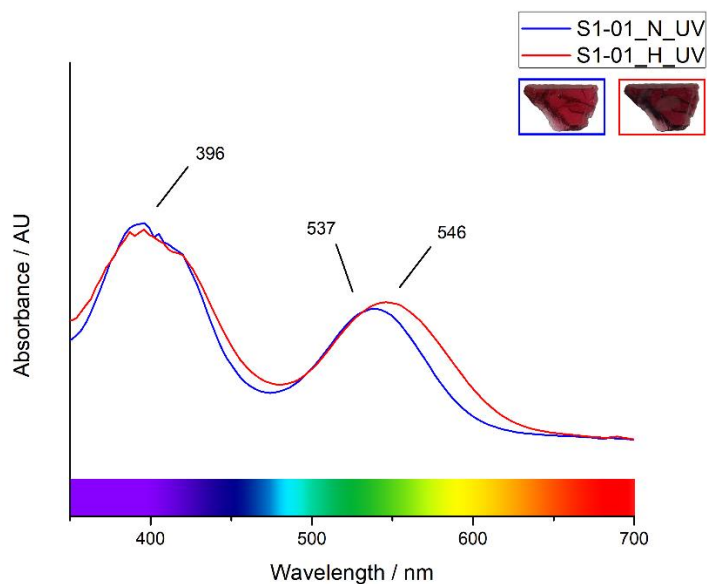


Figure 22 UV-visible absorption spectra of natural (blue line) and heated (red line) red spinel sample S1-01.

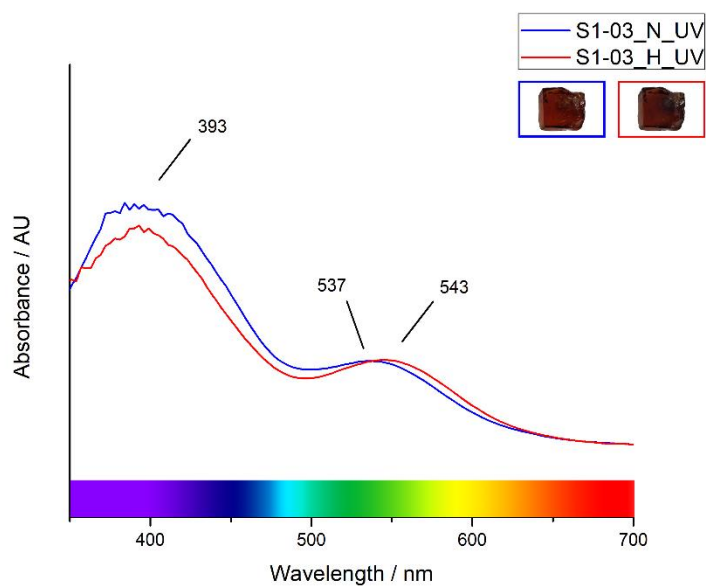


Figure 23 UV-visible absorption spectra of natural (blue line) and heated (red line) red spinel sample S1-03.

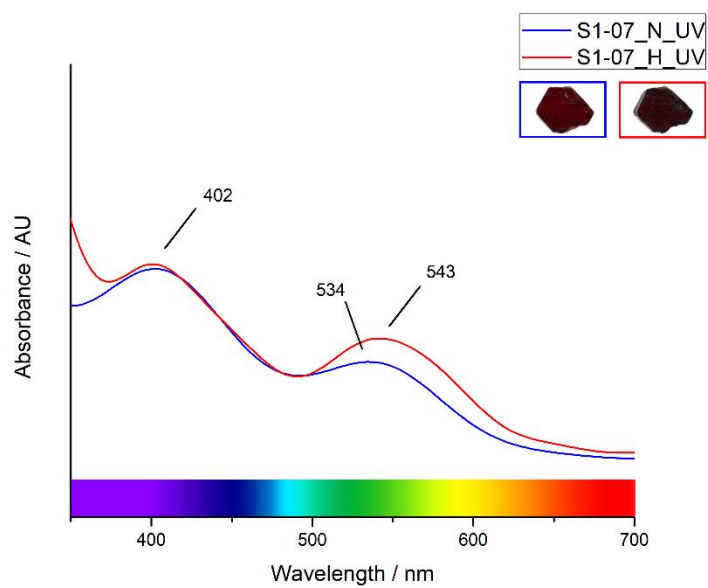


Figure 24 UV-visible absorption spectra of natural (blue line) and heated (red line) red spinel sample S1-07.

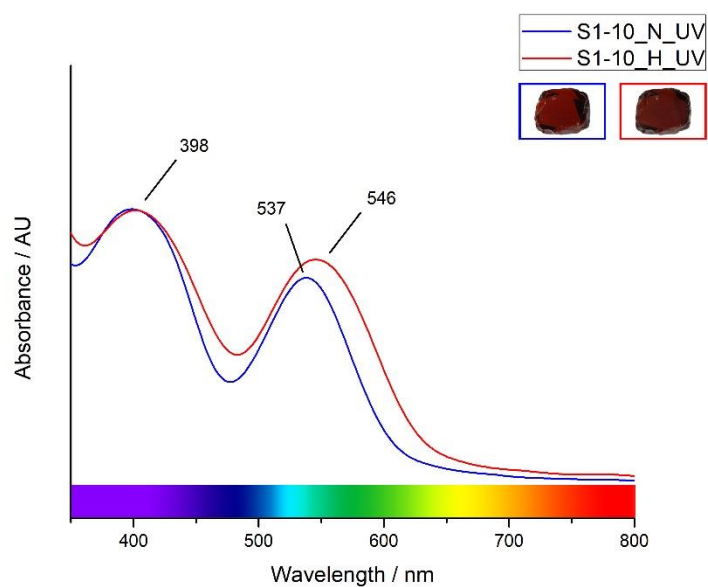


Figure 25 UV-visible absorption spectra of natural (blue line) and heated (red line) red spinel sample S1-10.

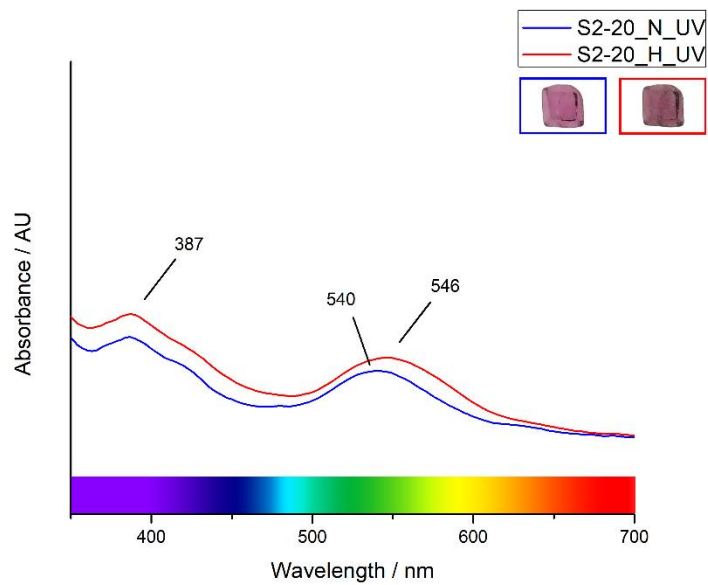


Figure 26 UV-visible absorption spectra of natural (blue line) and heated (red line) magenta spinel sample S2-20.

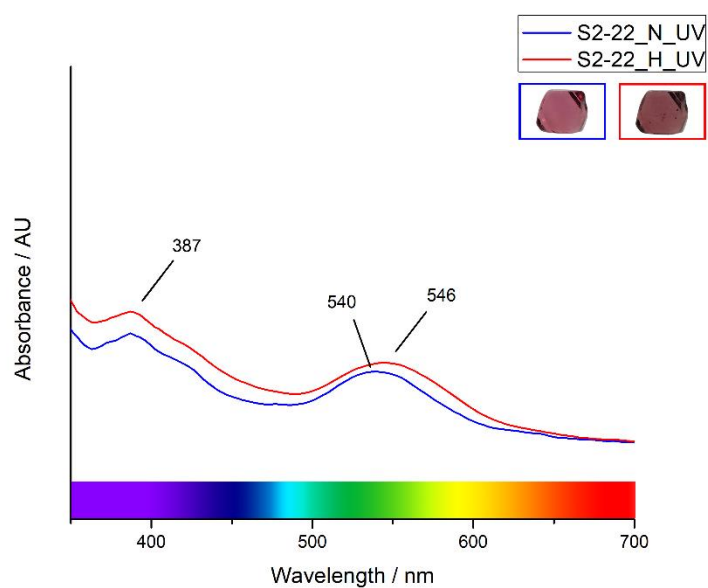


Figure 27 UV-visible absorption spectra of natural (blue line) and heated (red line) magenta spinel sample S2-22.

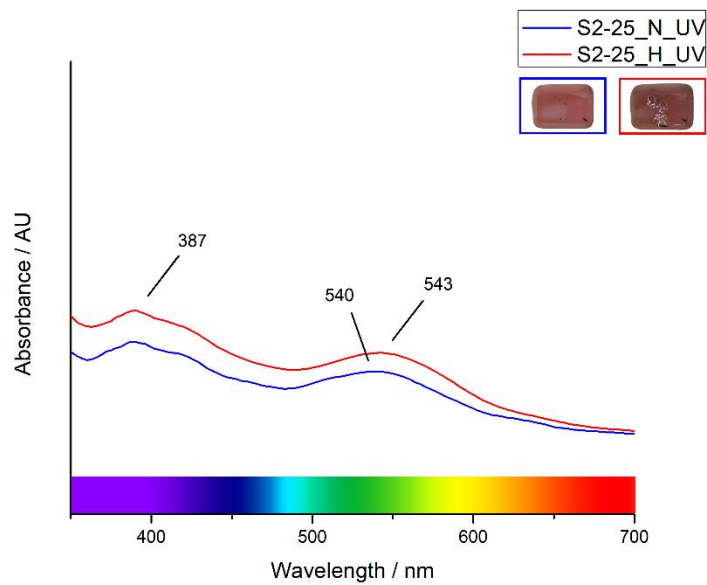


Figure 28 UV-visible absorption spectra of natural (blue line) and heated (red line) magenta spinel sample S2-25.

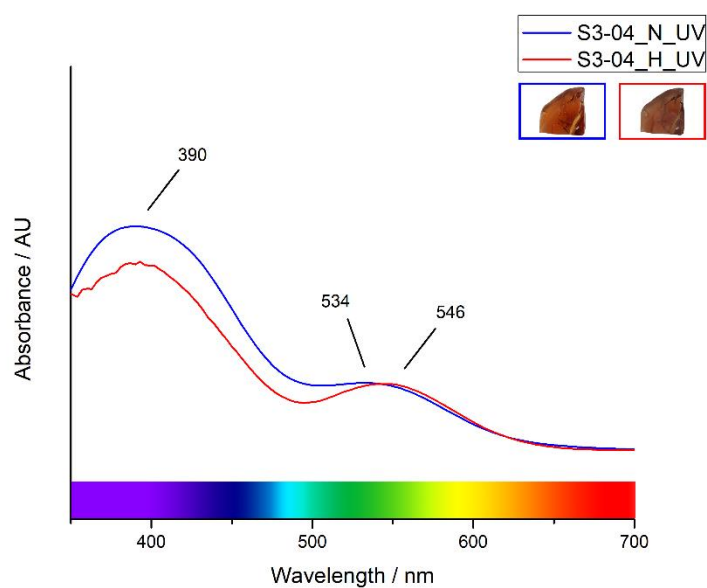


Figure 29 UV-visible absorption spectra of natural (blue line) and heated (red line) orange spinel sample S3-04.

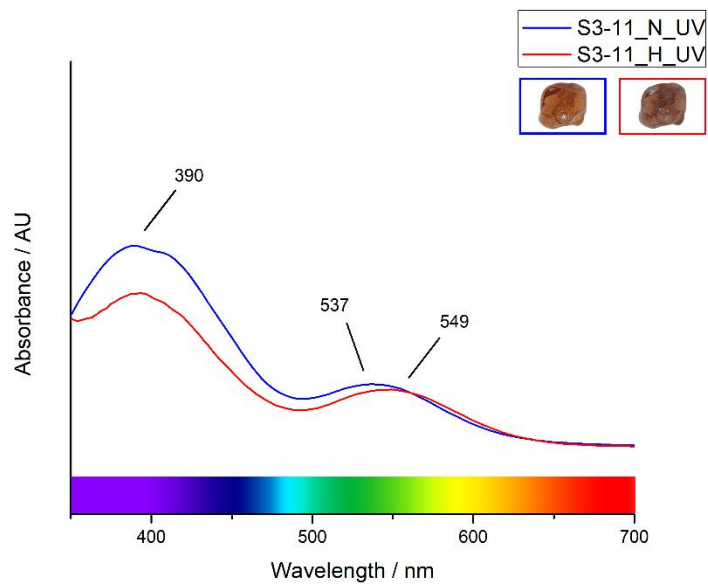


Figure 30 UV-visible absorption spectra of natural (blue line) and heated (red line) orange spinel sample S3-11.

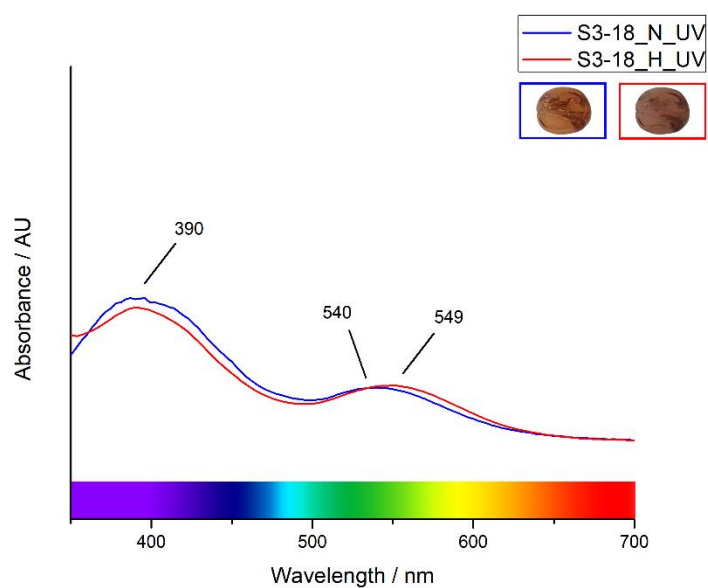


Figure 31 UV-visible absorption spectra of natural (blue line) and heated (red line) orange spinel sample S3-18.

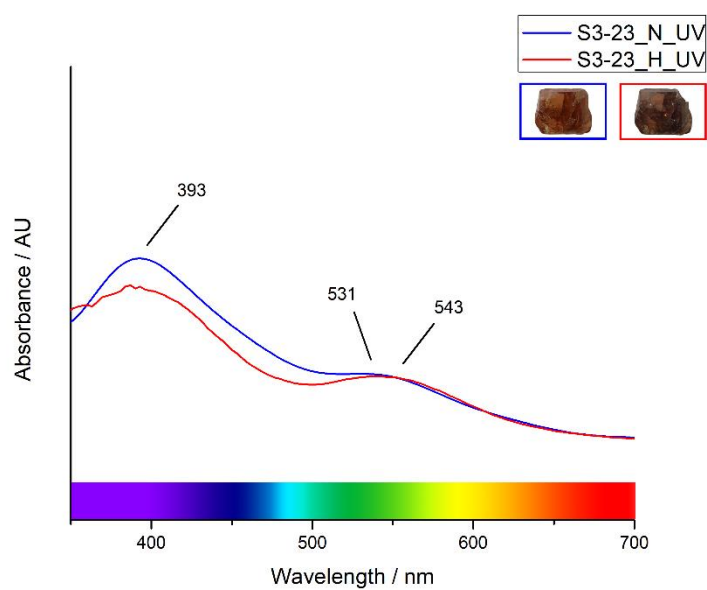


Figure 32 UV-visible absorption spectra of natural (blue line) and heated (red line) orange spinel sample S3-23.

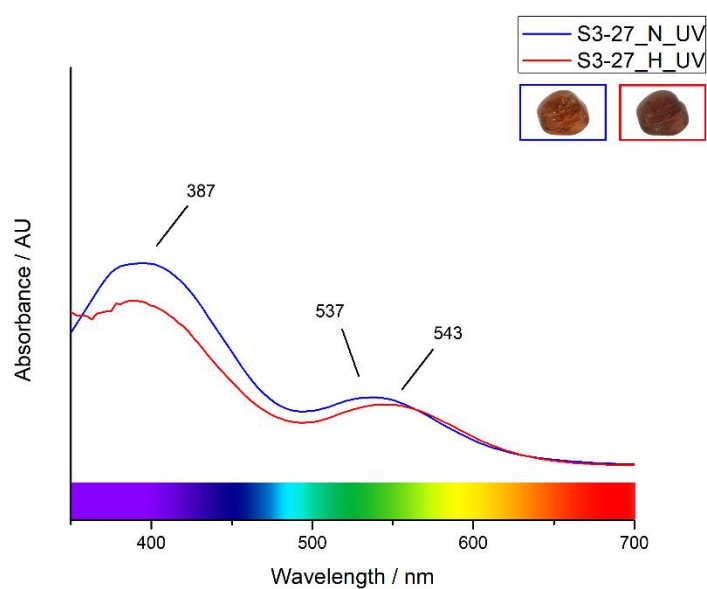


Figure 33 UV-visible absorption spectra of natural (blue line) and heated (red line) orange spinel sample S3-27.

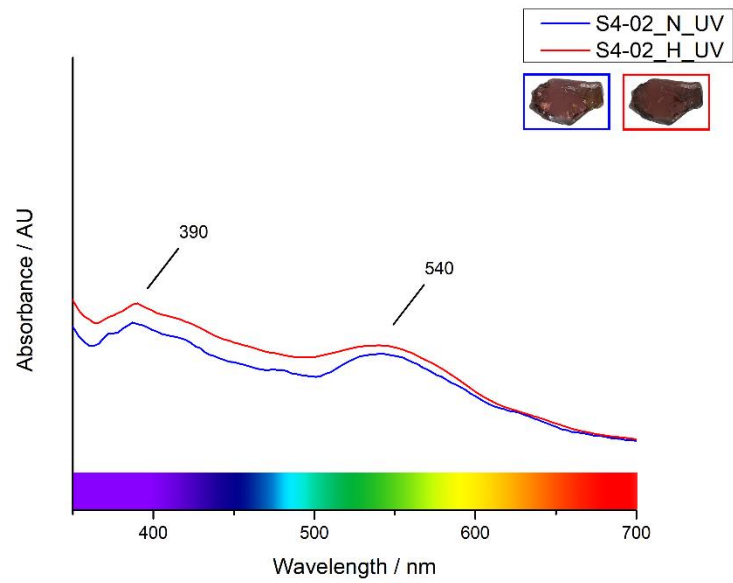


Figure 34 UV-visible absorption spectra of natural (blue line) and heated (red line) red-purple spinel sample S4-02.

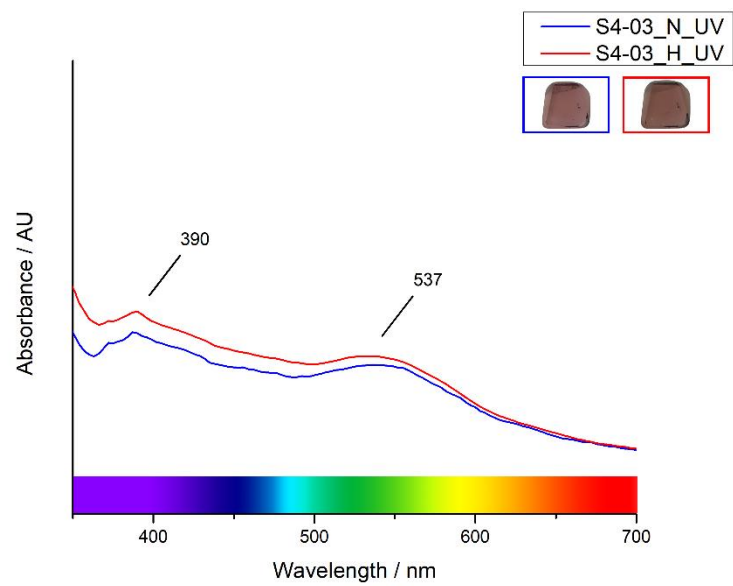


Figure 35 UV-visible absorption spectra of natural (blue line) and heated (red line) red-purple spinel sample S4-03.

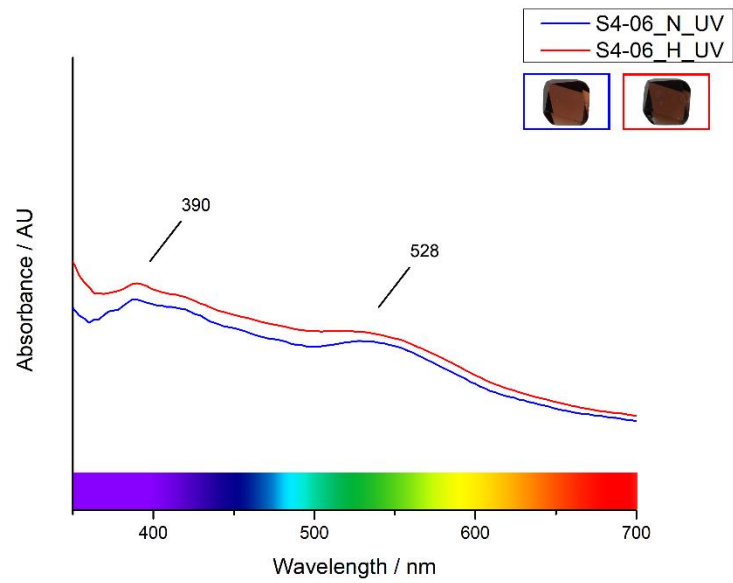


Figure 36 UV-visible absorption spectra of natural (blue line) and heated (red line) red-purple spinel sample S4-06.

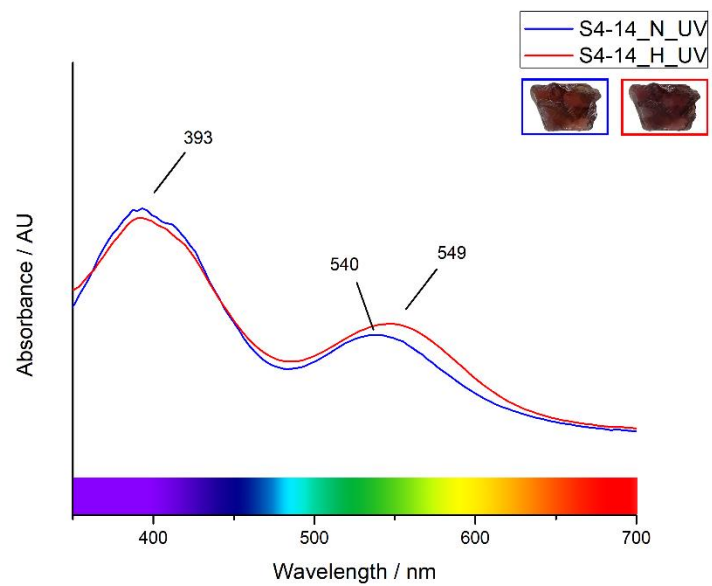


Figure 37 UV-visible absorption spectra of natural (blue line) and heated (red line) red-purple spinel sample S4-14.

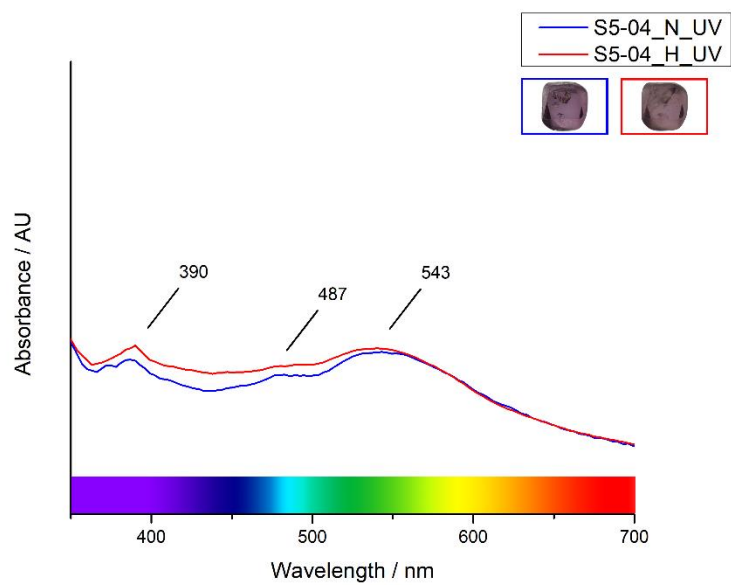


Figure 38 UV-visible absorption spectra of natural (blue line) and heated (red line) purple spinel sample S5-04.

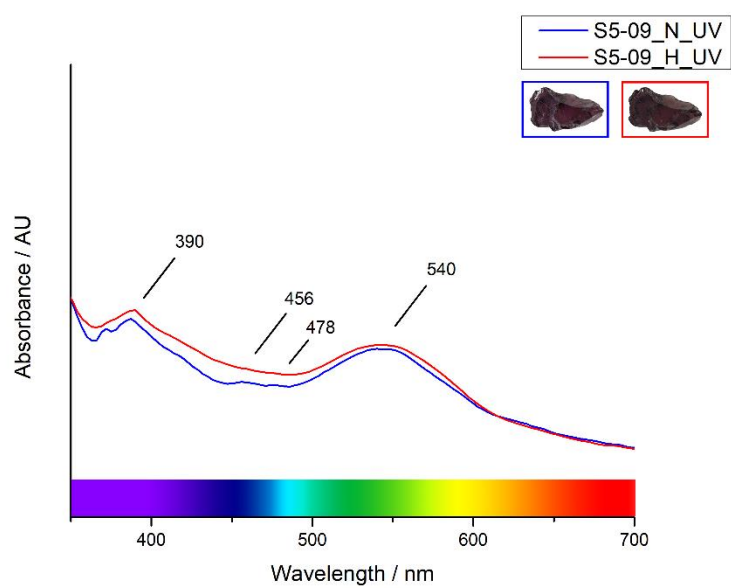


Figure 39 UV-visible absorption spectra of natural (blue line) and heated (red line) purple spinel sample S5-09.

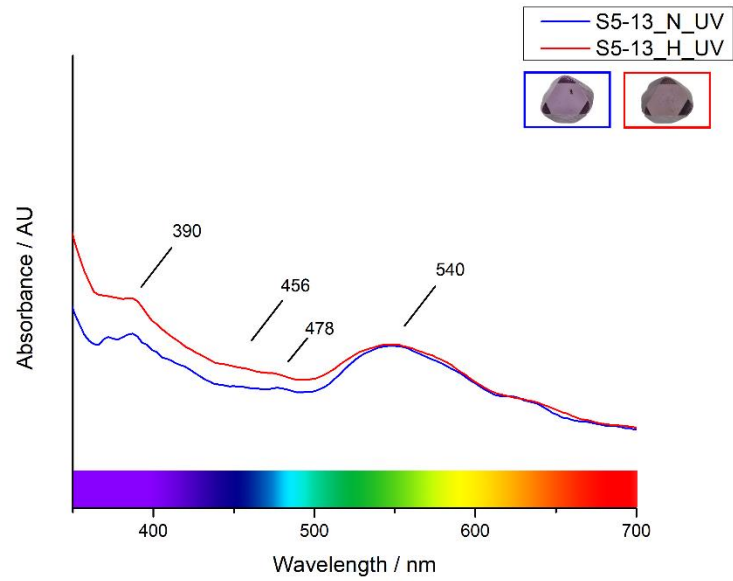


Figure 40 UV-visible absorption spectra of natural (blue line) and heated (red line) purple spinel sample S5-13.

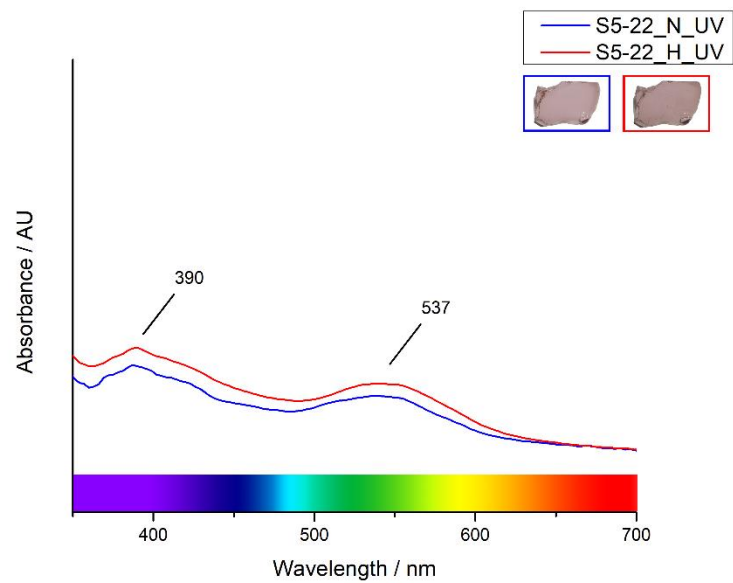


Figure 41 UV-visible absorption spectra of natural (blue line) and heated (red line) purple spinel sample S5-22.

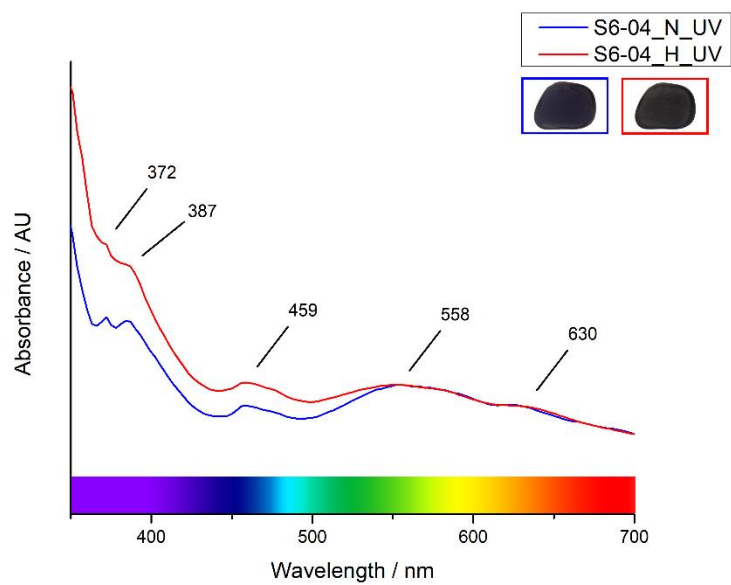


Figure 42 UV-visible absorption spectra of natural (blue line) and heated (red line) blue spinel sample S6-04.

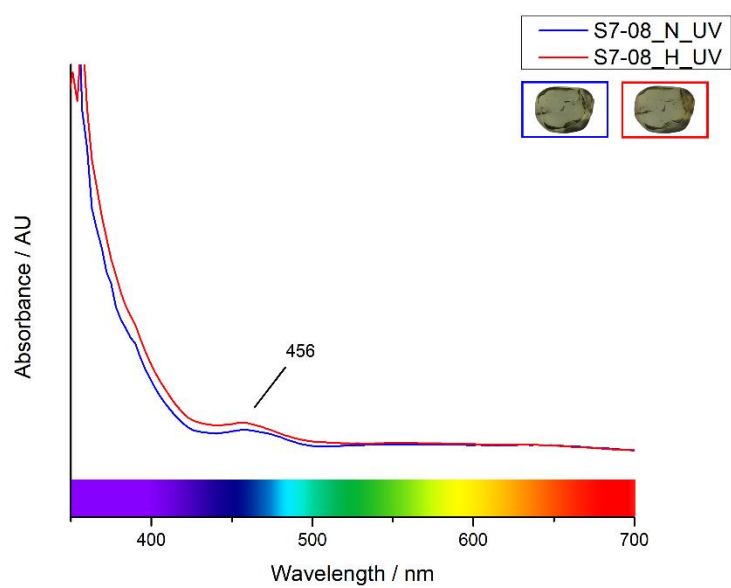


Figure 43 UV-visible absorption spectra of natural (blue line) and heated (red line) green spinel sample S7-08.

APPENDIX D

Spinel Raman Spectra

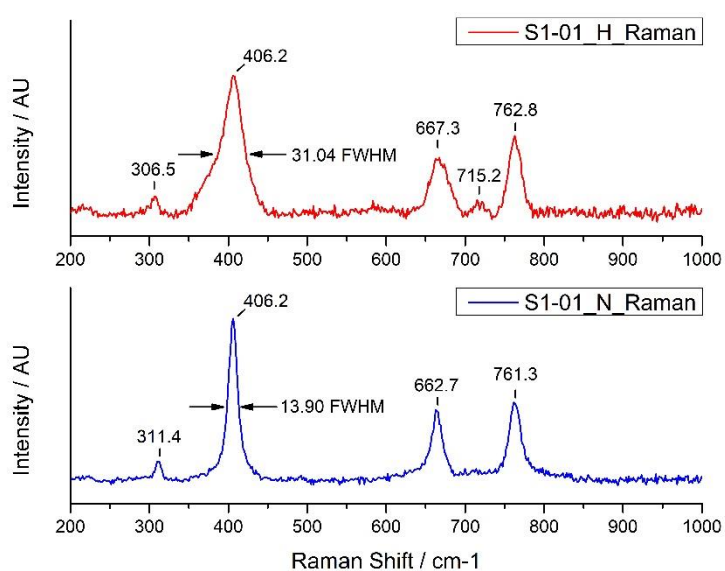


Figure 44 Raman spectra of natural (blue line) and heated (red line) spinel S1-01.

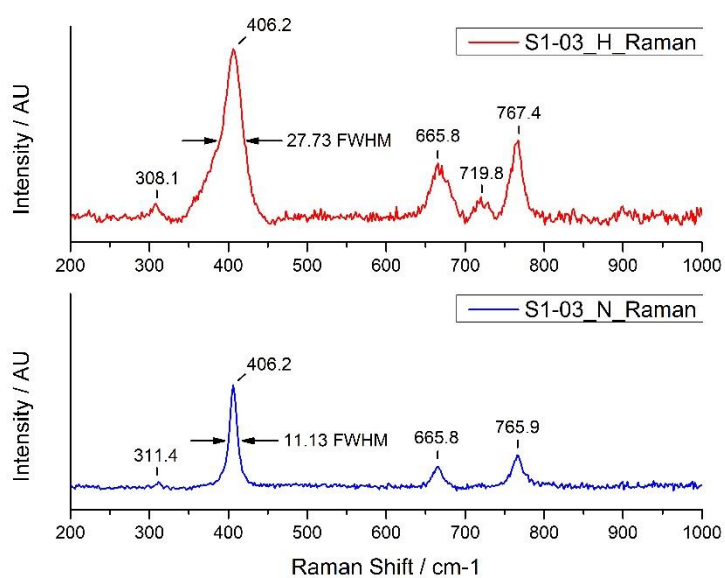


Figure 45 Raman spectra of natural (blue line) and heated (red line) spinel S1-03.

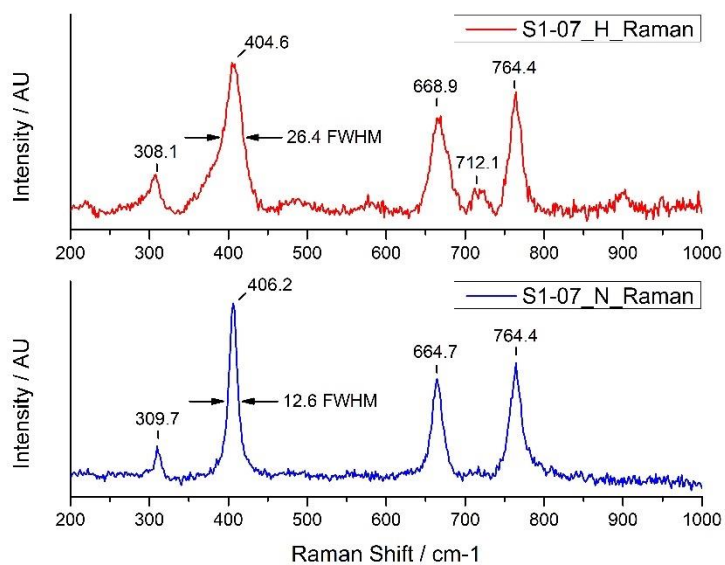


Figure 46 Raman spectra of natural (blue line) and heated (red line) spinel S1-07.

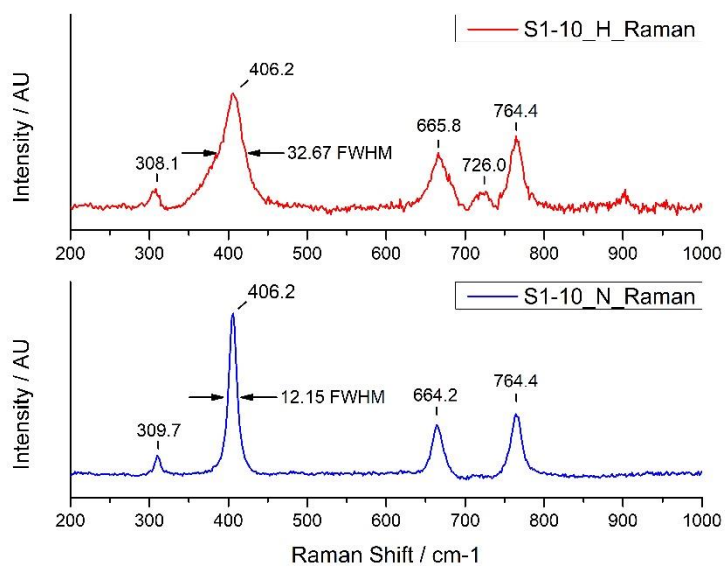


Figure 47 Raman spectra of natural (blue line) and heated (red line) spinel S1-10.

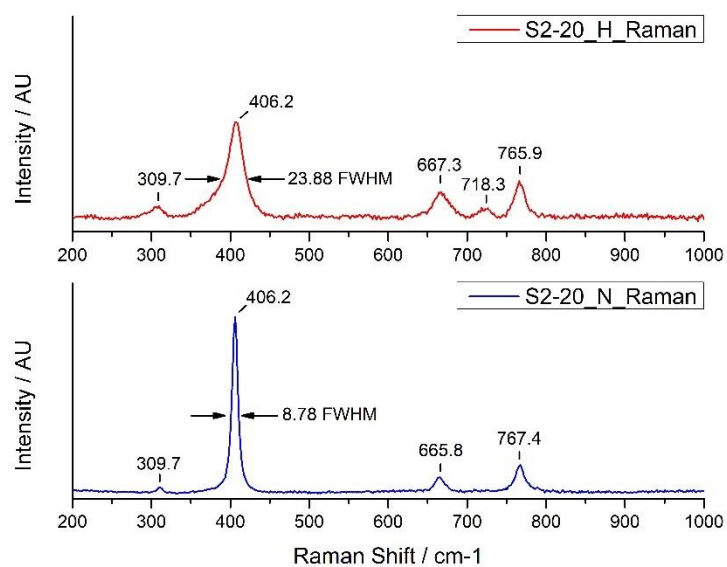


Figure 48 Raman spectra of natural (blue line) and heated (red line) spinel S2-20.

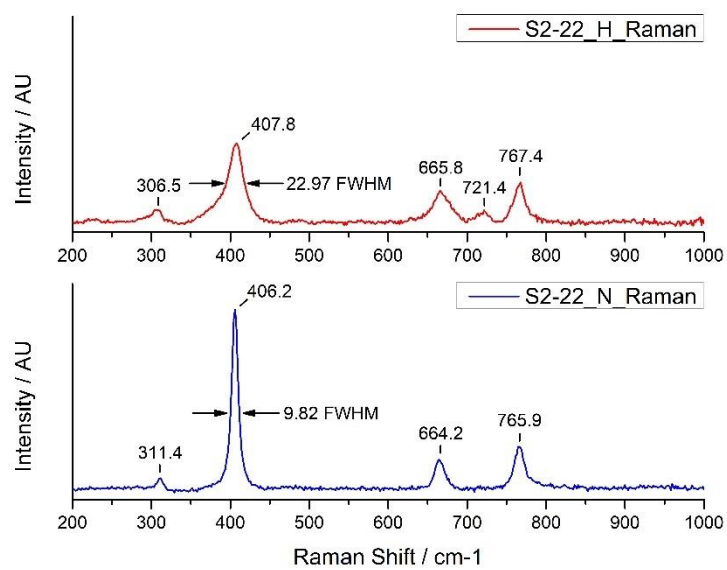


Figure 49 Raman spectra of natural (blue line) and heated (red line) spinel S2-22.

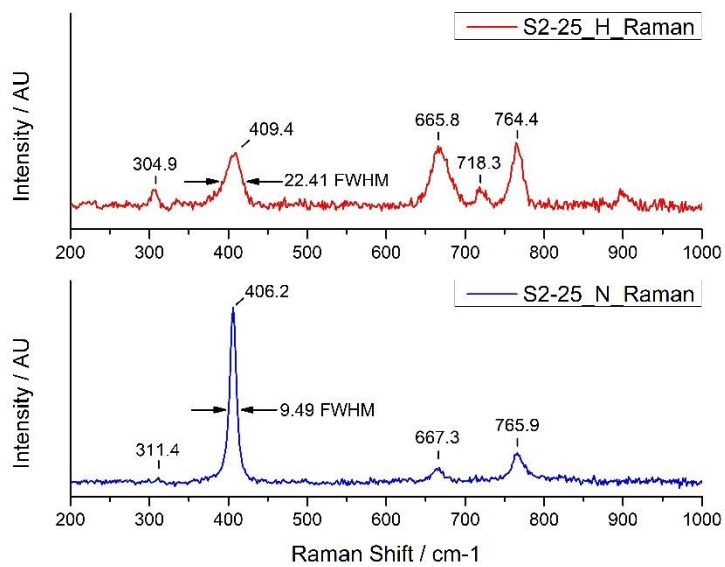


Figure 50 Raman spectra of natural (blue line) and heated (red line) spinel S2-25.

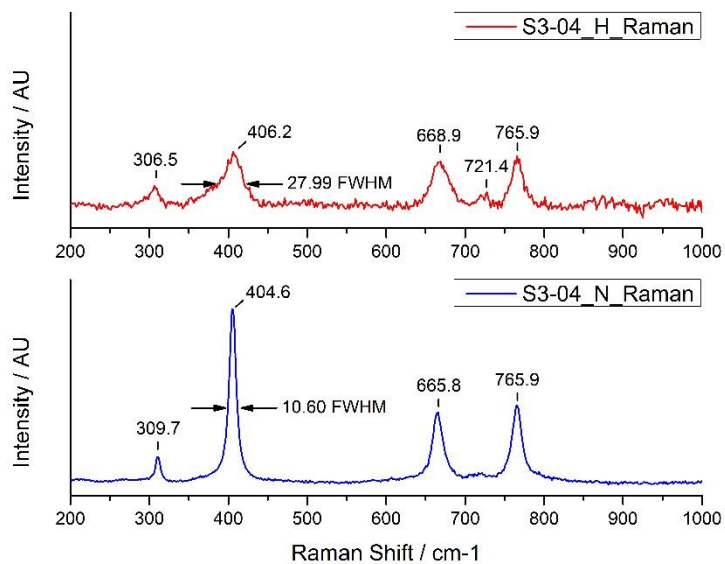


Figure 51 Raman spectra of natural (blue line) and heated (red line) spinel S3-04.

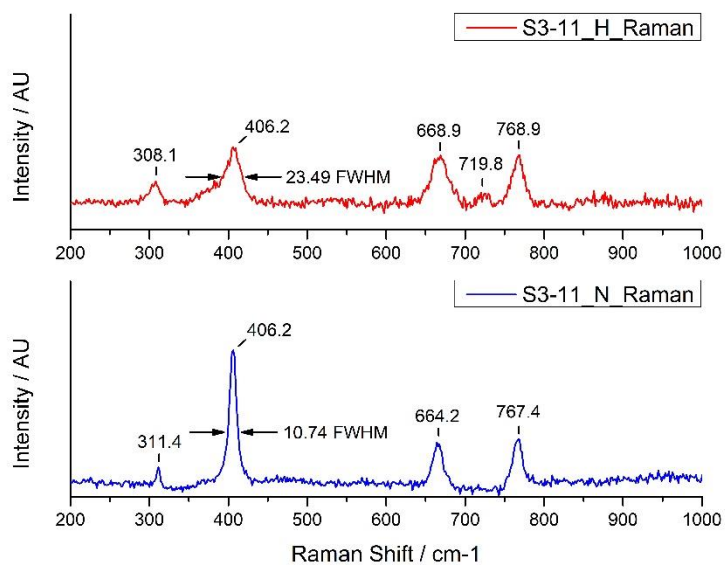


Figure 52 Raman spectra of natural (blue line) and heated (red line) spinel S3-11.

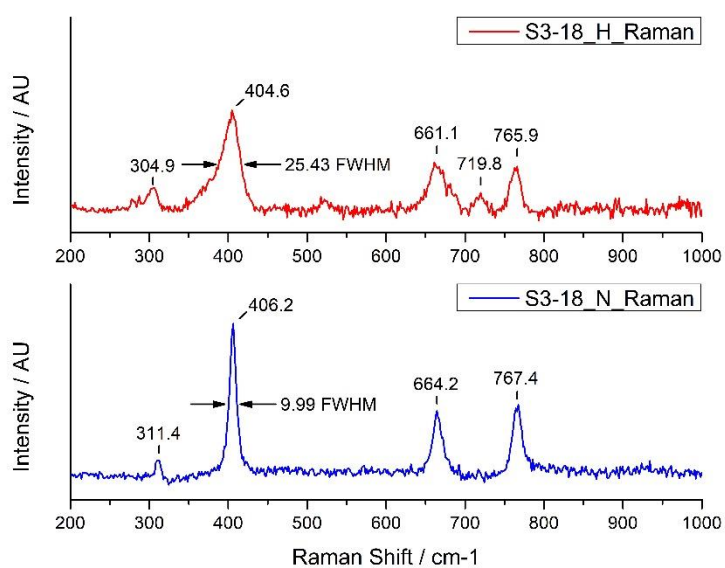


Figure 53 Raman spectra of natural (blue line) and heated (red line) spinel S3-18.

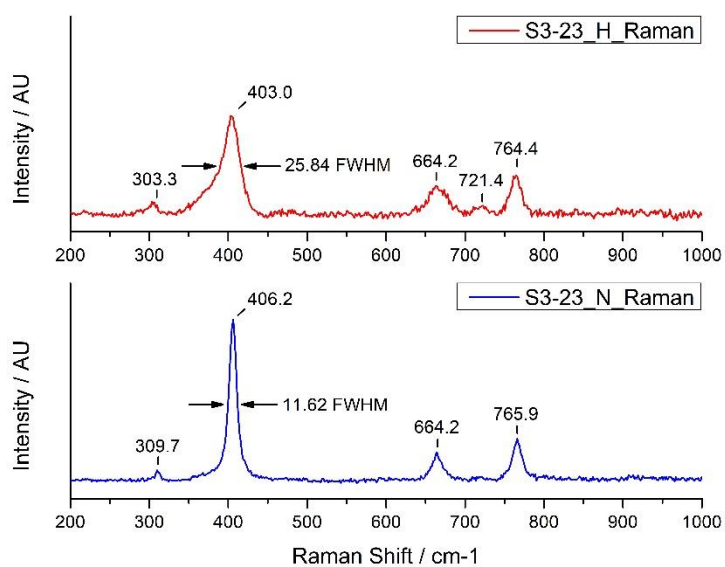


Figure 54 Raman spectra of natural (blue line) and heated (red line) spinel S3-23.

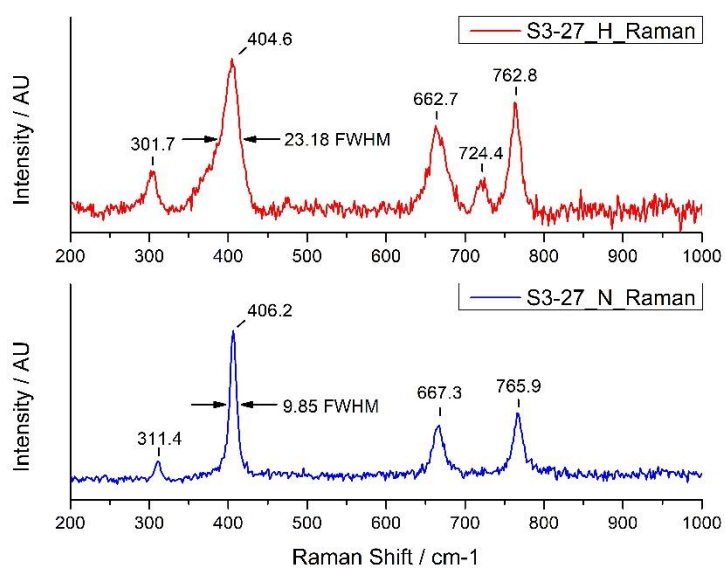


Figure 55 Raman spectra of natural (blue line) and heated (red line) spinel S3-27.

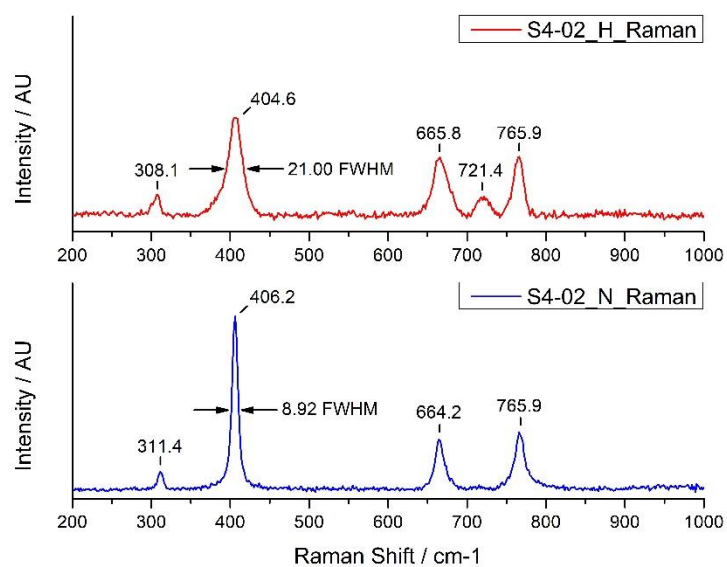


Figure 56 Raman spectra of natural (blue line) and heated (red line) spinel S4-02.

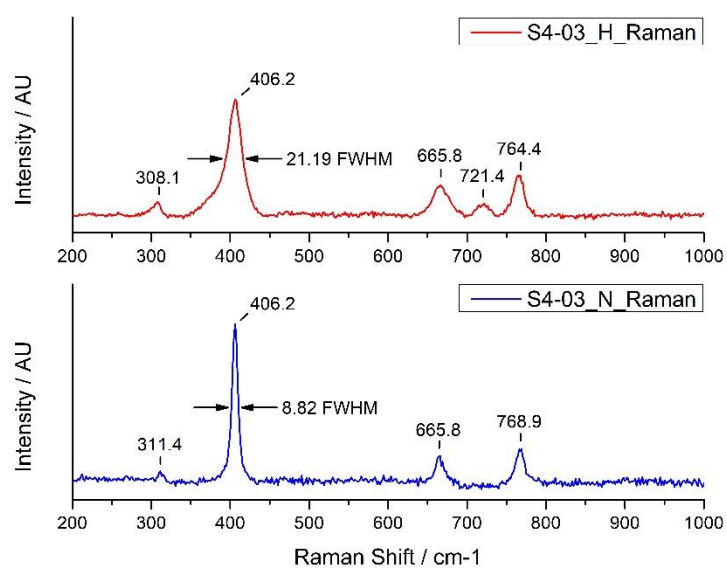


Figure 57 Raman spectra of natural (blue line) and heated (red line) spinel S4-03.

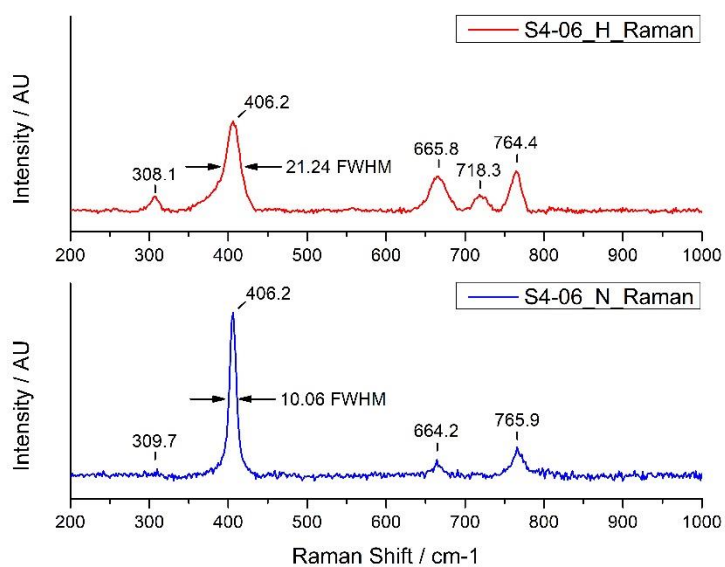


Figure 58 Raman spectra of natural (blue line) and heated (red line) spinel S4-06.

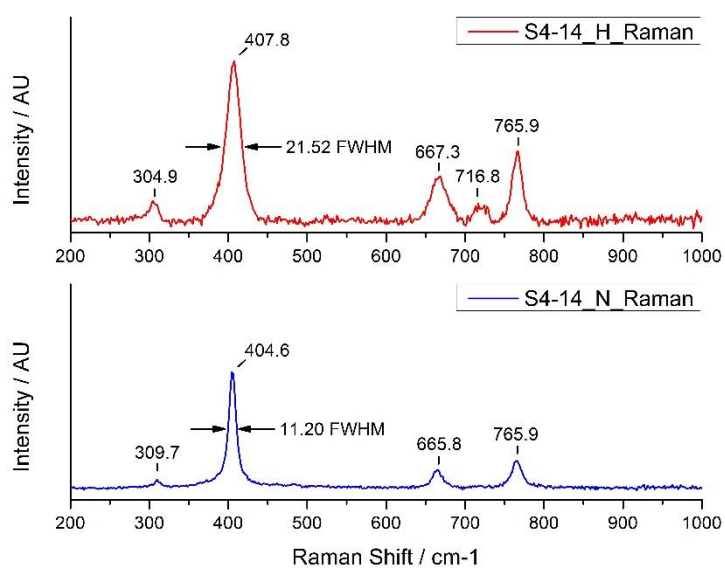


Figure 59 Raman spectra of natural (blue line) and heated (red line) spinel S4-14.

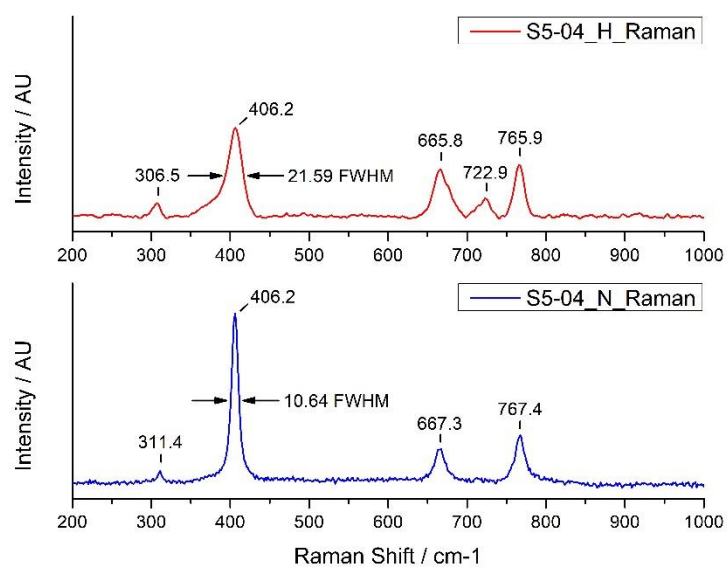


Figure 60 Raman spectra of natural (blue line) and heated (red line) spinel S5-04.

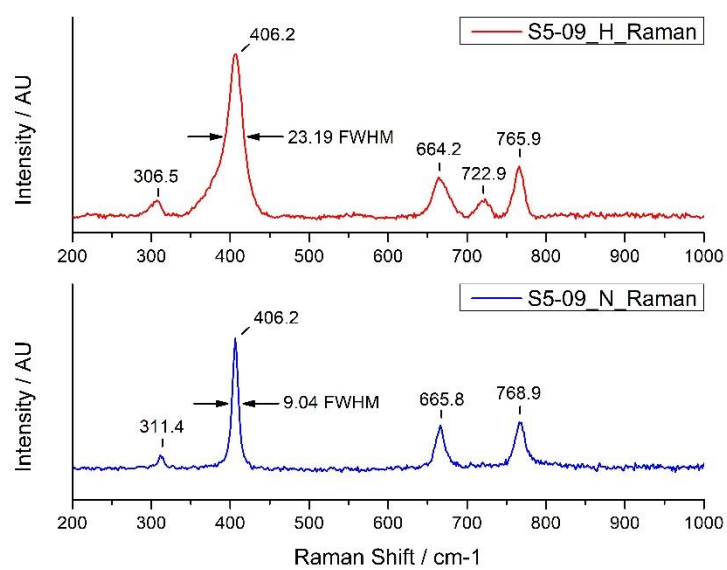


Figure 61 Raman spectra of natural (blue line) and heated (red line) spinel S5-09.

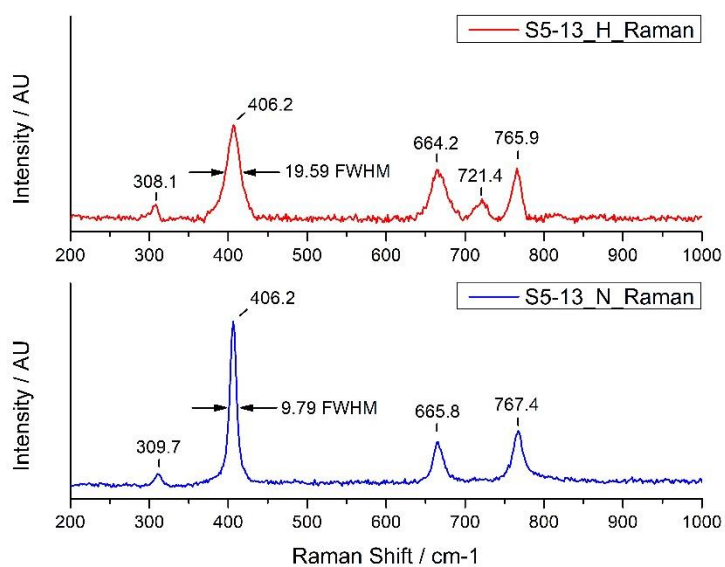


Figure 62 Raman spectra of natural (blue line) and heated (red line) spinel S5-13.

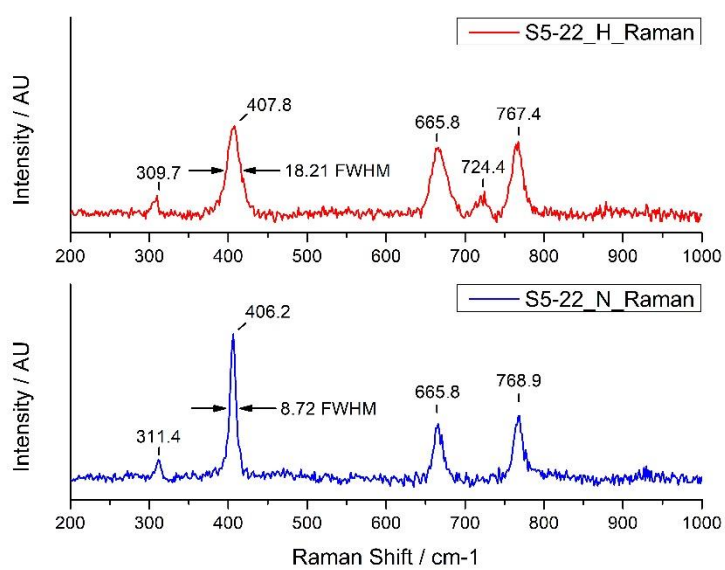


Figure 63 Raman spectra of natural (blue line) and heated (red line) spinel S5-22.

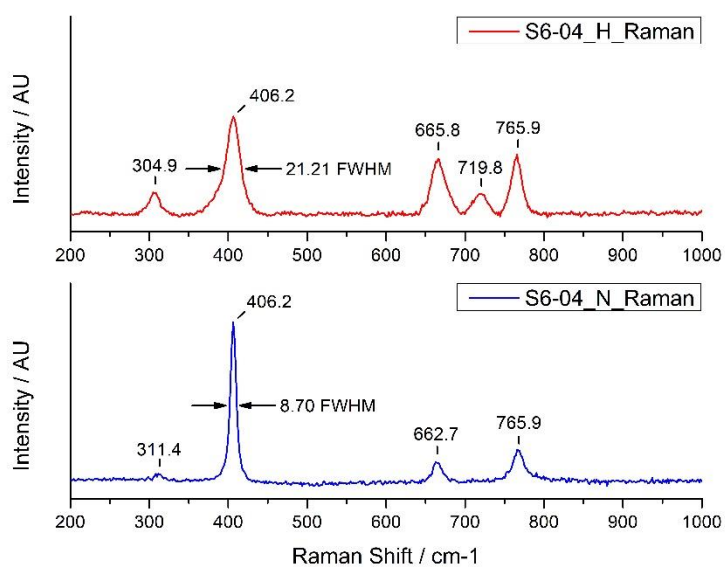


Figure 64 Raman spectra of natural (blue line) and heated (red line) spinel S6-04.

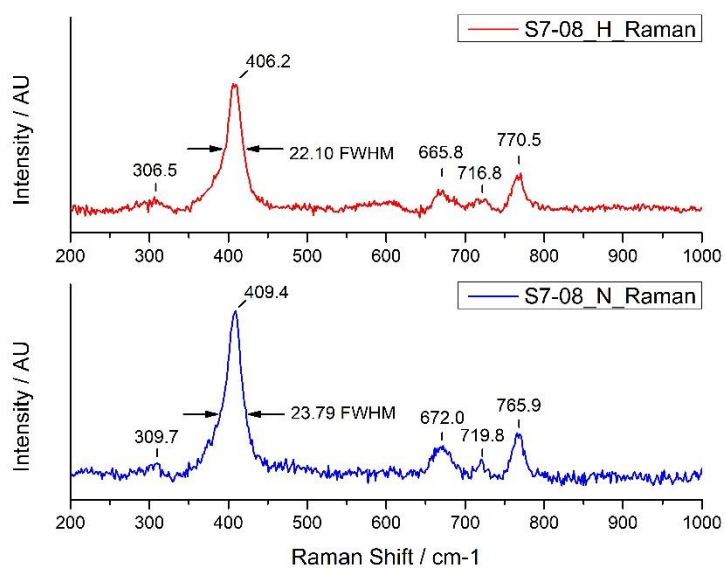


Figure 65 Raman spectra of natural (blue line) and heated (red line) spinel S7-08.

APPENDIX E

Spinel PL Spectra

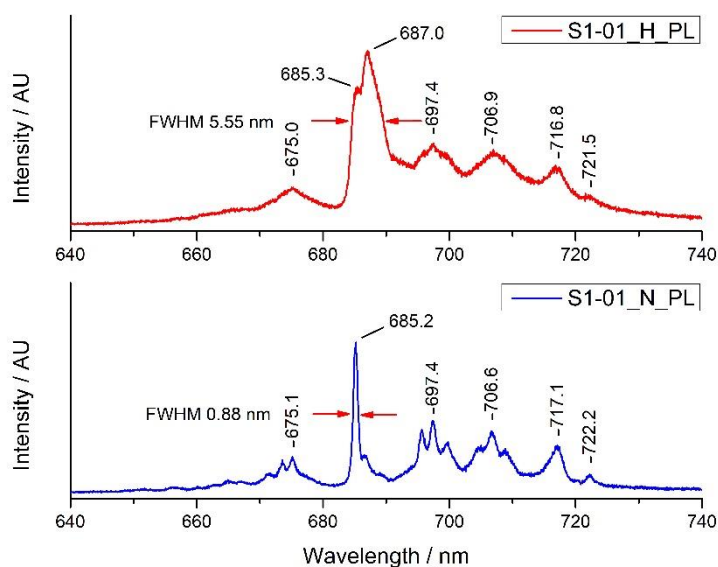


Figure 66 PL spectra of natural (blue line) and heated (red line) spinel S1-01.

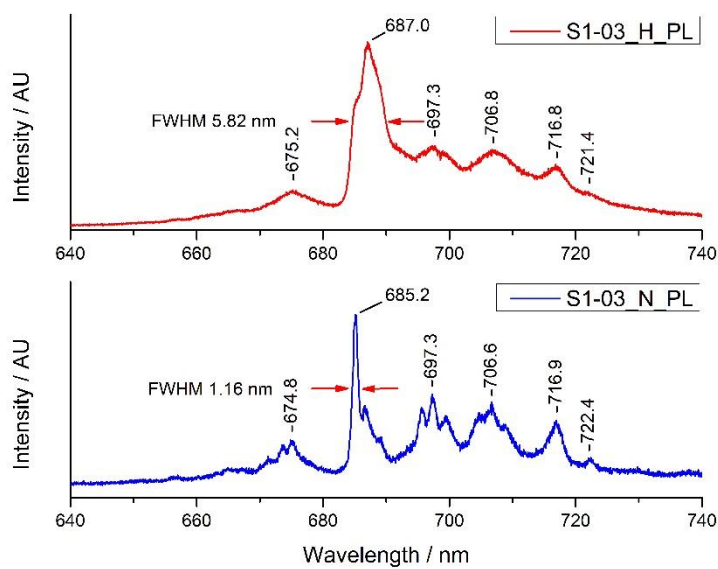


Figure 67 PL spectra of natural (blue line) and heated (red line) spinel S1-03.

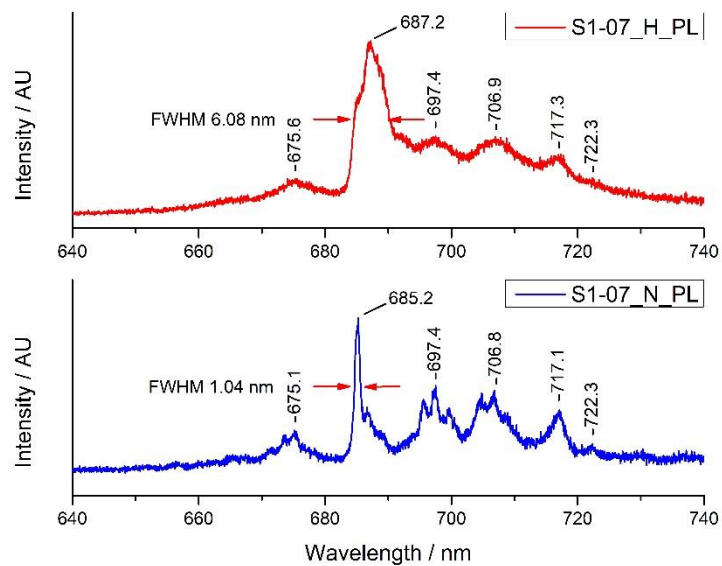


Figure 68 PL spectra of natural (blue line) and heated (red line) spinel S1-07.

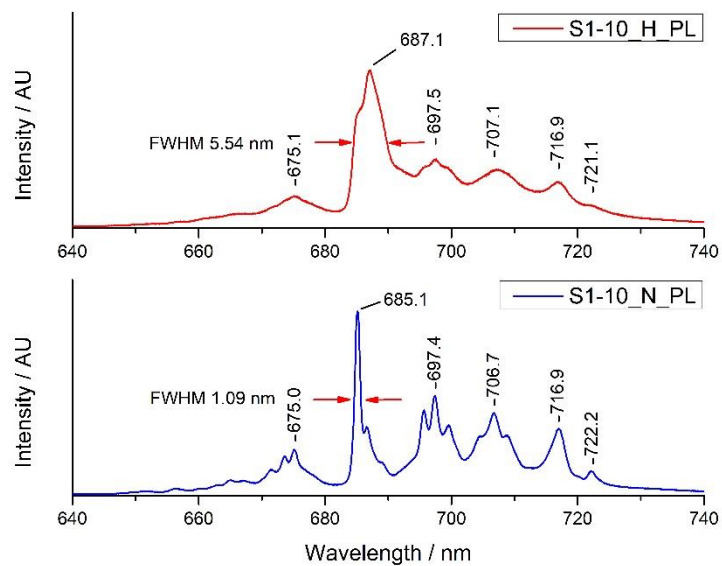


Figure 69 PL spectra of natural (blue line) and heated (red line) spinel S1-10.

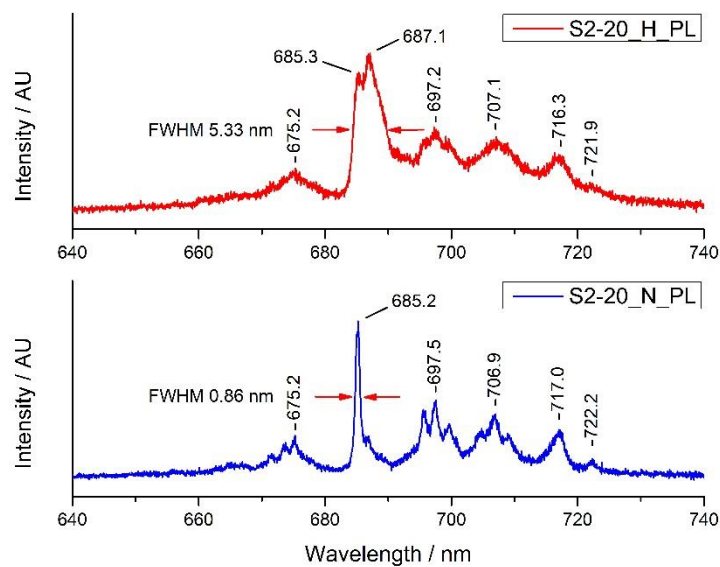


Figure 70 PL spectra of natural (blue line) and heated (red line) spinel S2-20.

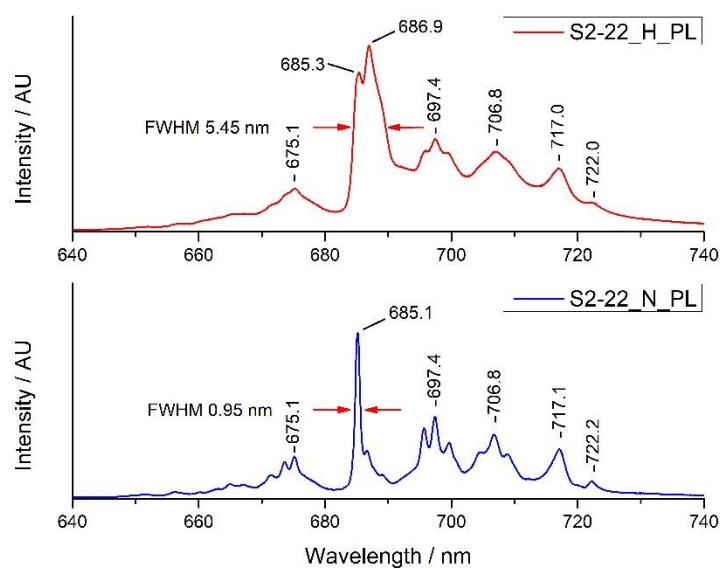


Figure 71 PL spectra of natural (blue line) and heated (red line) spinel S2-22.

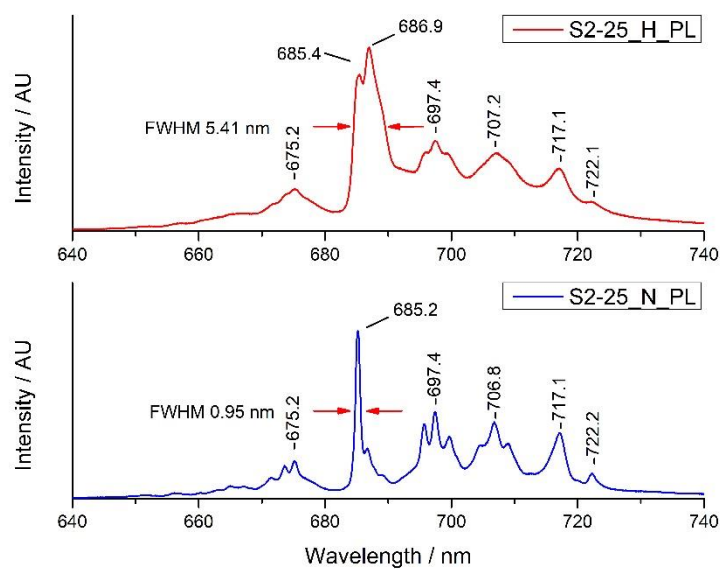


Figure 72 PL spectra of natural (blue line) and heated (red line) spinel S2-25.

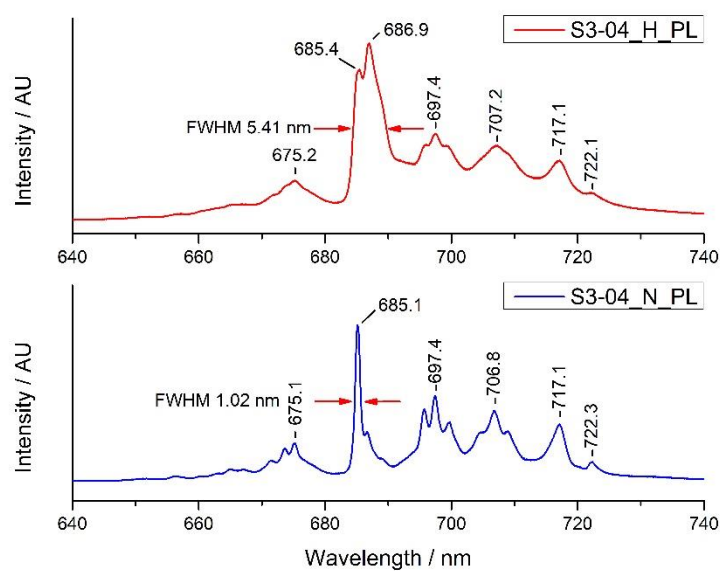


Figure 73 PL spectra of natural (blue line) and heated (red line) spinel S3-04.

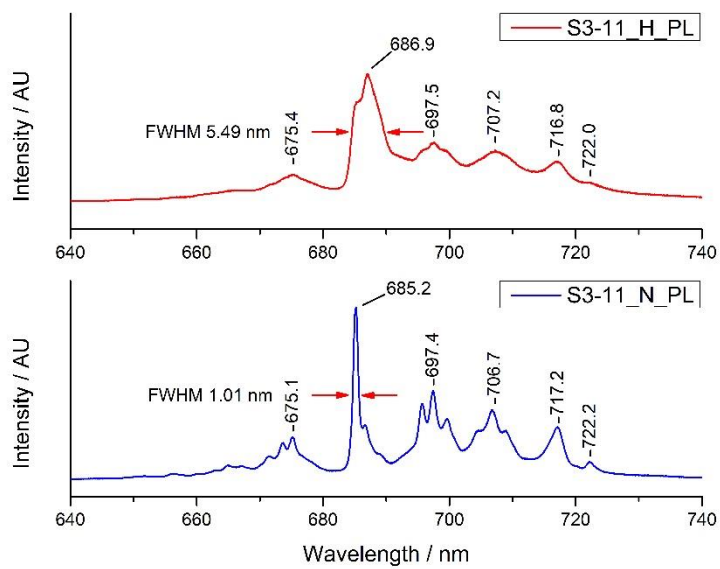


Figure 74 PL spectra of natural (blue line) and heated (red line) spinel S3-11.

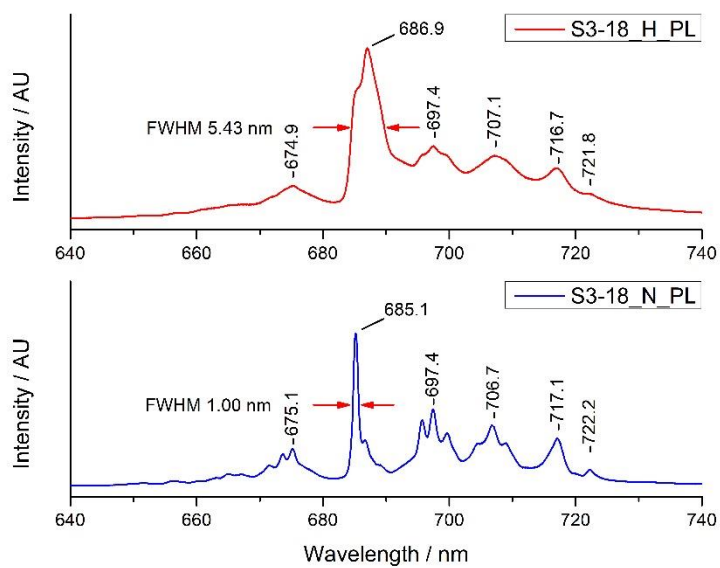


Figure 75 PL spectra of natural (blue line) and heated (red line) spinel S3-18.

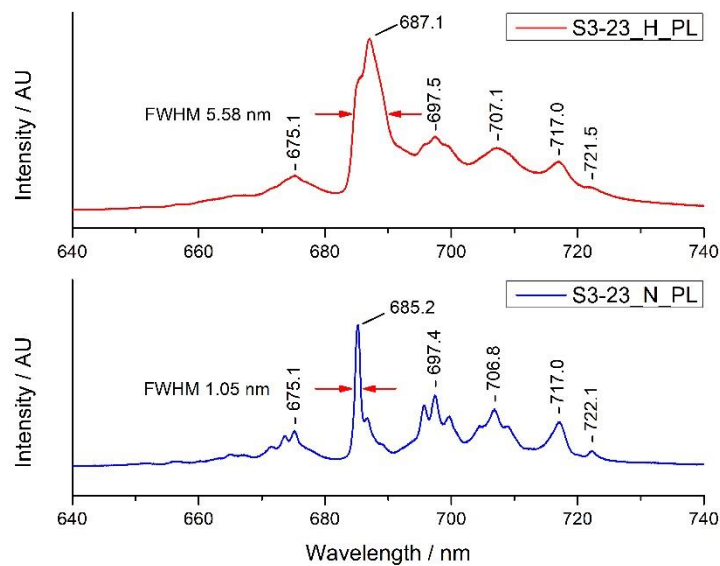


Figure 76 PL spectra of natural (blue line) and heated (red line) spinel S3-23.

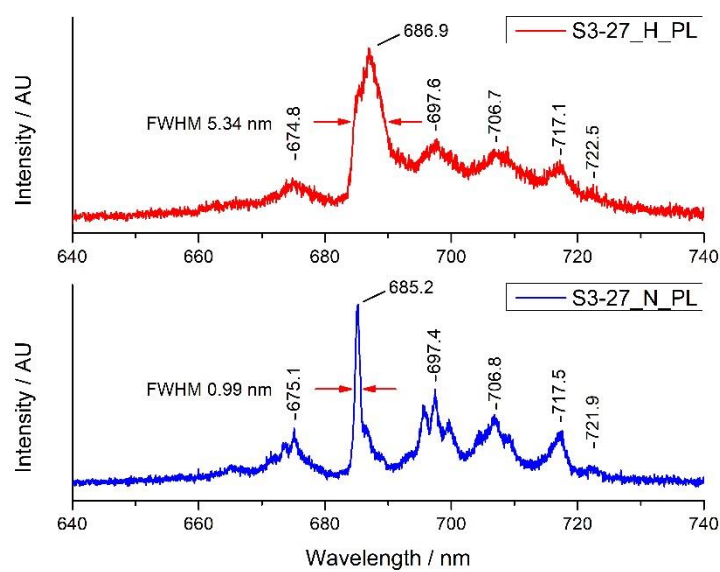


Figure 77 PL spectra of natural (blue line) and heated (red line) spinel S3-27.

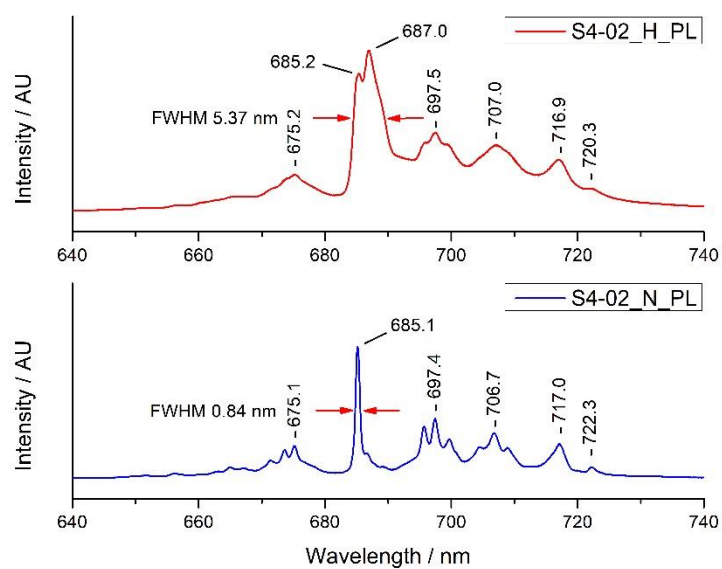


Figure 78 PL spectra of natural (blue line) and heated (red line) spinel S4-02.

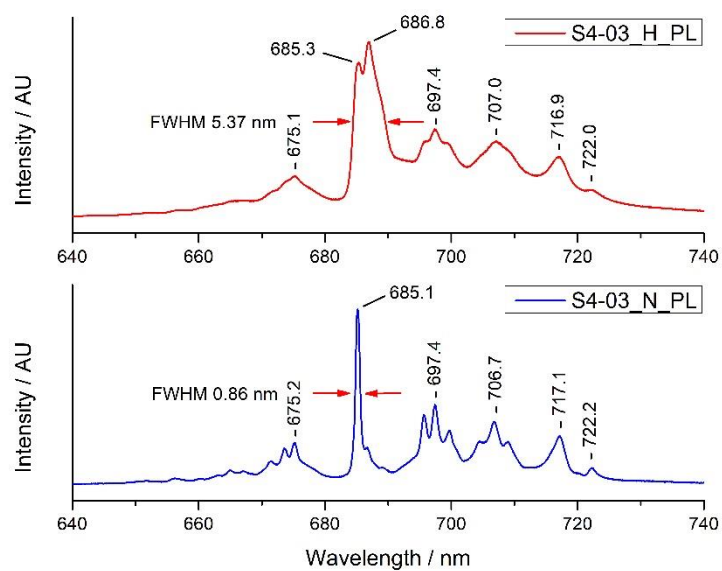


Figure 79 PL spectra of natural (blue line) and heated (red line) spinel S4-03.

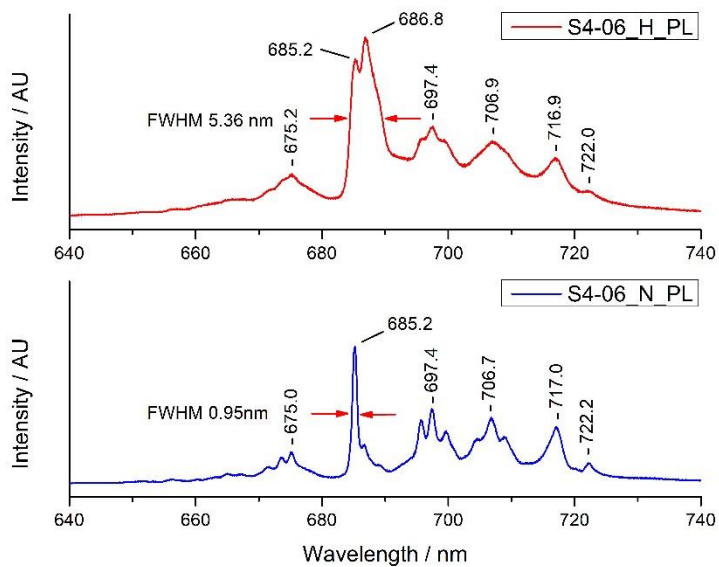


Figure 80 PL spectra of natural (blue line) and heated (red line) spinel S4-06.

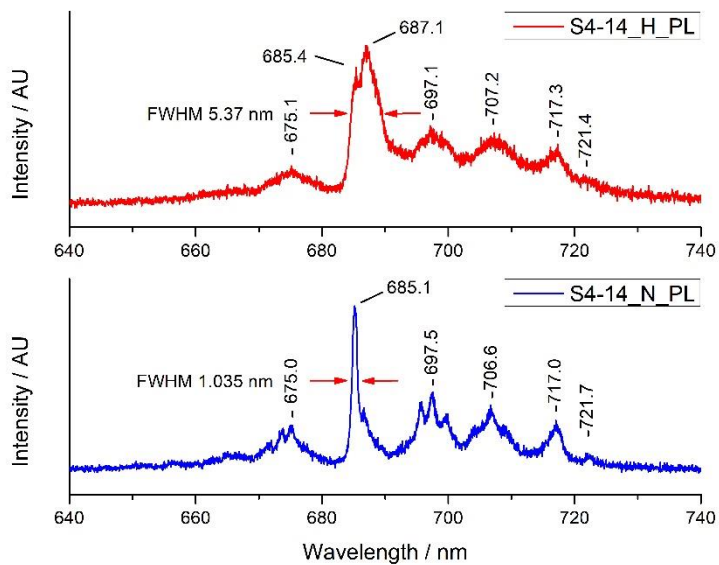


Figure 81 PL spectra of natural (blue line) and heated (red line) spinel S4-14.

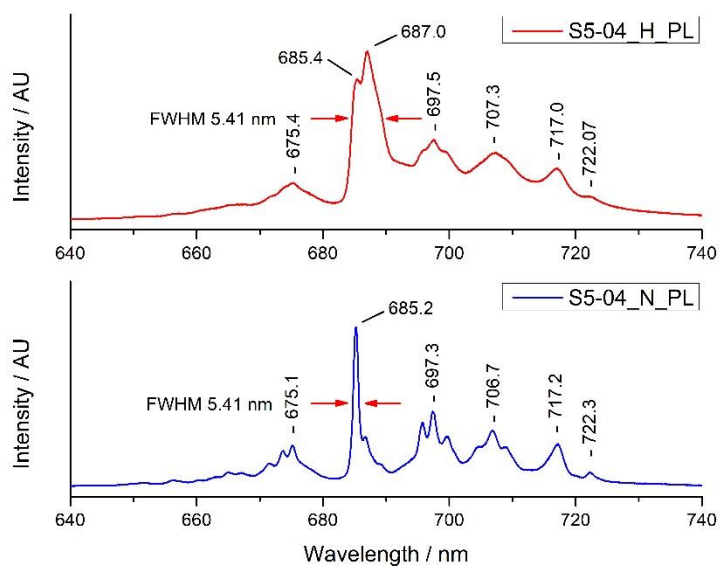


Figure 82 PL spectra of natural (blue line) and heated (red line) spinel S5-04.

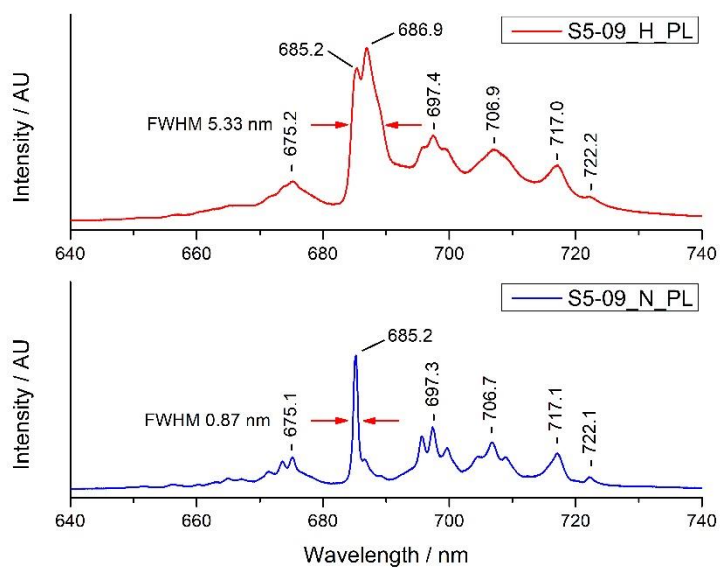


Figure 83 PL spectra of natural (blue line) and heated (red line) spinel S5-09.

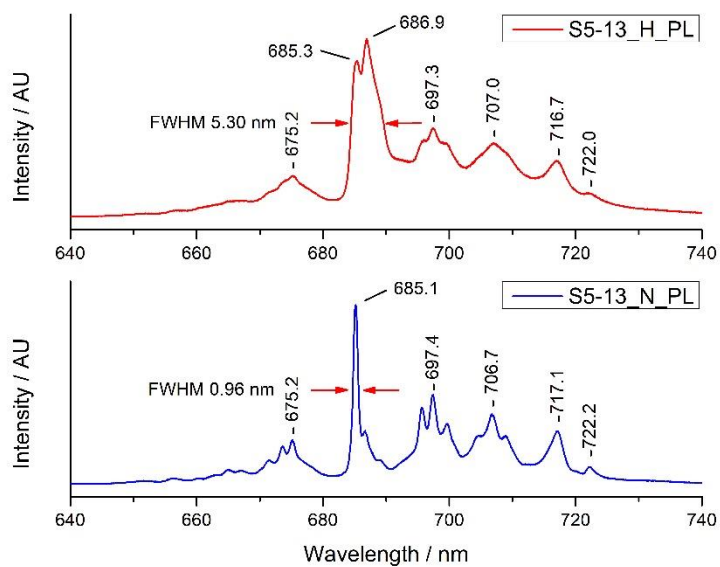


Figure 84 PL spectra of natural (blue line) and heated (red line) spinel S5-13.

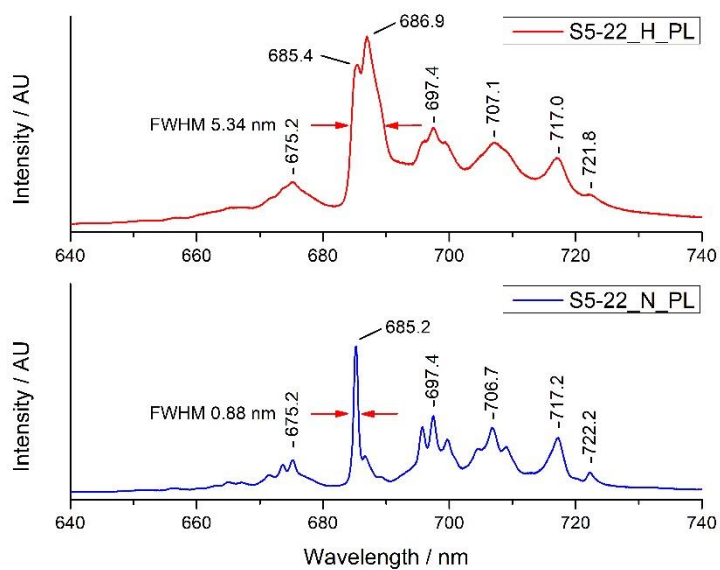


Figure 85 PL spectra of natural (blue line) and heated (red line) spinel S5-22.

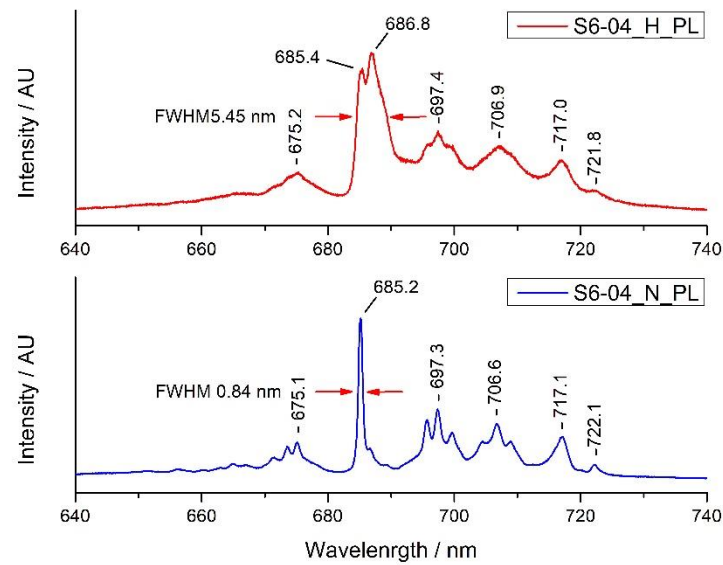


Figure 86 PL spectra of natural (blue line) and heated (red line) spinel S6-04.

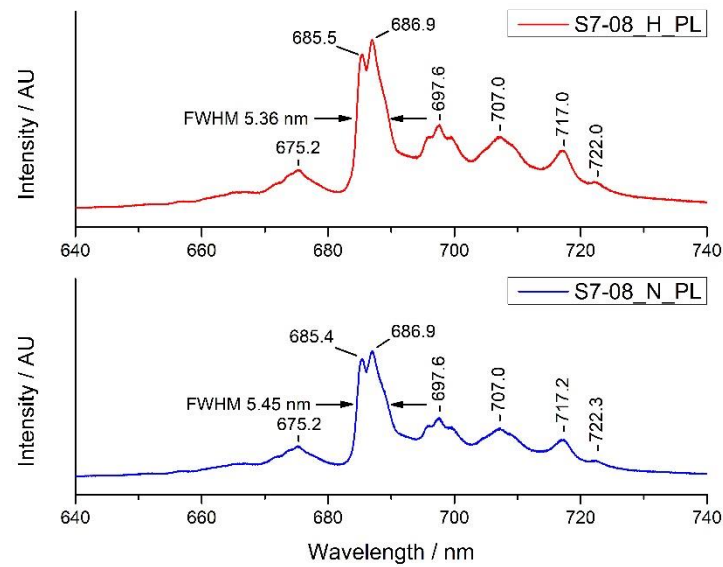


Figure 87 PL spectra of natural (blue line) and heated (red line) spinel S7-08.

APPENDIX F

Spinels Fe K-edge XANES Spectra

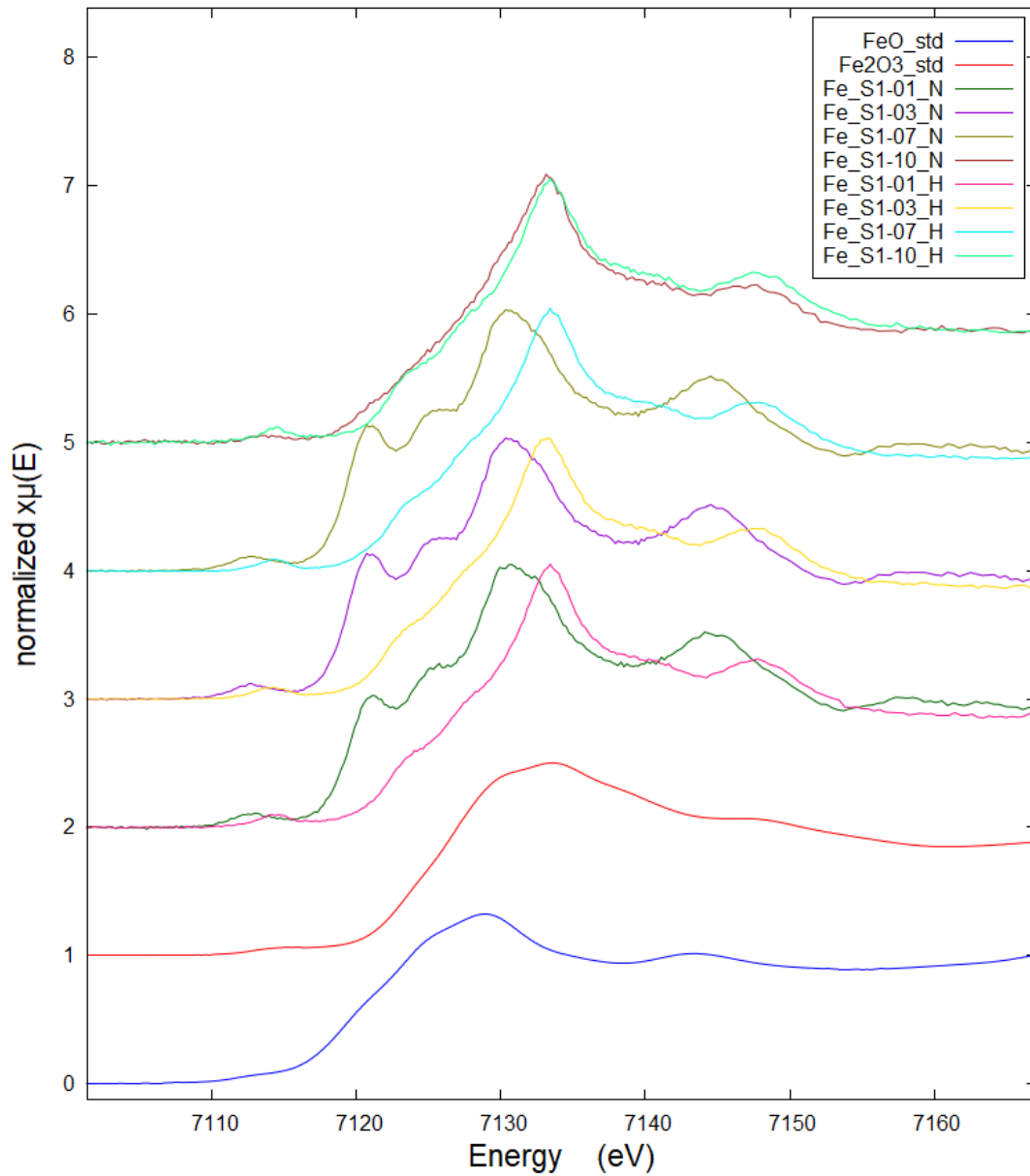


Figure 88 Normalized Fe K-edge XANES spectra of all natural and heated red spinels (S1) compared with Fe standards.

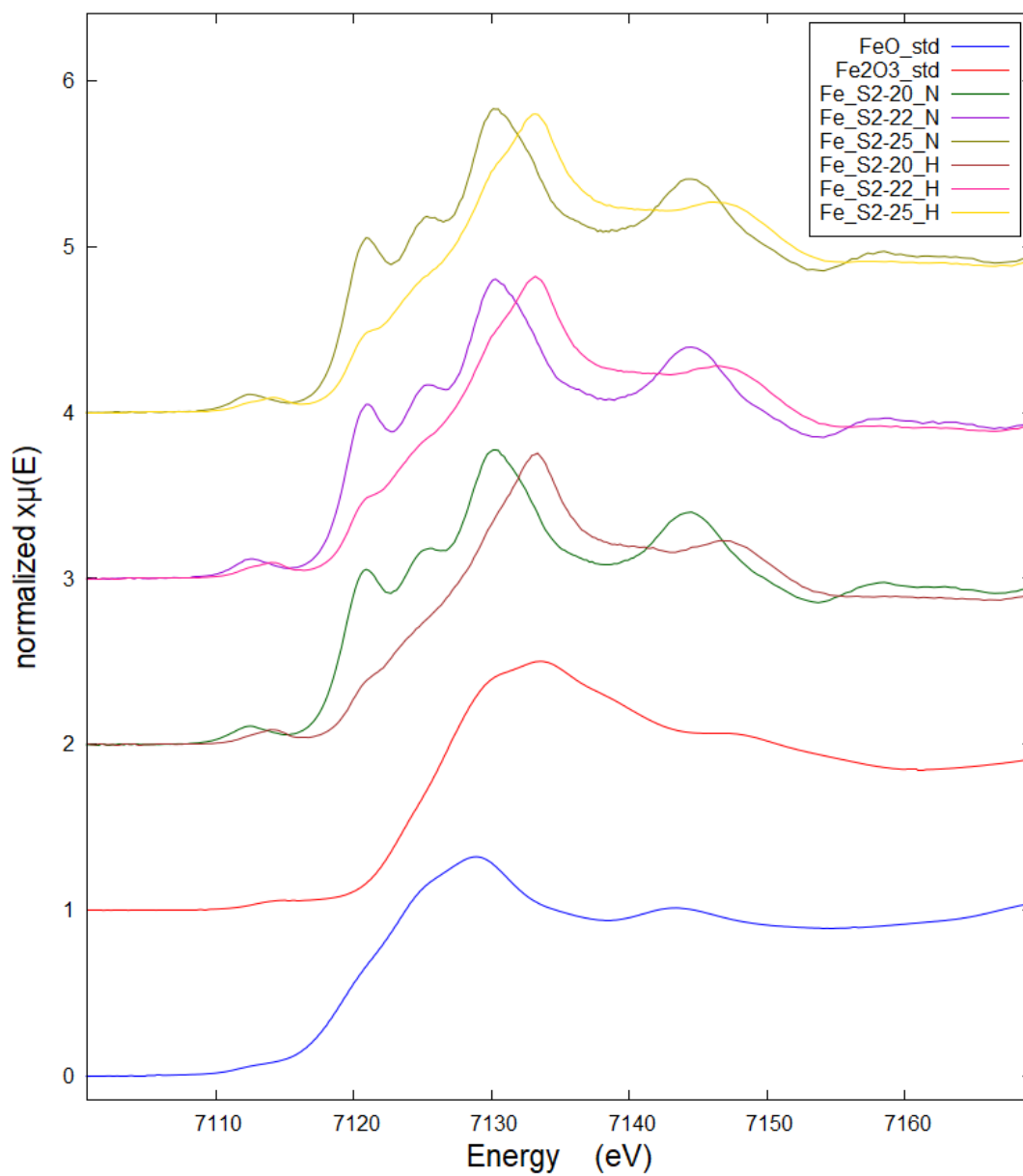


Figure 89 Normalized Fe K-edge XANES spectra of all natural and heated magenta spinels (S2) compared with Fe standards.

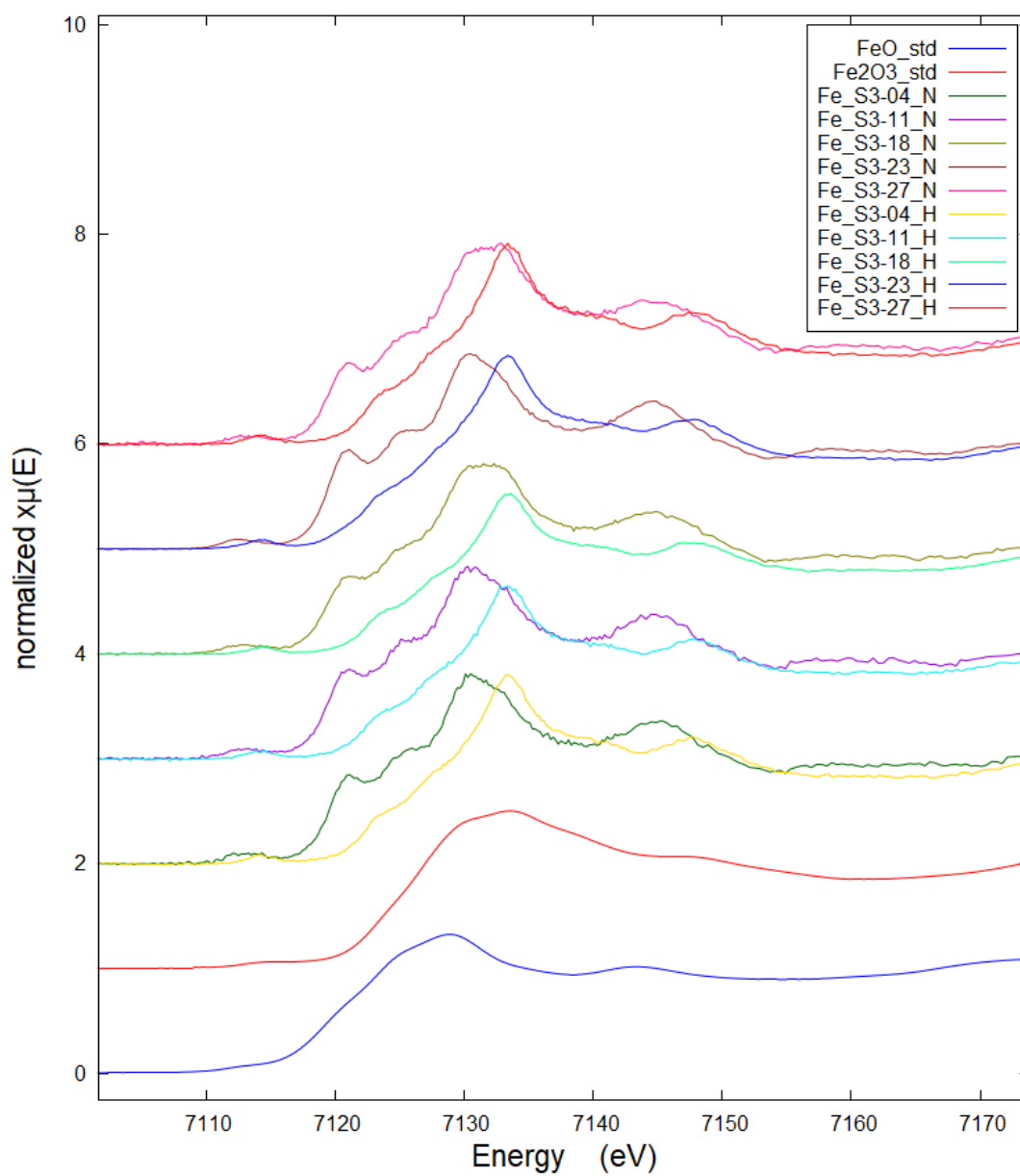


Figure 90 Normalized Fe K-edge XANES spectra of all natural and heated orange spinels (S3) compared with Fe standards.

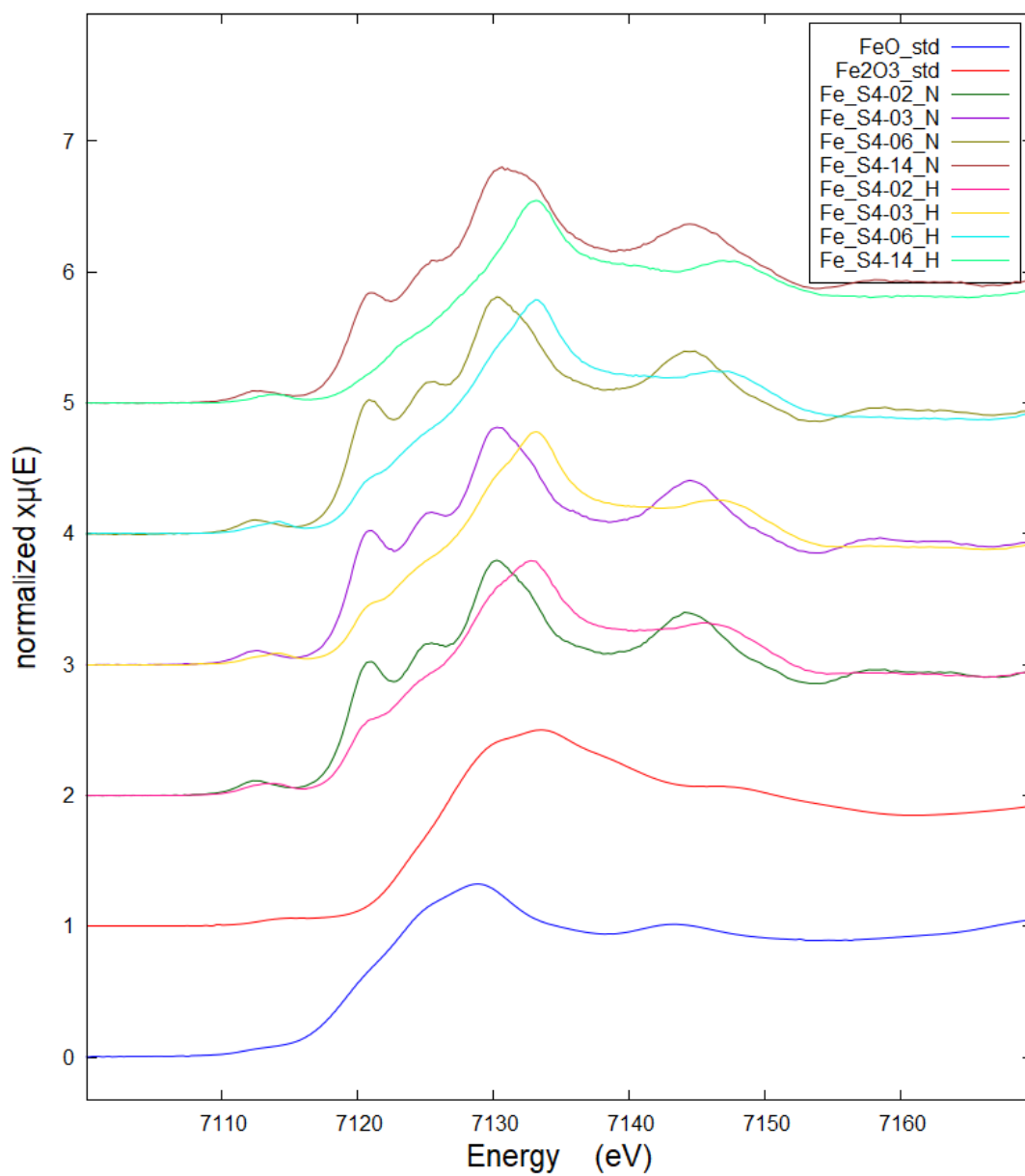


Figure 91 Normalized Fe K-edge XANES spectra of all natural and heated red-purple spinels (S4) compared with Fe standards.

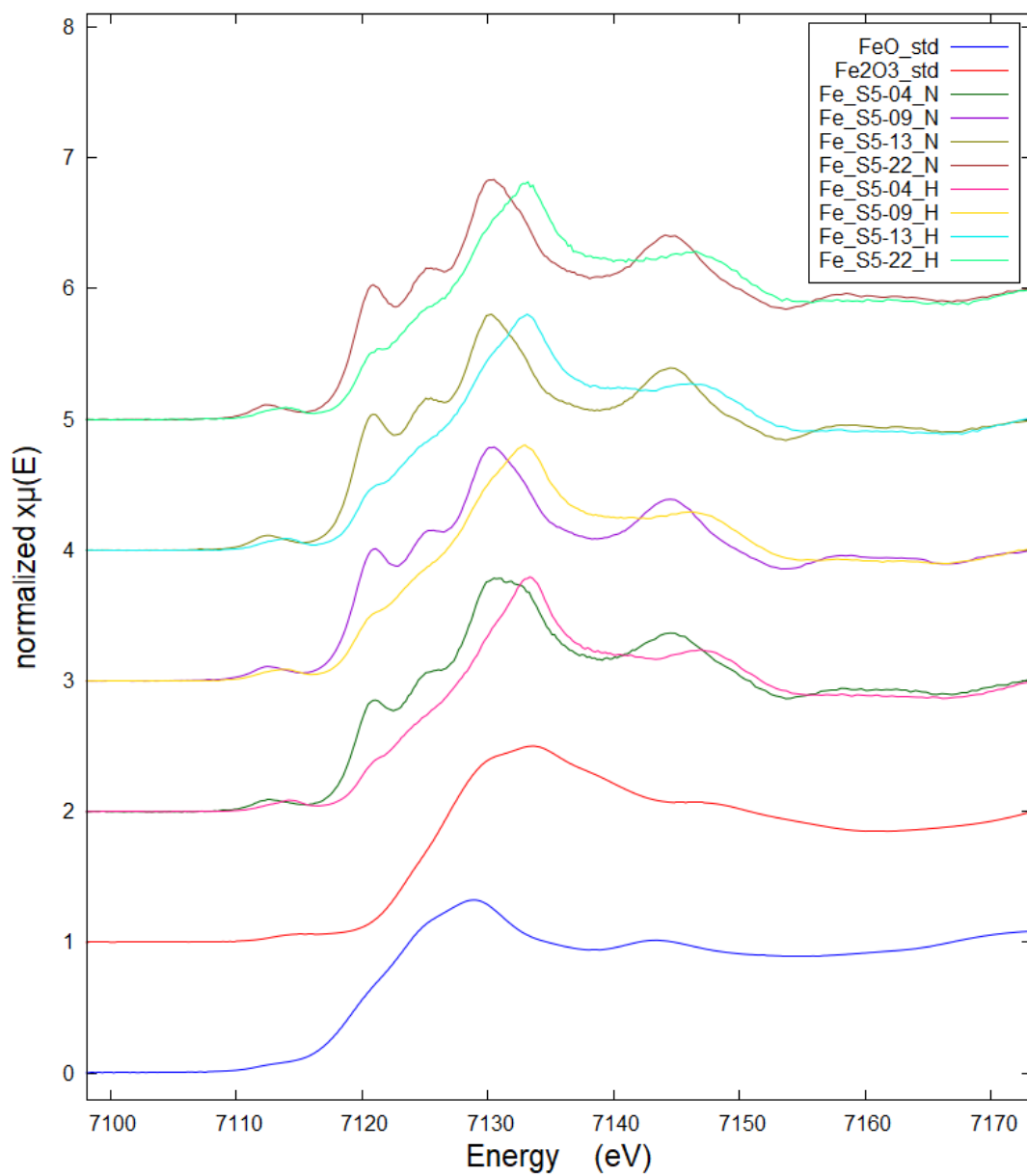


Figure 92 Normalized Fe K-edge XANES spectra of all natural and heated purple spinels (S5) compared with Fe standards.

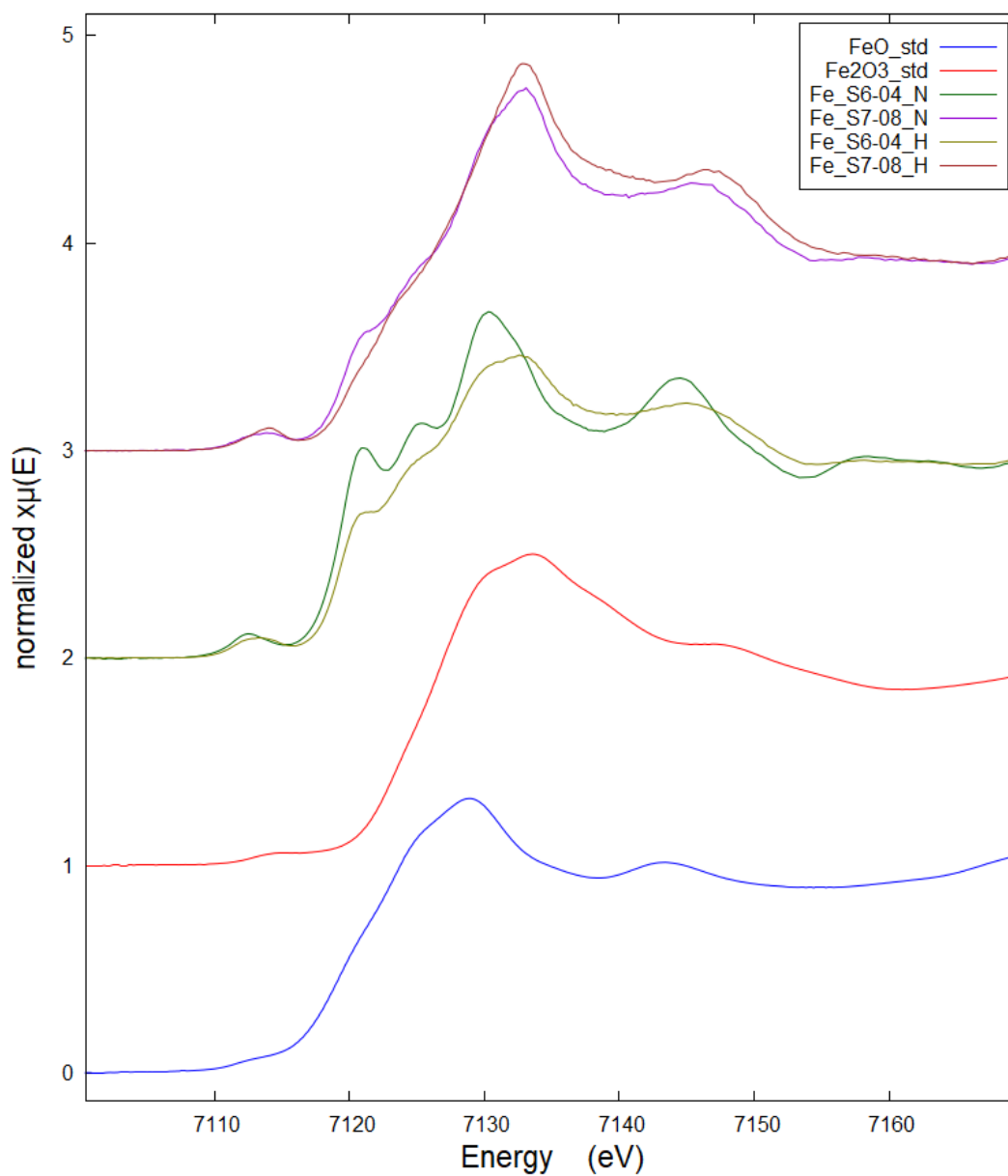


Figure 93 Normalized Fe K-edge XANES spectra of natural and heated blue (S6) and green spinels (S7) compared with Fe standards.

APPENDIX G

Spinel V K-edge XANES Spectra

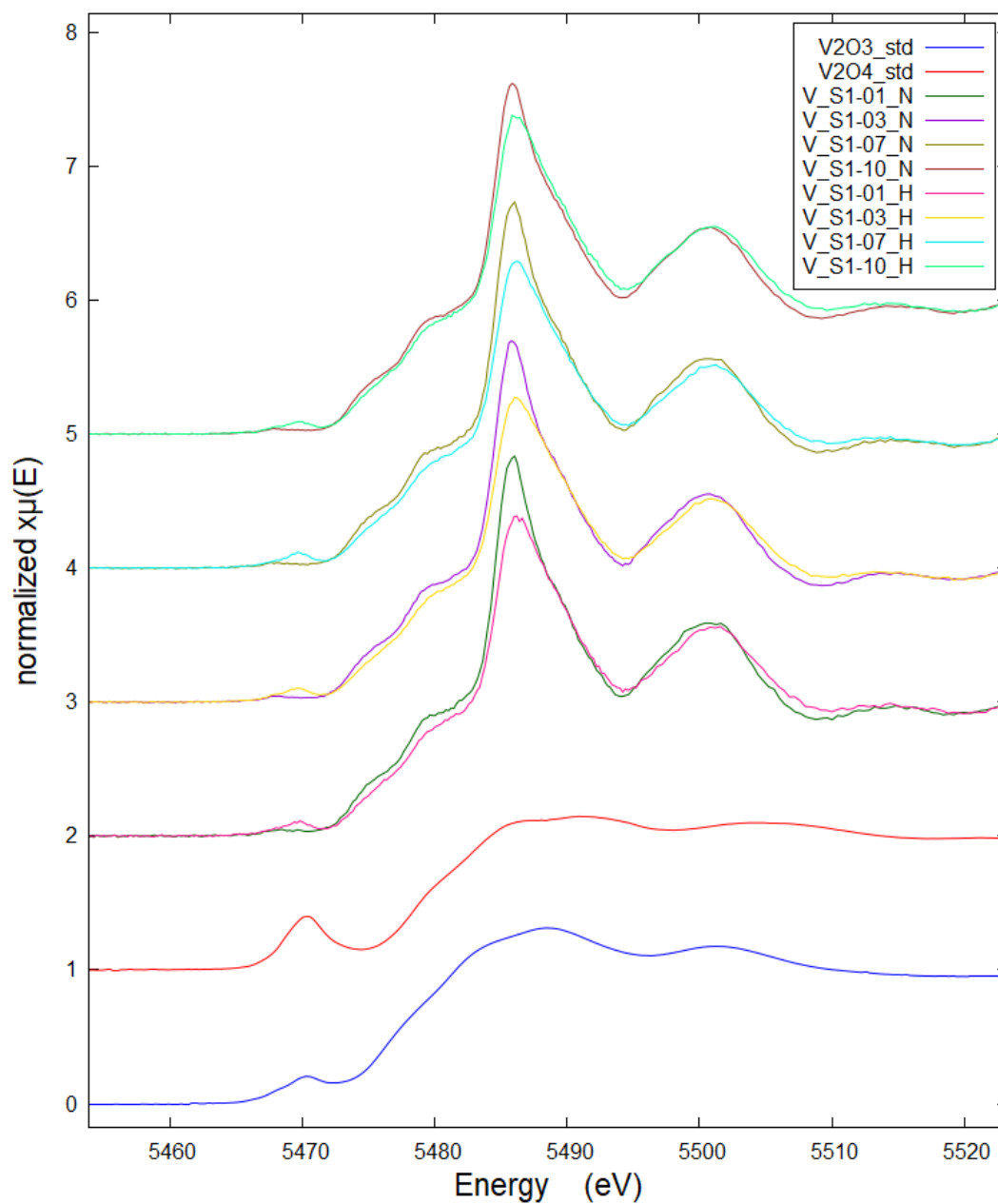


Figure 94 Normalized V K-edge XANES spectra of all natural and heated red spinels (S1) compared with V standards.

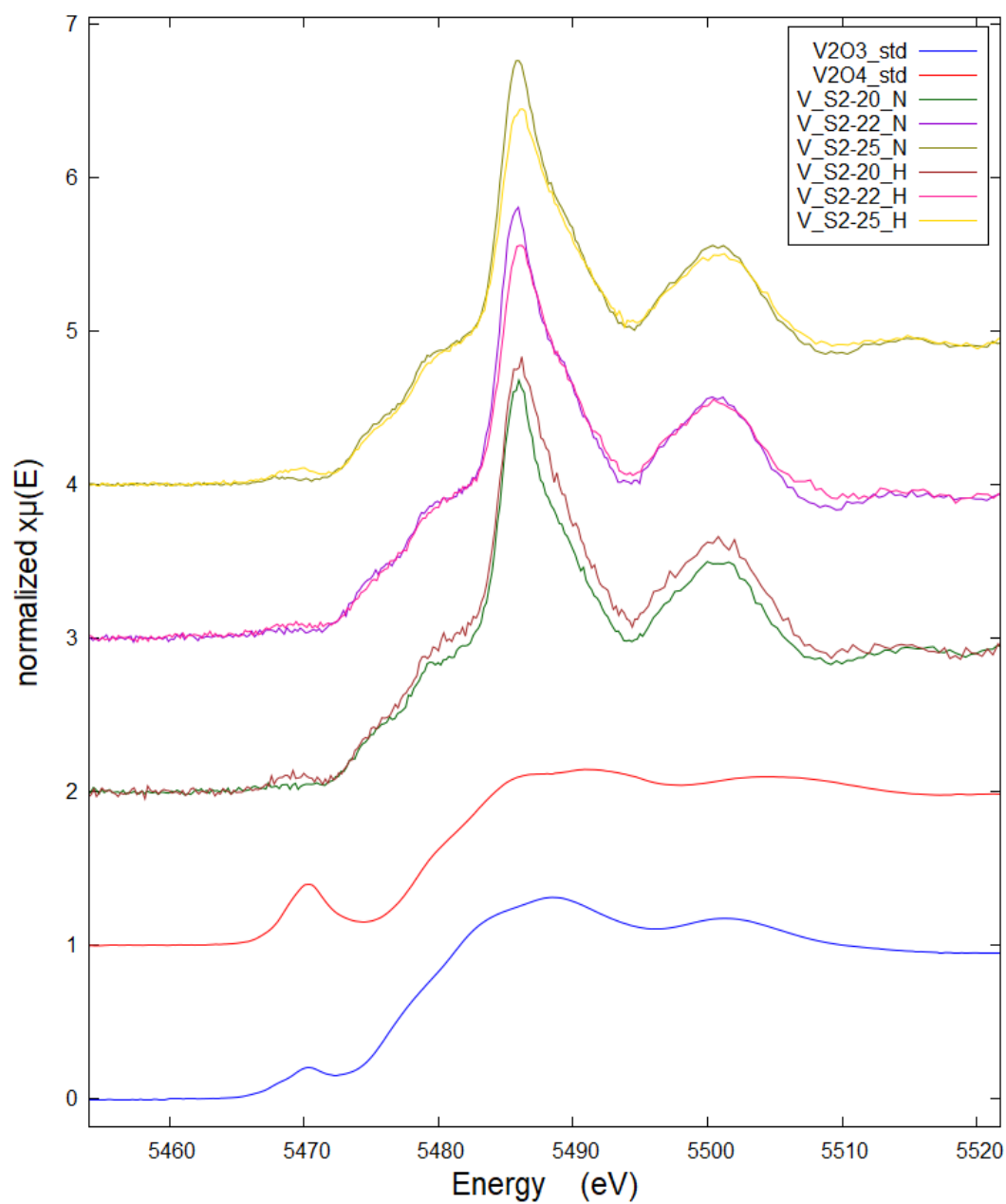


Figure 95 Normalized V K-edge XANES spectra of all natural and heated magenta spinels (S2) compared with V standards.

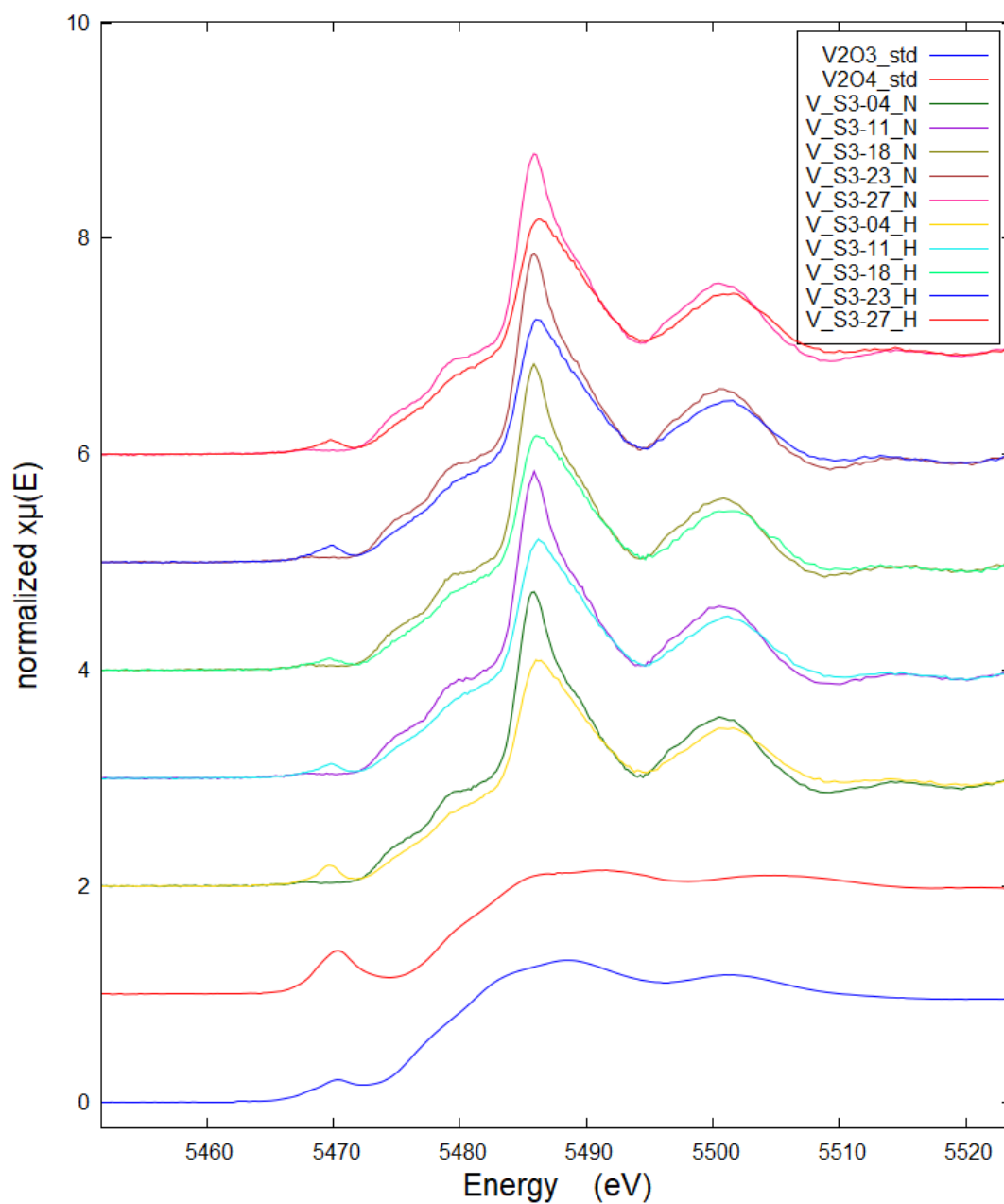


Figure 96 Normalized V K-edge XANES spectra of all natural and heated orange spinels (S3) compared with V standards.

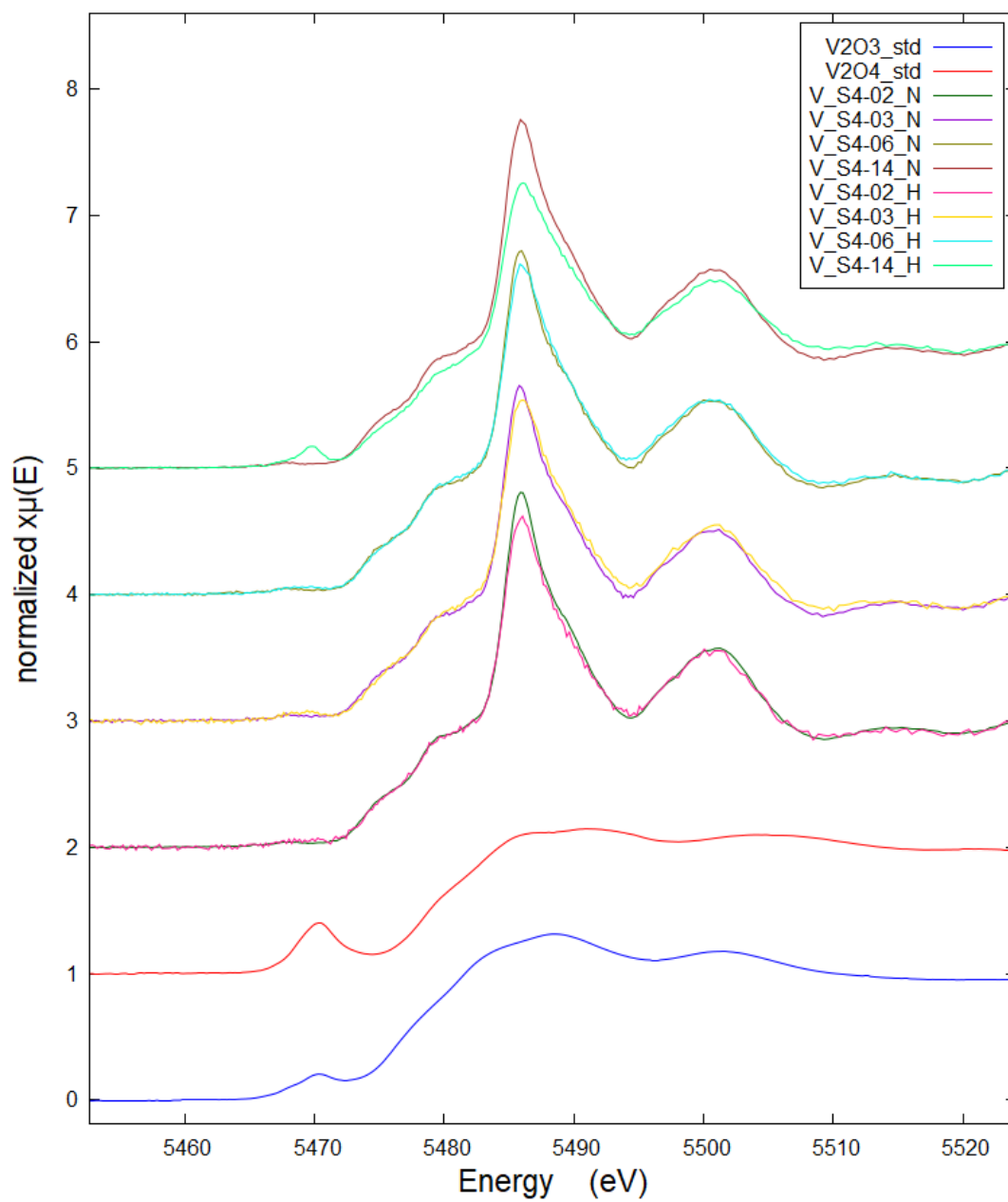


Figure 97 Normalized V K-edge XANES spectra of all natural and heated red-purple spinels (S4) compared with V standards.

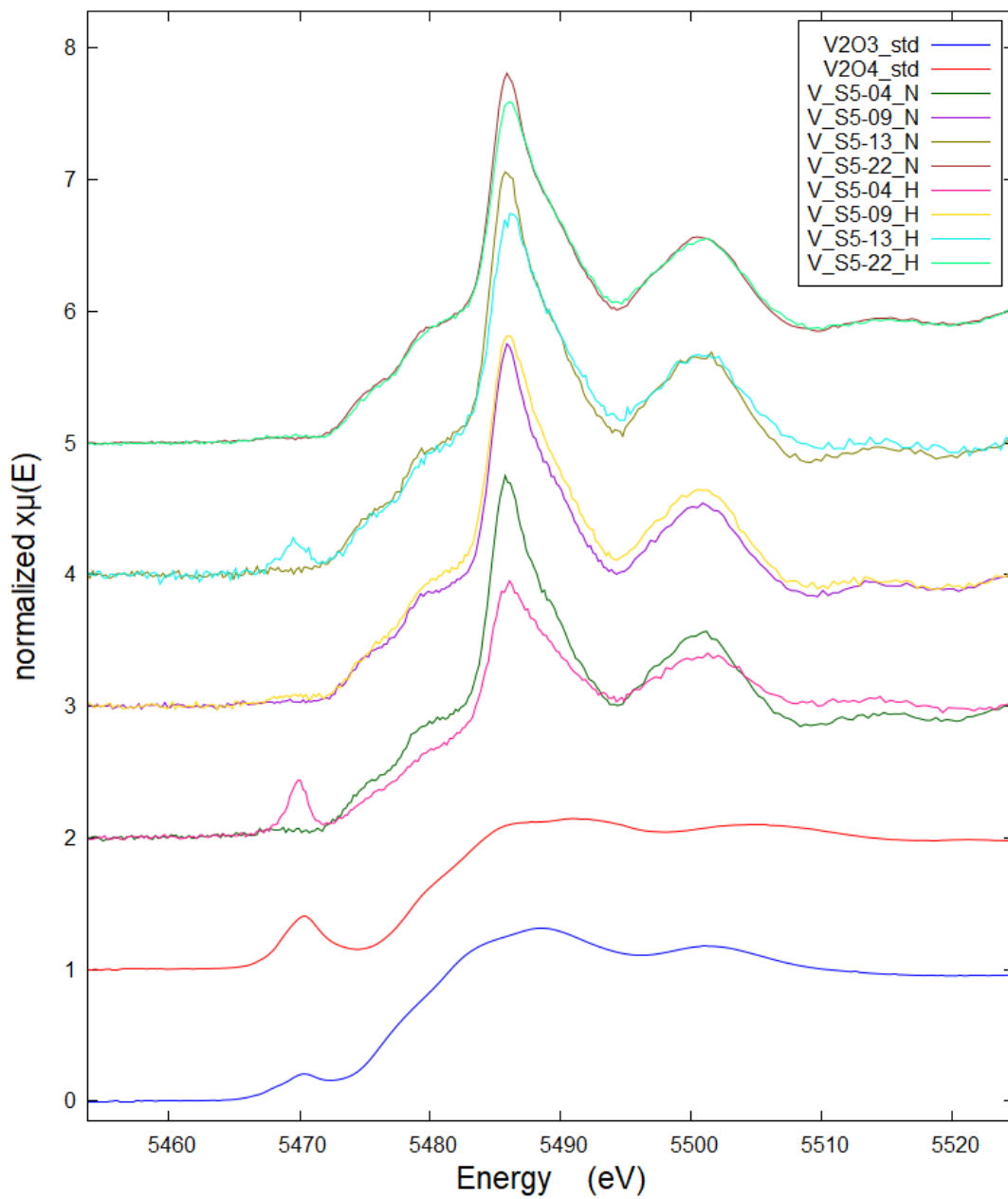


Figure 98 Normalized V K-edge XANES spectra of all natural and heated purple spinels (S5) compared with V standards.

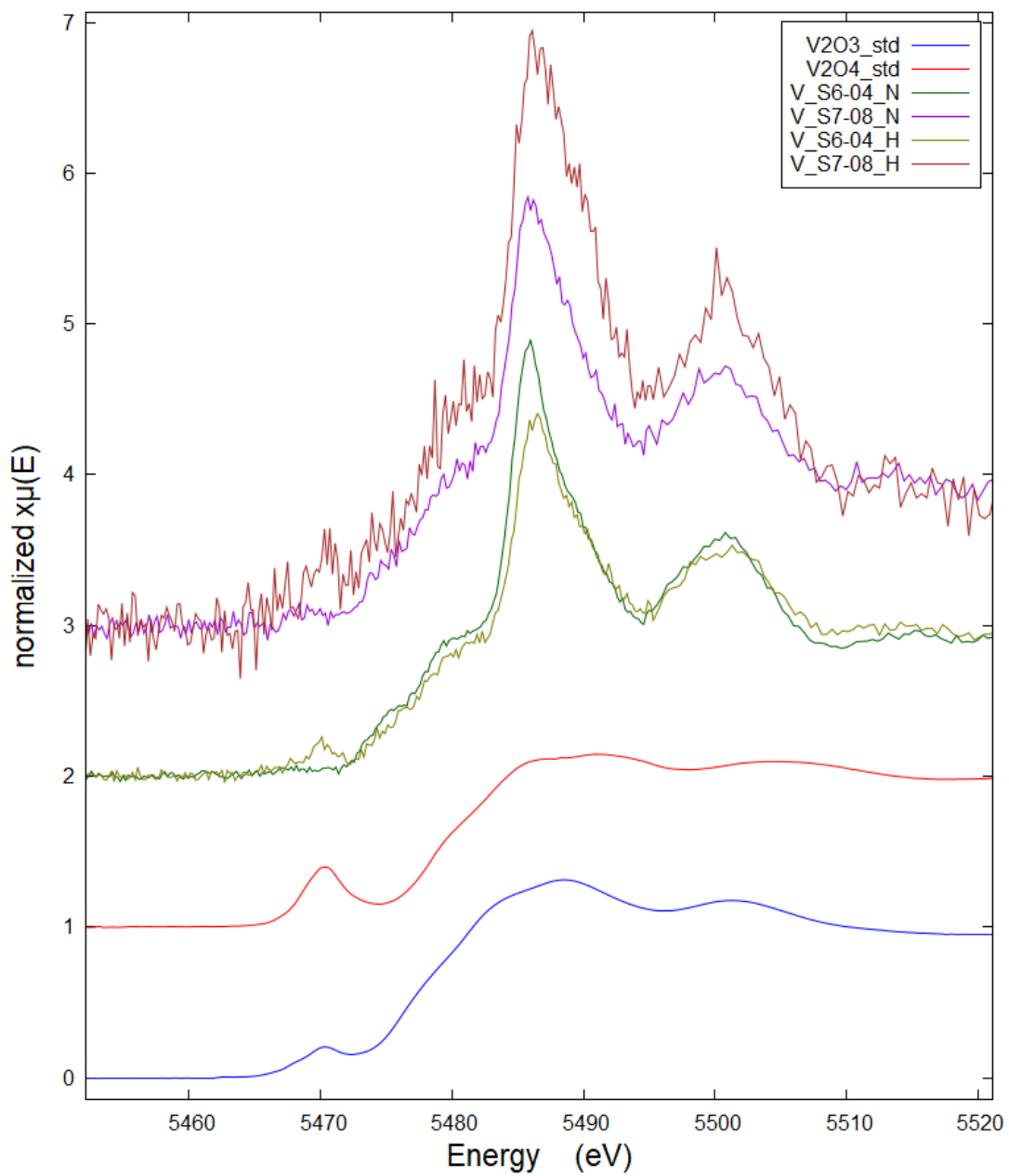


Figure 99 Normalized V K-edge XANES spectra of natural and heated blue (S6) and green spinels (S7) compared with V standards.

APPENDIX H

Fe-V-Cr pre-edge interpretation result diagrams

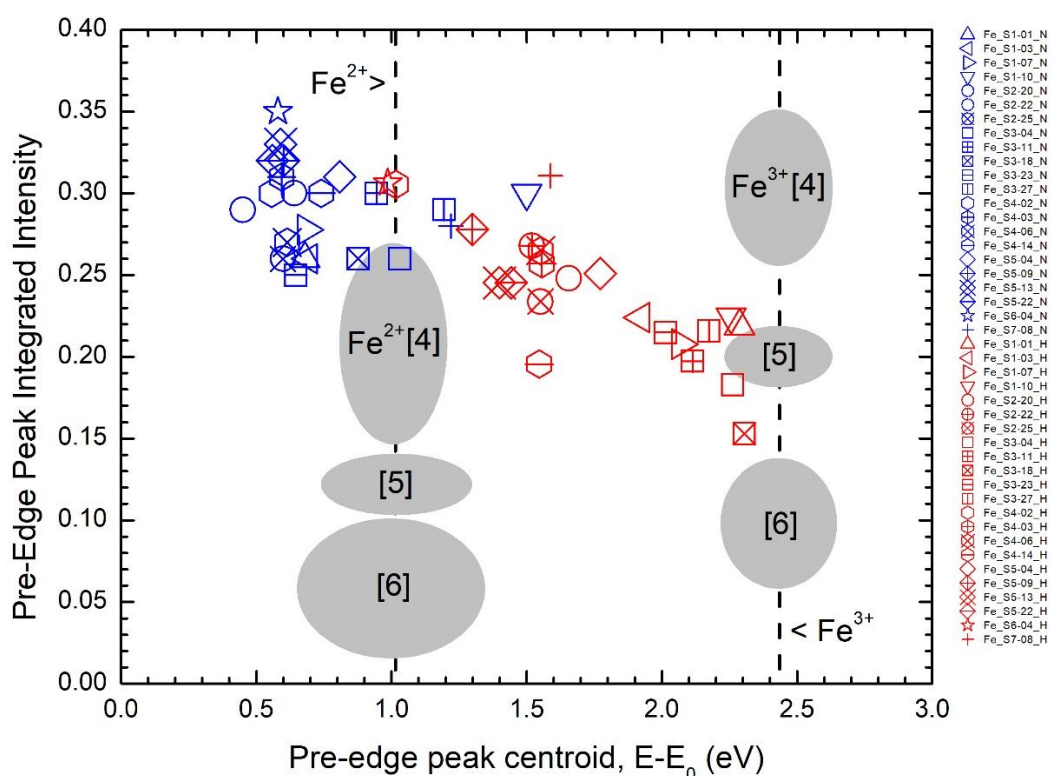


Figure 100 Diagram represented integrated pre-edge intensity and pre-edge peak centroid ($E-E_0$) parameter of all natural (blue dotted) and heated (red dotted) spinel samples in various Fe oxidation state and their coordination. Number [4], [5], and [6] represent a 4-fold, 5-fold, and 6-fold coordinated atoms, respectively.

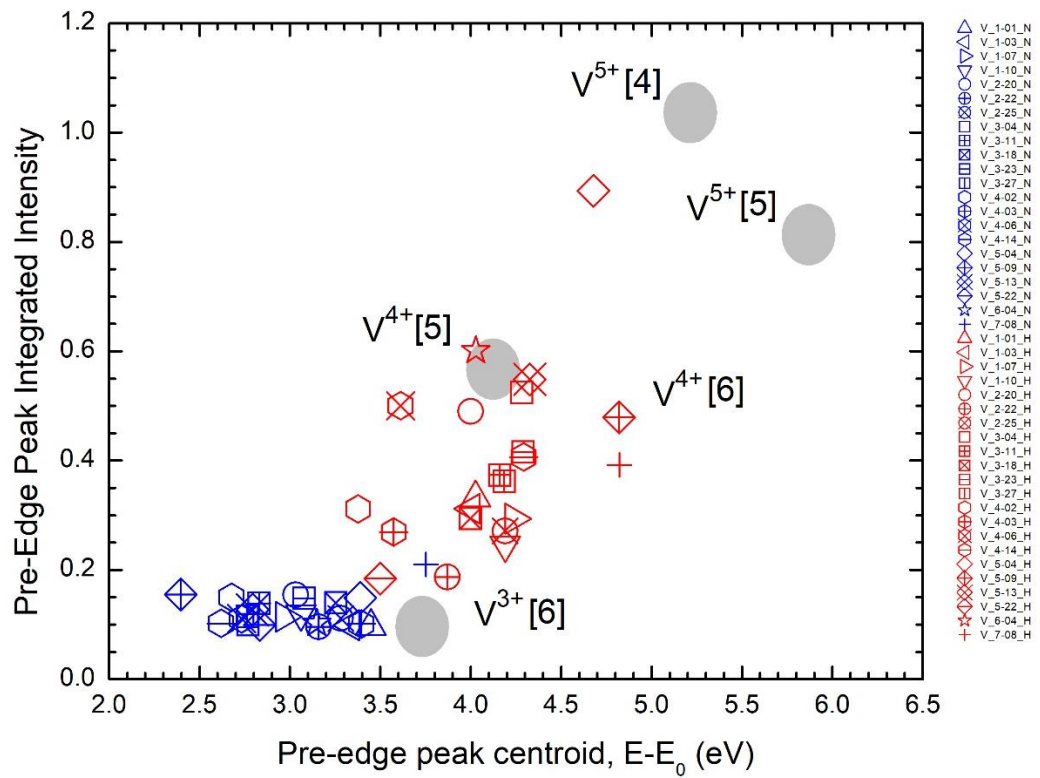


Figure 101 Diagram represented integrated pre-edge intensity and pre-edge peak centroid ($E-E_0$) parameter of all natural (blue dotted) and heated (red dotted) spinel samples in various V oxidation state and their coordination. Number [4], [5], and [6] represent a 4-fold, 5-fold, and 6-fold coordinated atoms, respectively.

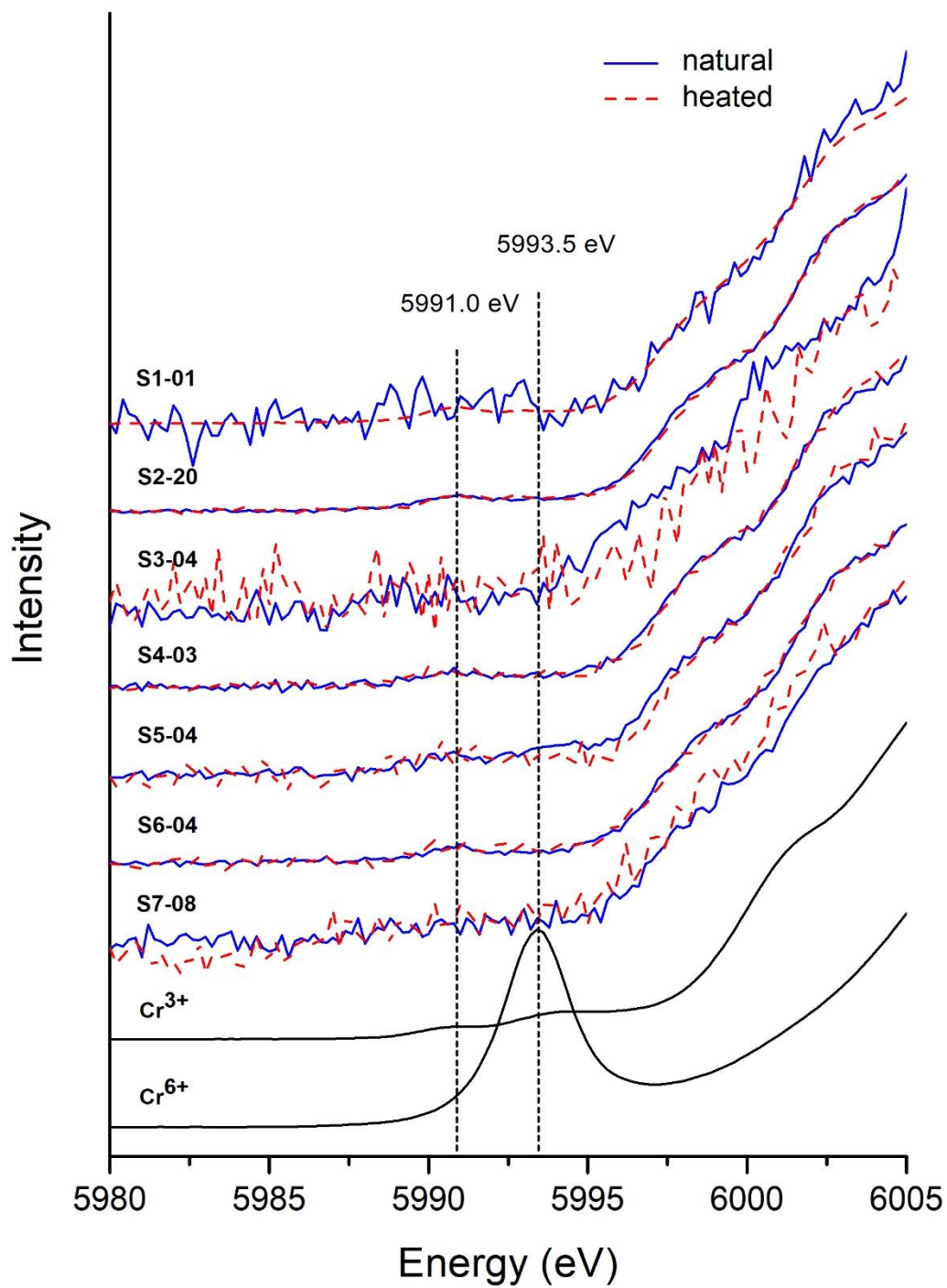


Figure 102 Diagram represented normalized Cr pre-edge XANES spectra of natural (blue lines) and heated (red lines) spinels compared with Cr(III) and Cr(VI) standards.

VITA

NAME Teerarat Pluthametwisute

DATE OF BIRTH 30 July 1995

PLACE OF BIRTH Bangkok, Thailand

INSTITUTIONS ATTENDED Secondary school: Sarasas Witaed Bangbon School
High school: Potisarn Pittayakorn School
Bachelor: Faculty of Gems, Burapha University, Chanthaburi Campus

HOME ADDRESS 113 soi 15/5 Nanthawan Village (Pinklao-Ratchapruerk), Bang ramad, Talingchan, Borommaratchachonnani 75 road, Bangkok, 10170.

PUBLICATION Article: Cause of Color Modification in Tanzanite after Heat Treatment. *Molecules*. 25. 3743. 10.3390/molecules25163743.

